

NONLINEAR MIXING OF TWO COLLINEAR RAYLEIGH WAVES

A Thesis
Presented to
The Academic Faculty

by

Merlin B. Morlock

In Partial Fulfillment
of the Requirements for the Degree
Master of Science in
Engineering Science and Mechanics

School of Civil and Environmental Engineering
Georgia Institute of Technology
December 2013
Copyright © 2013 Merlin B. Morlock

NONLINEAR MIXING OF TWO COLLINEAR RAYLEIGH WAVES

Approved by:

Professor Laurence J. Jacobs, Advisor
School of Civil and Environmental
Engineering
Georgia Institute of Technology

Dr. Jin-Yeon Kim
School of Civil and Environmental
Engineering
Georgia Institute of Technology

Dr. Jianmin Qu
Department of Civil and Environmental
Engineering
Northwestern University

Date Approved: 22 August 2013

ACKNOWLEDGEMENTS

First of all, I want to thank Helene Mohr and Sonja Morlock who exceptionally supported me in the last years.

I also want to thank Sebastian Thiele without whom the experimental part of my research would not have been possible. Furthermore, I want to thank Dr. Jin-Yeon Kim who was always there to steer my research in promising directions and helped me in numerous fruitful discussions. Moreover, I want to thank my advisor Prof. Laurence J. Jacobs for helping in all kinds of study related problems, supporting me throughout my graduate studies and for giving me the opportunity to take part in the Quantitative Nondestructive Evaluation conference in Baltimore. I also thank Prof. Lothar Gaul for choosing me for the ISAP exchange program.

Besides, I am grateful for being financially supported by the DAAD (German Academic Exchange Service) and the FES (Friedrich-Ebert-Stiftung).

TABLE OF CONTENTS

ACKNOWLEDGEMENTS	iii
LIST OF TABLES	vii
LIST OF FIGURES	viii
LIST OF SYMBOLS AND ABBREVIATIONS	xiv
SUMMARY	xv
I INTRODUCTION	1
1.1 Motivation	1
1.2 Problem Statement	3
1.3 Literature Review	4
1.4 Gap Analysis	5
1.5 Outline	6
II FUNDAMENTALS OF WAVE PROPAGATION IN SOLIDS . .	8
2.1 Problem Specific Definitions	8
2.2 Mathematical Tools	9
2.2.1 Notation	9
2.2.2 Gauss' Theorem	10
2.2.3 Lagrangian Mechanics	10
2.2.4 Helmholtz Decomposition	11
2.3 Linear Wave Propagation	11
2.3.1 Linear Stress Strain Relationship	12
2.3.2 Cauchy's Equation of Motion	12
2.3.3 Linear Wave Equation	14
2.3.4 P-waves and S-waves	16
2.3.5 Refraction, Reflection and Transmission	18
2.3.6 Linear Rayleigh Waves	20
2.4 Nonlinear Wave Propagation	25

2.4.1	Derivation	26
2.4.2	Acoustic Nonlinearity Parameter for P-waves	27
III	ANALYTICAL MODEL OF THE MIXING PROCESS	29
3.1	Two Dimensional Model	30
3.1.1	Modeling	30
3.1.2	Numerical Simulations	51
3.1.3	Justification of Weak Nonlinearity Assumption	61
3.2	Simplified Two Dimensional Model	62
3.2.1	Modeling	62
3.2.2	Simulation	64
3.3	Diffraction Model	66
3.4	Simplified Diffraction Model	70
3.5	Acoustic Nonlinearity Parameter β	71
3.5.1	Modeling	71
3.5.2	Simulation	73
IV	FINITE ELEMENT METHOD SIMULATION	76
4.1	Modeling	77
4.1.1	Geometry	77
4.1.2	Material	78
4.1.3	Physics and Boundary Conditions	79
4.1.4	Nonlinearity	80
4.1.5	Mesh	81
4.1.6	Time stepping	82
4.1.7	Solver	82
4.2	Simulation	83
4.2.1	Computing	83
4.2.2	Signal Processing	83
4.2.3	Results for Different Frequencies and Amplitudes	86

4.2.4	Variation of Specimen Size	88
4.2.5	Variation of Wedge Size	90
4.2.6	Variation of Nonlinearity	90
4.2.7	Variation of Mesh Size	93
4.2.8	Variation of Time Step	93
4.3	FEM Conclusion	93
V	EXPERIMENTAL VALIDATION	94
5.1	Experimental Setup	94
5.1.1	Experimental Procedure	94
5.1.2	Experimental Devices	95
5.2	Experimental Results	103
5.2.1	Feasibility of Rayleigh Wave Mixing	103
5.2.2	Variation of Amplitudes for Fixed Frequencies	109
5.2.3	Variation of Frequencies for Fixed Amplitudes	114
5.2.4	Comparison of Experiments with Analytical Model	115
VI	CONCLUSION AND FUTURE WORK	118
6.1	Conclusion	118
6.2	Future Work	119
	REFERENCES	121

LIST OF TABLES

3.1	Elastic parameters of steel.	51
3.2	Elastic parameters of fused quartz.	57
3.3	Elastic parameters of 7075-T651 Aluminum.	64

LIST OF FIGURES

2.1	Principle of balance of linear momentum for Cauchy's first law of motion.	13
2.2	Reflection and transmission of an incident P-wave at a solid-solid boundary.	18
2.3	Reflection of an incident SV-wave at a stress free boundary.	19
2.4	Generation of a Rayleigh wave with the wedge excitation method. . .	20
2.5	Propagation of an evanescent Rayleigh wave in an semi-infinite elastic solid with wave vector \mathbf{k}_r	22
2.6	Three dimensional model from [39] of a Rayleigh wave propagating through a solid.	25
3.1	Phase matching for non-collinear and collinear mixing of two Rayleigh waves.	31
3.2	Sketch of the effect of a nonlinear material on initially monochromatic waves.	34
3.3	Velocity profile of horizontal component (a) and vertical component (b) at $z = 0$ for $f_a=2.5\text{MHz}$, $f_b=2.5\text{MHz}$, $\alpha = 6e^{-4}\text{Np/m}$ and including the first 120 harmonics.	53
3.4	Velocity profile of horizontal component (a) and vertical component (b) at $z = 0$ for $f_a=2.5\text{MHz}$, $f_b=1.75\text{MHz}$, $\alpha = 6e^{-4}\text{Np/m}$ and including all frequency components up to a level of 120.	55
3.5	Velocity profile of horizontal component (a) and vertical component (b) at $z = 0$ for $f_a=2.5\text{MHz}$, $f_b=0.5\text{MHz}$, $\alpha = 6e^{-4}\text{Np/m}$ and including all frequency components up to a level of 120.	56
3.6	Amplitudes of the level 1 and 2 waves normalized to $b_{ICa} = 2b_{ICb} = 7.5e^{-10}\text{m}$ over propagation distance. The damping within is $6e^{-4}\text{Np/m}$ for fused quartz according to Table 3.2 and the frequency $f_a=2.5\text{MHz}$ is fix while f_b is given according to the FMR of a) 0.1, b) 0.6, c) 0.9. All frequency elements up to level 120 are included in the simulations.	58
3.7	Slope over propagation distance for different of the different frequency level 2 components normalized to their maxima and plotted over the frequency mixing ratio. The fundamentals and a) $f_{a,b}$ the center frequency $(f_a + f_b)/2$ are kept constant.	65

3.8	Acoustic nonlinearity parameter for aluminum of Table 3.3 calculated on four different ways for a)no diffraction and no attenuation, b)attenuation of 0.8Np/m and no diffraction, c)attenuation of 0.08Np/m and diffraction, d) attenuation of 0.8Np/m and diffraction.	74
4.1	Sketch of geometry, material and physics of FEM simulation model. .	77
4.2	Time domain signal in z -direction for mixing of 2.5 and 1MHz waves with an AMR of 1.5 at 5.5mm propagation distance in steel with increased nonlinearity by a factor of 150.	84
4.3	DFT plot of time domain signal of Figure 4.2 with a Hanning window applied and approximately back calculated to time domain amplitudes with Equation (158).	85
4.4	Workflow in processing of the time domain signal obtained within FEM.	85
4.5	Comparison of vertical displacement portions of the different frequency components of the two dimensional model (curves) with the FEM model (markers) for $f_a = 2.5\text{MHz}$ and a) $f_b = 1\text{MHz}$ and b) $f_b = 2\text{MHz}$. The maximum P-wave excitation is $15e^{-10}\text{m}$ for both fundamentals. Material nonlinearity within steel is increased by a factor of 150. . . .	87
4.6	Surface plot of vertical displacement for the FEM model for $f_a = 2.5\text{MHz}$ and a) $f_b = 1\text{MHz}$, b) $f_b = 2\text{MHz}$. The used setups are the same as used in Figure 4.5.	88
4.7	Comparison of vertical displacement portions of the different frequency components of the two dimensional model (curves) with the FEM model (markers) for $f_a = 2.5\text{MHz}$ and $f_b = 2\text{MHz}$. The maximum P-wave excitation is $15e^{-10}\text{m}$ for both fundamentals. Material nonlinearity within steel is increased by a factor of 150. The specimen depth is a) 0.5 and b) 2 times the depth used in Figure 4.5 plot b).	89
4.8	Comparison of vertical displacement portions of the different frequency components of the two dimensional model (curves) with the FEM model (markers) for $f_a = 2.5\text{MHz}$, $f_b = 2\text{MHz}$ and a maximum P-wave excitation of $15e^{-10}\text{m}$ for both fundamentals. Material nonlinearity within steel is increased by a factor of 150 and the wedge size is multiplied by a factor of a) 0.5 and b) 2 compared to the setup used in Figure 4.5 b).	91
4.9	Comparison of vertical displacement portions of the different frequency components of the two dimensional model (curves) with the FEM model (markers) for $f_a = 2.5\text{MHz}$, $f_b = 2\text{MHz}$ and P-wave excitation of $15e^{-10}\text{m}$ for both fundamentals. Material nonlinearity within steel is increased by a factor of a)10, b)1350. Otherwise the setups are identical as used in Figure 4.5b)	92

5.1	Concept of experimental Rayleigh wave mixing.	95
5.2	Transducer setup of experiments with view from the side.	96
5.3	Transducer setup of experiments with view from the top.	96
5.4	Technical devices used for experiments.	97
5.5	Plastic wedge with exciting transducer centered at 2.25 MHz.	99
5.6	Frequency response of air-coupled transducer from the Ultran group.	101
5.7	Oscilloscope showing measured signal of two mixed Rayleigh waves at 2.666667 and 1.866667 MHz.	102
5.8	Workflow in processing of the time domain signal obtained within experiments.	105
5.9	Measured time domain signal at 78mm propagation distance for mixing a 2.333333MHz with a 1.867777MHz wave both at 700mVpp output from the function generator.	106
5.10	DFT of the time domain signal of Figure 5.9 with an applied Hanning window.	106
5.11	Amplitudes of different frequency components over the propagation distance with the parameters of Figure 5.9.	107
5.12	β times x for different level 2 components.	108
5.13	Average fundamental amplitudes over propagation distance normalized to their maxima for different output voltages of the function generators. Trends denoted by arrows.	110
5.14	Average level 2 wave amplitudes over propagation distance normalized to their maxima for different output voltages of the function generators. Trends denoted by arrows.	111
5.15	Dependence of measured amplitudes on simultaneous scaling of the output voltage of both function generators. All components are normalized to the first data point. The fundamentals are plotted linearly whereas the square root is taken of all level two waves. The reference curve has a slope of one.	112
5.16	Value of linear fit for different β 's normalized to their maxima for different output voltages of the function generators.	113
5.17	Amplitude of sum frequency normalized to last data point for fixed center frequency at 2.1MHz for different f_b/f_a	115
5.18	Simplified diffraction model of Section 3.4 fitted to normalized experimental data shown in Figure 5.11.	116

LIST OF SYMBOLS AND ABBREVIATIONS

SYMBOL	DESCRIPTION
x, y, z	directions of coordinate system in reference or undeformed configuration
u_x, u_y, u_z	displacements in the direction of the reference system
v_x, v_y, v_z	particle velocity in the direction of the reference system
$\mathbf{k}_{(r)}$	wave vector (of Rayleigh wave)
$k_{(r)}$	wave number (of Rayleigh wave)
Φ, Ψ	scalar and vectorial potential from Helmholtz decomposition
c_p, c_s, c_r	wave speeds of P-wave, S-wave and Rayleigh wave
t	time
i	imaginary unit
λ	Lamé's first parameter
μ	Lamé's second parameter or shear modulus
K	bulk modulus
ρ	material density in reference configuration
A_1, A_2	arbitrary constants
ξ_p, ξ_s	constants dependent on P-wave, S-wave and Rayleigh wave speed
η	constant dependent on $x i_s$
$\omega_{(r)}$	angular velocity (of Rayleigh wave)
f	frequency
A, B, C	third order elastic constants here referred as Landau's constants
σ_{ij}	stress in j -direction at a surface with normal vector in i -direction
a_n, b_n	displacement amplitude measures for n -th frequency component
b_{dn}	displacement amplitude measure for diffracted n -th frequency component
v_n	particle velocity measure of n -th frequency component
v_{dn}	particle velocity measure for diffracted n -th frequency component

n, l, m	control variables
u_{xn}, u_{zn}	terms describing decay of Rayleigh wave over depth for n -th frequency component in x - and y -direction
ϕ	frequency mixing ratio of the fundamental wave
\bar{p}	propagation direction of generated wave with magnitude of unity
\mathcal{T}	kinetic energy
\mathcal{V}, \mathcal{W}	quadratic and cubic elastic energy terms of an isotropic solid
\mathcal{U}	total potential energy of the system
\mathcal{L}	Lagrangian
\mathcal{E}_2	second order elastic energy
\mathcal{E}_3	third order elastic energy
q_n	generalized coordinate
χ	factor that scales spatial integration boundaries
M	term containing material properties and wavenumber
β	acoustic nonlinearity parameter
S_{nlm}, S_{lm}, S'_{lm}	different representations of nonlinear interaction
α	attenuation coefficient
v_{IC}	initial condition in terms of particle velocity
b_{IC}	initial condition in terms of displacement
ν	Poisson's ratio
E	Young's modulus
u_{x0}, v_{x0}	initial amplitudes at $x = 0$ of u_x and v_x
x_d	discontinuity distance
θ	normalization factor
c_{ijkl}	fourth order elastic tensor
σ_{ij}	stress tensor
ϵ_{ij}	strain tensor

δ_{ij}	Kronecker delta
\mathbf{n}	outward normal unit vector on surface
Θ	angle between two mixed waves
Θ_d	small diffraction angle
\mathbf{A}	amplitude vector
\mathbf{p}	propagation direction
f	frequency
λ_w	wavelength
\mathbf{t}	surface traction
S	surface of closed region
dA	infinitesimal surface area
\mathbf{n}	outward normal vector on surface
V	volume of closed region
dV	infinitesimal volume element
\mathbf{f}	body force
∇	nabla operator
Θ	angle of wave in space
\mathbf{x}	Lagrangian coordinate
\mathbf{x}^*	Eulerian coordinate
P_{ij}	first Piola-Kirchhoff stress tensor
$s(y)$	Gaussian source
a_s	characteristic width of source

ABBREVIATION	DENOTATION
FFT	Fast Fourier Transform
DFT	Discrete Fourier Transform
FEM	Finite Element Method
P-wave	longitudinal or pressure wave
S-wave	shear wave, here typically vertically polarized
NDE	nondestructive evaluation
FMR	frequency mixing ratio
AMR	amplitude mixing ratio
SE	standard error
SVEA	slowly varying envelope approximation
PACE	partnership for an advanced computing environment

SUMMARY

Nonlinear mixing of two collinear, initially monochromatic, Rayleigh waves propagating in the same direction in an isotropic, nonlinear elastic solid is investigated: analytically, by finite element method simulations and experimentally.

In the analytical part, it is shown that only collinear mixing in the same direction fulfills the phase matching condition based on Jones and Kobett [13] for the resonant generation of the second harmonics, as well as the sum and difference frequency components caused by the interaction of the two fundamental waves. Next, a coupled system of ordinary differential equations is derived based on the Lagrange equations of the second kind for the varying amplitudes of the higher harmonic and combination frequency components of the fundamentals waves. Numerical results of the evolution of the amplitudes of these frequency components over the propagation distance are provided for different ratios of the fundamental wave frequencies. It is shown that the energy transfer is larger for higher frequencies, and that the oscillation of the energy between the different frequency components depends on the amplitudes and frequencies of the fundamental waves. Furthermore, it is illustrated that the horizontal velocity component forms a shock wave while the vertical velocity component forms a pulse in the case of low attenuation. This behavior is independent of the two fundamental frequencies and amplitudes that are mixed. The analytical model is then extended by implementing diffraction effects in the parabolic approximation. To be able to quantify the acoustic nonlinearity parameter, β , general relations based on the plane wave assumption are derived. With these relations a β is expressed, that is analog to the β for longitudinal waves, in terms of the second harmonics and the sum and the difference frequencies. As a next step, frequency and amplitude ratios

of the fundamental frequencies are identified, which provide a maximum amplitude of one of the second harmonics as well as the sum or difference frequency components to enhance experimental results.

Subsequently, the results of the analytical model are compared to those of finite element method simulations. Two dimensional simulations for small propagation distances gave similar results for analytical and finite element simulations. Consequently, this shows the validity of the analytical model for this setup.

In order to demonstrate the feasibility of the mixing technique and of the models, experiments were conducted using a wedge transducer to excite mixed Rayleigh waves and an air-coupled transducer to detect the fundamentals, second harmonics and the sum frequency. Thus, these experiments yield more physical information compared to the case of using a single fundamental wave. Further experiments were conducted that confirm the modeled dependence on the amplitudes of the generated waves.

In conclusion, the results of this research show that it is possible to measure the acoustic nonlinearity parameter β to quantify material damage by mixing Rayleigh waves on up to four ways.

CHAPTER I

INTRODUCTION

This chapter provides the a background on nonlinear acoustic nondestructive evaluation (NDE) concepts and states the objectives of the conducted research. Also an overview of related research results is given and gaps among existing research results are stated which this thesis seeks to fill. Finally, the structure of the thesis closes this chapter.

1.1 Motivation

NDE techniques using ultrasonic measurements have proven to be very useful in the last decades to reduce maintenance cost and to ensure a safe use of mechanical resources by monitoring the health of critical components. However, linear NDE techniques are not sensitive enough to detect micro structural changes as their scales are much smaller than the typical wavelengths used in an experiment using linear techniques [11]. Therefore, linear acoustic methods are usually limited to the detection of large scale damages like macro-cracks. That is why it has proven of value to apply nonlinear acoustical methods to obtain information about the micro structure of a material before damages like macro-cracks arise, as nonlinear material properties are sensitive to micro structural changes [12, 28, 38].

Nonlinear acoustic techniques make use of the measurement of higher harmonics of the fundamental wave which are generated in an initially monochromatic signal through the nonlinearity of the solid in which the waves propagate [5]. Here, the acoustic nonlinearity parameter β can be measured to characterize the micro structural state. In recent years a few different nonlinear acoustic techniques have been developed to quantify several nonlinear acoustic phenomena within a material. They can be used

to measure fatigue damage prior to crack initiation, as the dislocation density will be increased which is the only significant micro structural change for the damaged material. This leads to a generation of larger higher harmonics compared to an undamaged specimen which increases the acoustic nonlinearity parameter β and can be used to monitor the health state of the specimen. As dislocations have a relatively small influence on macroscopic material properties we rely on nonlinear techniques since linear methods are not sensitive enough as pointed out before [12, 38].

Furthermore, nonlinear ultrasound has been applied successfully to aging of materials [5] and stress corrosion cracking [42]. Nonlinear ultrasound can be used as well to measure irradiation damage as the underlying effects of increasing dislocation density and precipitate growth are quantifiable by nonlinear techniques. It has been demonstrated that irradiation of an undamaged specimen first increases the acoustic nonlinearity parameter β until a medium dose and from there on it will decrease again for higher doses [27].

This research focuses on nonlinear techniques using Rayleigh surface waves for a variety of reasons. Firstly, we can investigate components that we can only access from one side as excitation and detection of Rayleigh waves are conducted on the same side in contrast to bulk waves. Secondly, as Rayleigh waves are nondispersive and as the energy is concentrated within the surface as opposed to bulk waves, a stronger nonlinear interaction is obtained which helps to measure for example corrosion or fatigue damage more easily which usually starts in the surface. Thirdly, Rayleigh waves decay more slowly than bulk waves as they dissipate their energy less rapidly which is useful to investigate large components [9, 12, 38].

Recently, the nonlinear concept of measuring the second harmonic of a fundamental Rayleigh wave has been taken a step further by mixing of two Rayleigh waves, which has been experimentally applied in concrete [10] and demonstrated several advantages. Mixing of two Rayleigh waves produces not only higher harmonics of each

fundamental wave but also sum and difference frequencies of all harmonics (combination frequencies). The sum and difference frequencies and the second harmonics of the two fundamental waves can be measured to provide more physical information compared to the case of a single fundamental to quantify the material state. The various frequency components can have different advantages depending on the specific application and the available experimental equipment such as transducers with specific center frequencies. For example the difference frequency undergoes low attenuation and low scattering which is advantageous in materials with high attenuation such as concrete. Moreover, the difference frequency component is less sensitive to the contact condition between transducer and surface of the specimen. Finally, if the difference frequency component arises from the mixing of two high frequencies it is usually much larger compared to a one wave set up where the considered frequency of the difference component would be realized as the second harmonic of a much smaller fundamental wave in terms of frequency and energy assuming similar fundamental amplitudes.

1.2 Problem Statement

The objectives of this thesis are to understand, model, simulate and validate the mixing process of two collinear Rayleigh waves and the generation of higher harmonics as well as sum and difference frequencies to be able to better interpret experimental results. An additional goal is to identify of the frequency and amplitude ratios of the two fundamental frequencies, which provide a maximum amplitude of the considered frequency components to enhance experimental results. A final focus of this research is to show that and how the mixing technique can be used to characterize the acoustic nonlinearity parameter β .

1.3 Literature Review

The theoretical background used in the present paper to be able to model Rayleigh wave mixing reaches back several decades. In 1963 Jones and Kobett [13] published a paper on wave mixing in which they established resonance conditions to calculate the occurrence of strong scattered waves. In the same year Rollins [31] validated their theoretical results and detected the predicted scattered waves.

In 1973, Reutov [30] showed that the averaged variational principle can be used to consider multi wave interaction of surface waves. Moreover, the equations for the interactions of the different harmonics of a surface wave in an isotropic elastic medium have been discussed.

In 1981, Kalyanasundaram [14] has published a paper on nonlinear mixing of two co-directional Rayleigh waves. In this work the method of multiple scales is used including perturbation expansions considering the fundamental and second harmonics and the sum and difference frequency component. By satisfying solvability conditions a set of coupled nonlinear differential equations were obtained to perform numerical simulations.

In 1983, Kalyanasundaram presented a paper [17] about the mixing of two Rayleigh waves propagating in opposite directions. Here, it is stated that no mode coupling between the primary waves exists. Kalyanasundaram used an extension of the method of multiple scales in order to handle the singularity of the boundary condition matrices.

In 1985, Lardner [24] used an asymptotic theory of nonlinear Rayleigh waves to investigate the waveform distortion over propagation distance. Here, the formation of a shock in the horizontal velocity component is shown and a pulse shape is observed in the vertical velocity component.

In the same year David [8] obtained similar results and discovered that the displacement components do not become discontinuous as opposed to the velocity components. In the present thesis an approach highly based on the work of Zabolotskaya from 1991 [40, 41] will be presented. Zabolotskaya postulated the solution to be in the form of summation of the considered harmonics of a Rayleigh wave. Then a system of coupled differential equations is derived based on the Hamiltonian formalism to describe the dynamics of the slowly varying envelopes or amplitudes of the different harmonics.

In 1993, Shull et al. [33] worked with the model of Zabolotskaya to analyze the harmonic generation within Rayleigh waves. A year later Shull et al. published a paper on finite sized sources [34] extending the model of Zabolotskaya by incorporating diffraction effects in the parabolic approximation.

In 2009, non-collinear mixing techniques have been successfully applied to quantify plasticity and fatigue damage. Non-collinear mixing of two shear waves helps to control system nonlinearities [7].

In 2011 and 2012, the mixing of collinear P-waves and S-waves propagating in opposite directions has been used to measure the acoustic nonlinearity parameter [25, 26]. This allows to determine the acoustic nonlinearity and accordingly the damage of a material locally in the mixing zone of the involved waves. Thus, it has the potential to measure the spatial distribution of the acoustic nonlinearity to conduct more detailed non-destructive damage evaluations.

1.4 Gap Analysis

Considering the previous work, there are several gaps within the wave mixing field of Rayleigh waves which will be covered in this thesis. First of all, a model for the mixing process will be developed that does not only include the fundamental waves,

the second harmonics plus the sum and difference frequency components as in [14], but also a variable amount of higher harmonics and combination frequencies. A large number of frequency components is crucial for simulations with low attenuating materials and highly nonlinear effects such as shock formations. Also, a representation that allows for easy adjustment of the number of harmonics and combination frequencies considered, will be developed which ensures easy automation to set up the system of differential equations and no nonlinear boundary conditions have to be fulfilled [41]. Moreover, a model will be developed that does not assume slowly varying envelopes as opposed to many other papers [14–16, 40, 41], to make the solutions more accurate. Diffraction effects will be included in the Rayleigh wave mixing process which has not been done yet and general formulas to calculate the acoustic nonlinearity parameter β based on the second harmonics plus sum and difference frequency components will be developed. Multiple analytical and numerical investigations of the analytical model will be used to make draw conclusions about the effects of different amplitudes and frequencies of the fundamental waves and their ratios.

The analytical model is directly compared to a FEM model for validation purposes. Such a direct comparison has not been presented in the covered literature.

As in [10] the difference frequency component has been the focus of experimental Rayleigh wave mixing in concrete, this thesis will cover the measurement of both second harmonics plus the sum frequency and use aluminum to demonstrate the technique for a different material. Also an air-coupled transducer is used to detect the Rayleigh waves which is a relatively new approach in nonlinear acoustics.

1.5 Outline

The following section gives a short overview of the structure of the thesis. In Chapter 2 a short introduction is given to fundamental wave propagation concepts which are relevant for this thesis. Based on these concepts, in Chapter 3 a theoretical

mixing model for the interaction between the different harmonics and combination frequencies is derived and extended to a finite sized source. Numerical simulations are presented and relations for the calculation of the acoustic nonlinearity parameter β are presented. Hereupon, in Chapter 4 finite element method simulations are conducted and the results are compared to those of the analytical model. Furthermore, Chapter 5 covers an experimental validation of the practical feasibility of the Rayleigh wave mixing technique. Finally, the thesis is summarized and an outlook is given in Chapter 6.

CHAPTER II

FUNDAMENTALS OF WAVE PROPAGATION IN SOLIDS

This chapter provides an introduction to the fundamental concepts of wave propagation in solids which serve as a basis for further investigations. In the beginning definitions and necessary mathematical tools for the wave propagation theory are presented. As a next step, the linear theory is covered including the linear equations of motion of wave propagation in solids. This is followed by a discussion of several wave phenomena. Furthermore, P-wave, S-wave and Rayleigh wave theory will be discussed as well as nonlinear wave propagation concepts. The basic theories and concepts of this chapter can be found in various books and theses [1, 4, 6, 9, 11, 18, 20, 22, 32, 36, 37].

2.1 Problem Specific Definitions

To make discussions easier to read and write, several definitions will be used throughout this thesis as they were found useful although not always common:

Definition 2.1 (Labeling of Waves). *The two involved waves in the mixing process are labeled $wave_a$ and $wave_b$. The frequency, angular velocity and wavenumber of $wave_a$ are accordingly named as f_a , ω_a and k_a , which holds analogously for $wave_b$.*

Definition 2.2 (Frequency components). *Integer multiples of a fundamental frequency f_a are called higher harmonics, while the n th harmonic is nf_a with $n = 1, 2, 3, \dots$. The frequency component $f_a + f_b$ is called the sum frequency, $f_a - f_b$ the difference frequency and an arbitrary combination of frequencies f_a and f_b is called combination frequency and written as $nf_a \pm mf_b$ with $n = 1, 2, 3, \dots$ and $m = 1, 2, 3, \dots$. The inequality $f_a \geq f_b$ holds without loss of generality.*

Definition 2.3 (Ratios). *The ratio $\phi = f_b/f_a \leq 1$ is called the frequency mixing*

ratio (FMR). Analogously, the initial amplitude of wave_b denoted by b_{IC_b} divided by the initial amplitude of wave_a denoted by b_{IC_a} is called the amplitude mixing ratio (AMR).

Definition 2.4 (Level of Frequency Components). *The fundamental waves are “level 1” waves as they exist as initial conditions. All waves that will be generated directly out of the two fundamental Rayleigh waves are “level 2” waves. These consist of the sum frequency $f_a + f_b$, the difference frequency $f_a - f_b$, the second harmonic of wave_a $2f_a$ and the second harmonic of wave_b $2f_b$. The components generated out of the interaction of level 1 and level 2 waves are analogously “level 3” waves and “level 4” waves are components generated of level 1 and 3 or level 2 with level 2 components and so on.*

Note that this naming will serve to make the order of the discussed components clearer but of course there will be also an influence from higher to lower levels transferring typically small amounts of energy.

2.2 Mathematical Tools

2.2.1 Notation

Within this work different notations such as the vector notation and the indicial notation or a short form for partial derivatives as well as the standard form are used depending on which formulation is found to be useful in the specific equation. For example, indicial notation will be used if sums are involved and the indices are used as variables that go from one, over two to three. The according coordinates are x_1, x_2 and x_3 . However, within the work with specific components that do not use variable indices anymore we will stick to x, y , and z as they will help to prevent mistakes and are easier to read. Thus, $u_1 = u_x, u_2 = u_y$ and $u_3 = u_z$ will hold. Also, the symbol ∂_i denotes the partial derivative $\frac{\partial}{\partial x_i}$ in i -direction, where Lagrangian coordinates are used. The according formulation in the xyz -system will however only be written as

for example $\frac{\partial}{\partial x}$. This is also the case for partial derivatives in direction of generalized coordinates. Besides, Einstein notation will be used, which means that repeated indices are treated as a summation.

Finally, bold symbols represent vectors. In vector notation, $\nabla \times \mathbf{u}$ denotes the curl of \mathbf{u} , $\nabla \cdot \mathbf{u}$ the divergence and ∇^2 the Laplacian.

2.2.2 Gauss' Theorem

The Gauss' Theorem, also called divergence theorem, is used to relate a surface integral over a closed surface S to a volume integral over the volume V which is bounded by the surface S . Thus, Gauss' Theorem equates the flow through the surface S with the sources and sinks inside the volume V . It is essential to later develop Cauchy's equations of motion in Section 2.3.2 .

Theorem 2.1 (Gauss' Theorem). *Suppose the compact volume V is bounded by the piecewise smooth surface S , then we can write*

$$\int_V \partial_i u_i dV = \int_S u_i n_i dA, \quad (1)$$

where u_i denotes the components of the continuously differentiable vector field \mathbf{u} and n_i are the outward pointing components of the unit normal vector \mathbf{n} on the surface S .

2.2.3 Lagrangian Mechanics

For derivation of the equations of motion in Chapter 3 the Lagrange equations of the second kind for a conservative system will prove to be very useful. By problem specific choice of the generalized coordinates q_n we can find the equations of motion for our problem by modeling the kinetic and potential energy of the system as the active forces have a potential when conservation of energy holds. The Theorem is as follows:

Theorem 2.2 (Lagrange equations of the second kind). *Suppose the total kinetic energy of a conservative system is denoted by \mathcal{T} and the total potential energy by \mathcal{U} . Then, we can define the Lagrangian as*

$$\mathcal{L} = \mathcal{T} - \mathcal{U} \quad (2)$$

and the equations of motion follow as

$$\frac{d}{dt} \frac{\partial \mathcal{L}}{\partial \dot{q}_n} = \frac{\partial \mathcal{L}}{\partial q_n} \quad (3)$$

for N generalized coordinates q_n . The number of generalized coordinates matches the number of degrees of freedom.

2.2.4 Helmholtz Decomposition

In wave propagation it is often useful to write displacements in terms of potentials to arrive at easier representations of the considered equations. In order to do this, we can use the Helmholtz Theorem:

Theorem 2.3 (Helmholtz's Theorem). *We can decompose the vector field \mathbf{u} by introducing a scalar potential Φ and a vector potential Ψ in the form*

$$\mathbf{u} = \nabla\Phi + \nabla \times \Psi \quad \text{with} \quad \nabla \cdot \Psi = 0 \quad (4)$$

The zero-divergence condition is necessary to uniquely relate the three components of \mathbf{u} to the four components of the potentials.

2.3 Linear Wave Propagation

In the following linear constitutive relations and linear geometric relations will be used to obtain the linear elastic wave equation. P-waves, S-waves and Rayleigh waves emerge from this equation and will be discussed plus several important wave phenomena will be pointed out.

2.3.1 Linear Stress Strain Relationship

In the following we develop a stress strain relationship assuming a homogeneous and linear elastic medium. This is necessary to later develop the equations of motion for a propagating wave in a solid. Stress and strain are linked physically through constitutive relations. The linear stress strain relationship in the indicial notation is given as

$$\sigma_{ij} = c_{ijkl}\epsilon_{kl}. \quad (5)$$

Here, σ_{ij} is the stress tensor, c_{ijkl} the fourth order elastic tensor and ϵ_{kl} the linear strain tensor. The control variables i, j, k and l are one, two or three. In this general representation c_{ijkl} consists of 81 components. Furthermore, with the symmetry of the stress and strain tensors it follows

$$c_{ijkl} = c_{jikl} \quad \text{and} \quad c_{ijkl} = c_{ijlk}. \quad (6)$$

With further thermodynamical considerations one can find that

$$c_{ijkl} = c_{klij} \quad (7)$$

holds. It follows that only 21 components of c_{ijkl} are independent. Assuming an isotropic material with identical properties in all directions finally yields only two independent parameters in c_{ijkl} , which are called Lamé's parameters λ and μ . Thus, Equation (5) simplifies to

$$\sigma_{ij} = \lambda\delta_{ij}\epsilon_{kk} + 2\mu\epsilon_{ij} \quad (8)$$

where δ_{ij} denotes the Kronecker delta.

2.3.2 Cauchy's Equation of Motion

In order to be able to describe wave propagation in an elastic material, we need to derive the according equations of motion by using the principle of balance of linear

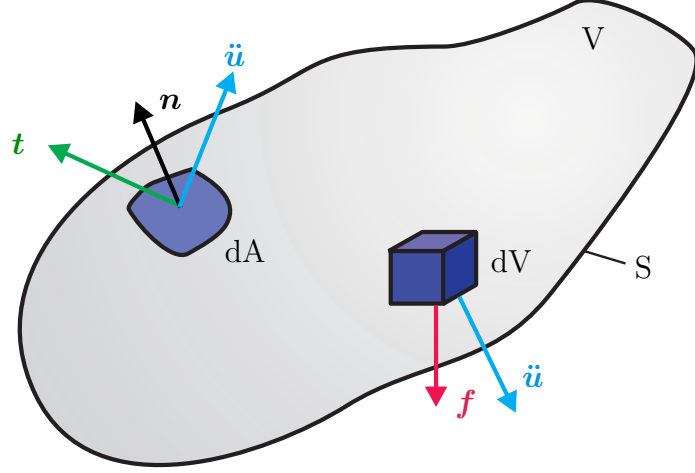


Figure 2.1: Principle of balance of linear momentum for Cauchy's first law of motion.

momentum. If we take into account the closed region of Figure 2.1 with surface S and volume V , we can use the fact that mechanical interaction of material points on opposite surfaces can be described entirely by a suitable surface tractions \mathbf{t} acting on the surface elements dA with outward normal directions \mathbf{n} . Moreover, each element dV of the considered body is influenced by a body force \mathbf{f} . Thus, by applying the balance of linear momentum for a linear problem we obtain

$$\int_S \mathbf{t} dA + \int_V \rho \mathbf{f} dV = \int_V \rho \ddot{\mathbf{u}} dV, \quad (9)$$

where \mathbf{u} denotes the particle displacement and ρ is the material density. When we substitute the Cauchy stress formula

$$t_i = \sigma_{ij} n_j \quad (10)$$

in Equation (9), we can apply Gauss' theorem of Section 2.2.2 to write the surface integral as a volume integral which yields

$$\int \partial_j \sigma_{ij} + \rho(f_i - \ddot{u}_i) dV = 0 \quad (11)$$

or

$$\rho \ddot{u}_i = \partial_j \sigma_{ij} + \rho f_i \quad (12)$$

as Equation (11) holds for each dV . Equation (12) is called Cauchy's first law of motion. Note that this equation of motion can also be obtained by considering the stress variations across a parallelepiped and making use of Newton's second law of motion as shown in [20].

2.3.3 Linear Wave Equation

In the following the goal is to write the equation of motion of Section 2.3.2 in terms of the displacement field \mathbf{u} to be able to make better physical interpretations of wave types and wave phenomena. First of all, we need to introduce the Lagrangian strain tensor which is based on material coordinates. With the displacement field \mathbf{u} and the current position \mathbf{x}^* , the Lagrangian coordinates follow as

$$\mathbf{x} = \mathbf{x}^* - \mathbf{u}. \quad (13)$$

Let us now use these coordinates and define the symmetric Lagrangian strain tensor

$$E_{ij} = \frac{1}{2}(\partial_j u_i + \partial_i u_j + \partial_i u_k \partial_j u_k). \quad (14)$$

If we assume small strains we can neglect the geometric nonlinearities and obtain the linear strain tensor as

$$\epsilon_{ij} = \frac{1}{2}(\partial_j u_i + \partial_i u_j). \quad (15)$$

The strain tensor describes the change in position of points within a continuum and is a relative measure in contrast to the displacement field \mathbf{u} which represents an absolute change. If we now neglect body forces and substitute the linear stress strain relationship of Equation (8) into Equation (12) we obtain the linear equations of motion as

$$\rho \ddot{u}_i = \partial_i \lambda \partial_k u_k + \partial_j \mu (\partial_i u_j + \partial_j u_i) + \lambda \partial_i \partial_k u_k + \mu \partial_i \partial_j u_j + \mu \partial_j \partial_j u_i. \quad (16)$$

This second order partial differential equation can be further simplified for a homogeneous material where all components of c_{ijkl} are constant and thus

$$\partial_i \lambda = \partial_i \mu = 0, \quad (17)$$

where the nabla operator denotes the gradient. As a result, for a homogeneous and isotropic material the elastic wave Equation (16) can be written as

$$\rho \ddot{u}_i = (\lambda + \mu) \partial_j \partial_i u_j + \mu \partial_j \partial_j u_i. \quad (18)$$

or in vector notation

$$\rho \ddot{\mathbf{u}} = (\lambda + \mu) \nabla \nabla \cdot \mathbf{u} + \mu \nabla^2 \mathbf{u}. \quad (19)$$

Equation (19) can be further simplified in two easier equations. On the one hand, if we take the divergence of both sides and substitute the Helmholtz Theorem of Equation (4) for u_i and use the fact that

$$\nabla \cdot \mathbf{u} = \nabla^2 \Phi, \quad (20)$$

we get an equation that only depends on the scalar potential Φ as

$$\nabla^2 \Phi - \frac{1}{c_p^2} \ddot{\Phi} = 0. \quad (21)$$

Here, $c_p = \sqrt{(\lambda + 2\mu)/\rho}$ holds. If we analogously take the curl of Equation (19), apply the Helmholtz Theorem and use the fact that

$$\nabla \times \mathbf{u} = -\nabla^2 \Psi, \quad (22)$$

we get

$$\nabla^2 \Psi - \frac{1}{c_s^2} \ddot{\Psi} = 0, \quad (23)$$

with $c_s = \sqrt{\mu/\rho} < c_p$.

2.3.4 P-waves and S-waves

In the following the theory of P-waves and S-waves will be covered as they make up the basic components of the Rayleigh waves that are mixed later. In the case both Φ is zero within Equation (21), we have a divergence free displacement field and the obtained wave will travel with the speed c_s and is called equivoluminal, distortional, secondary, transversal, shear wave or S-wave. Similarly, if Ψ equals zero in Equation (23), we obtain an irrotational wave traveling with c_p , also called primary, longitudinal, pressure wave or P-wave. Thus, we can see that the potentials in the Helmholtz decomposition are directly related to P-waves and S-waves namely

$$\mathbf{u} = \underbrace{\nabla\Phi}_{\substack{\text{longitudinal} \\ \text{component}}} + \underbrace{\nabla \times \Psi}_{\substack{\text{shear} \\ \text{component}}} . \quad (24)$$

Now, we will have a look on how P-waves and S-waves are related to plane waves. Analogously to the well-known D'Alembert solution of the one dimensional wave equation, we can express a plane wave solution in three dimensions by

$$\mathbf{u} = \mathbf{A}f(\mathbf{p}\mathbf{x} - ct) \quad (25)$$

where \mathbf{A} is the vector of amplitudes, and \mathbf{p} within the function f is the direction of wave propagation of unity magnitude. Furthermore, c is a wave speed, \mathbf{x} denotes the position and t the time. This plane wave has a constant frequency, a constant amplitude and its wavefronts occur on parallel planes standing vertically on the wave propagation direction. If we plug Equation (25) into the Equation of motion (19) we obtain similar to [37]

$$\rho c^2 \mathbf{A} = (\lambda + \mu)(\mathbf{p} \cdot \mathbf{A})\mathbf{p} + \mu \mathbf{A}. \quad (26)$$

According to [9] we can then write the determinant of coefficients as

$$(\lambda + 2\mu - \rho c^2)(\mu - \rho c^2)^2 = 0. \quad (27)$$

The roots of this equation are exactly c_p and c_s as defined previously. This shows, that a plane wave will travel either with c_p or c_s .

To obtain information about the spatial characteristics of these two different types of waves, we look at two special cases. First we assume that the amplitude \mathbf{A} points in the wave propagation direction \mathbf{p} . This leaves us with

$$\rho c^2 \mathbf{A} = (\lambda + \mu) \mathbf{A} + \mu \mathbf{A} \quad (28)$$

which gives $c = c_p$. The fact that the propagation direction of a P-wave is also the direction of displacement is the reason why the P-wave is also called longitudinal wave. Moreover, if we assume that the wave propagation direction \mathbf{p} is perpendicular to the direction of the displacement amplitude \mathbf{A} we obtain

$$\rho c^2 \mathbf{A} = \mu \mathbf{A}. \quad (29)$$

and realize that this holds for $c = c_s$. Thus, the perpendicular polarization is the reason for the name transversal wave for the S-wave. We can have two types of S-waves, a vertical SV-wave and a horizontal SH-wave, but we will denote vertical shear waves only as S-waves in the following.

If we take a closer look at the definition of plane waves we can see that it is fulfilled by simple sine and cosine functions

$$\mathbf{u} = \mathbf{A} \sin(\mathbf{k}\mathbf{x} - \omega t) \quad (30)$$

at a constant frequency ω , with the wave vector \mathbf{k} pointing in the direction of propagation. Besides,

$$c = \frac{\omega}{|\mathbf{k}|} = \frac{2\pi f}{|\mathbf{k}|} = \lambda_w f \quad (31)$$

is the wave speed. Here, f denotes the frequency and λ_w the wavelength. Equation (30) describes a harmonic plane wave which is a central wave type in nonlinear measurements and especially in the finite element method (FEM) simulations and experiments presented in this thesis.

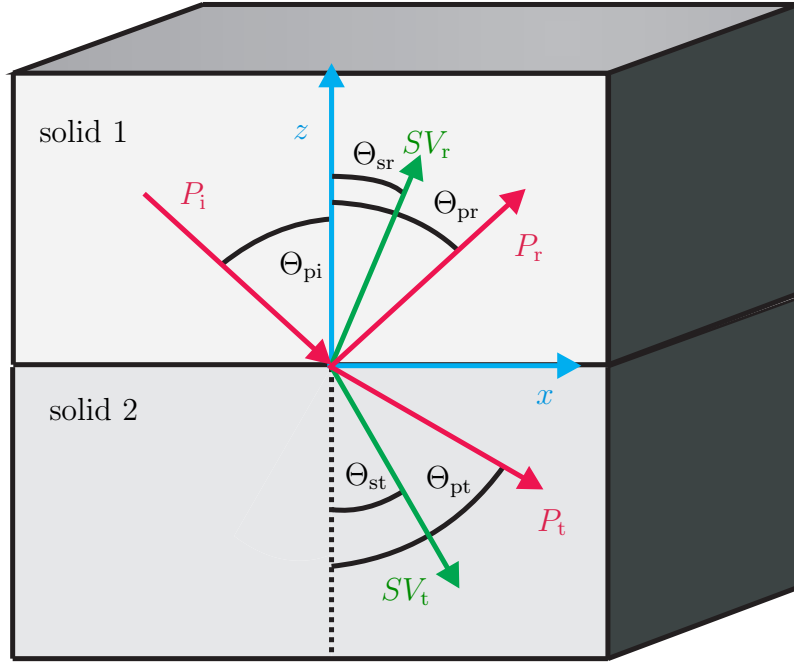


Figure 2.2: Reflection and transmission of an incident P-wave at a solid-solid boundary.

2.3.5 Refraction, Reflection and Transmission

In order to conduct and interpret experiments and FEM simulations, we need to consider the phenomena of refraction or Snell's Law as well as reflection and transmission. They will be important for Rayleigh wave generation according to Section (2.3.6.1) and wherever we deal with bounded media.

Now, consider the setup of Figure 2.2. As we can see, an incident P-wave at a solid-solid boundary results in reflected and transmitted P-waves as well as reflected and transmitted vertical S-waves also called SV-waves. Thus, there is a mode conversion between P- and SV-waves for angles different from zero degree incidence. Note, that this analogously holds for incident vertical S-waves, but for horizontally polarized (in y -direction) S-waves or just SH-waves, we do not have a mode conversion to other wave types independent of the angle of incidence. For angles of 0° we do not have mode conversions for all three wave types.

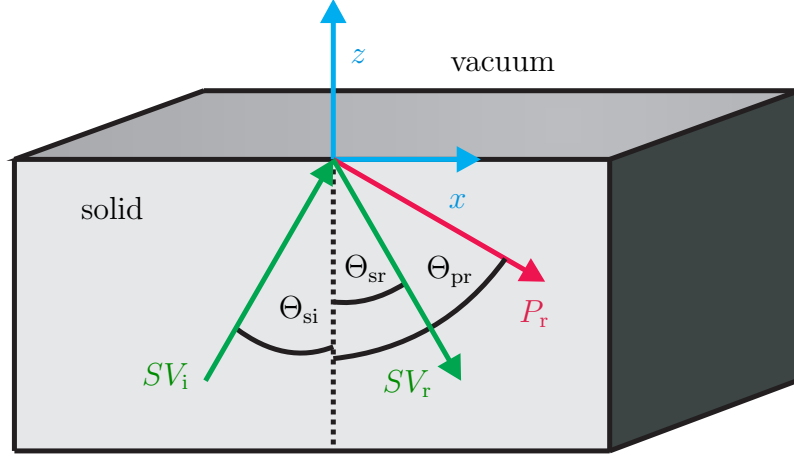


Figure 2.3: Reflection of an incident SV-wave at a stress free boundary.

The angles of the waves are related by the refraction or Snell's law as

$$\frac{\sin \Theta_{pi}}{c_{p1}} = \frac{\sin \Theta_{pr}}{c_{p1}} = \frac{\sin \Theta_{pt}}{c_{p2}} = \frac{\sin \Theta_{sr}}{c_{s1}} = \frac{\sin \Theta_{st}}{c_{s2}}, \quad (32)$$

where the second index of the wave velocities denotes solid 1 or 2. Thus, $\Theta_{pi} = \Theta_{pr}$ holds. This principle is fundamental to design the needed wedges for the wedge excitation of Rayleigh waves.

However, in the FEM simulation and experiments conducted in this thesis we are also confronted with stress free surfaces, as the considered Rayleigh waves are confined to free surfaces which can be idealized as a solid-vacuum interface as shown in Figure (2.3). Here, we see that we only have reflected waves which can be calculated with stress continuity at the boundary, but we do not have transmitted waves anymore. Note that $\Theta_{si} = \Theta_{sr}$ holds now. If we increase the incident SV-wave we can see that the reflected P-wave will finally travel along the surface in a 90° angle for

$$\sin \Theta_{si} = \frac{c_s}{c_p}, \quad (33)$$

where Θ_{si} is also called critical angle. If we further increase this angle of incidence, the P-wave will become evanescent. This effect can also appear in the solid-solid setup when the wave speeds of the considered wave components of solid 2 are faster

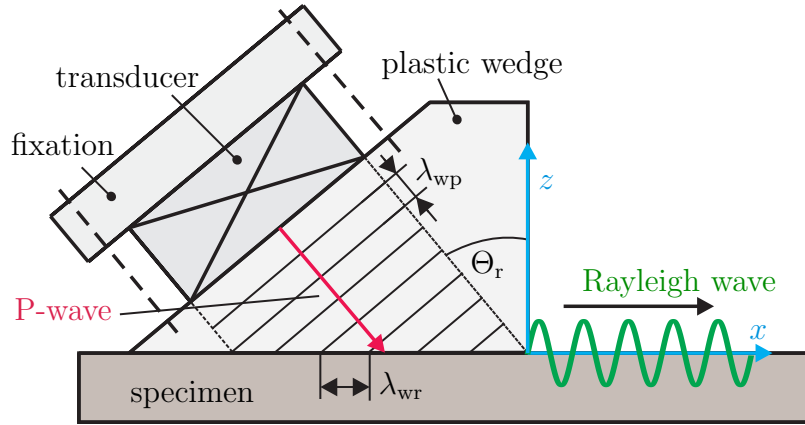


Figure 2.4: Generation of a Rayleigh wave with the wedge excitation method.

than of solid 1 or if we also consider incident SV-waves. This leads us now to the topic of the well-known evanescent Rayleigh waves.

2.3.6 Linear Rayleigh Waves

Rayleigh waves are named after Lord Rayleigh who was the first to investigate them. Rayleigh waves are closely confined to the surface and therefore also called Rayleigh surface waves. They travel with the constant velocity c_r independent of the frequency, meaning they are nondispersive and their phase and group velocity are the same. Also, Rayleigh waves travel even slower than the S-waves and decay rapidly with increasing depth.

2.3.6.1 Rayleigh Wave Generation

For the FEM simulation and the experiments in Chapters 4 and 5 it will be crucial to understand the generation of Rayleigh waves. In this thesis we excite Rayleigh waves with the wedge method according to Figure 2.4. Here, a piezoelectric transducer excites a P-wave in a plastic wedge. As the plastic wedge has a relatively low wave speed compared to the specimen which consists for example of metal, we can excite a surface wave in the specimen if the angle of incidence is chosen according to Snell's

law as

$$\sin \Theta_r = \frac{c_{\text{pwedge}}}{c_r} \quad (34)$$

for $c_{\text{pwedge}} < c_r$ with the Rayleigh wave speed c_r to be determined. The wavelengths of the P-wave and Rayleigh wave are denoted by λ_{wp} and λ_{wr} .

The illustrated wedge method is conducted in the experiments in an analogous way with an air-coupled transducer where the surrounding air works as a wedge to detect the Rayleigh wave. Thus, the Rayleigh wave “leaks” as a P-wave into the air which can be measured by sensitive equipment.

2.3.6.2 Rayleigh Wave Equation

To be able to understand experiments better it is indispensable to have a good model of the investigated subject. Thus, we will start by modeling linear Rayleigh waves with the linear stress strain relationship for homogeneous, isotropic and elastic solids according to Equation (8).

The derivation of the Rayleigh wave equations can be found in many textbooks like [1, 9, 36]. However, we shall review the most important steps in order to make the resulting Rayleigh wave forms and the notation more comprehensive as they will make the basis for Chapter 3. Now, consider an isotropic, elastic solid in the half-space $z < 0$ as defined in Figure 2.5 at which u_x and u_z describe the displacement in x and z -direction. Thus, we assume $u_y = 0$ and all derivatives in y -direction are also zero. As the Rayleigh wave is a surface wave the presence of the boundary at $z = 0$ is necessary for its existence. Furthermore, assuming a semi-infinite media which enables us to neglect all kinds of reflections for the theory. Similar to Section 2.3.3, we can simplify the derivation of the Rayleigh wave displacements by making use of the Helmholtz decomposition of the displacement field in a scalar potential Φ and a vector potential Ψ , which are again directly related to the P-wave and S-wave component as shown in Equation (24). As we assume that the two dimensional

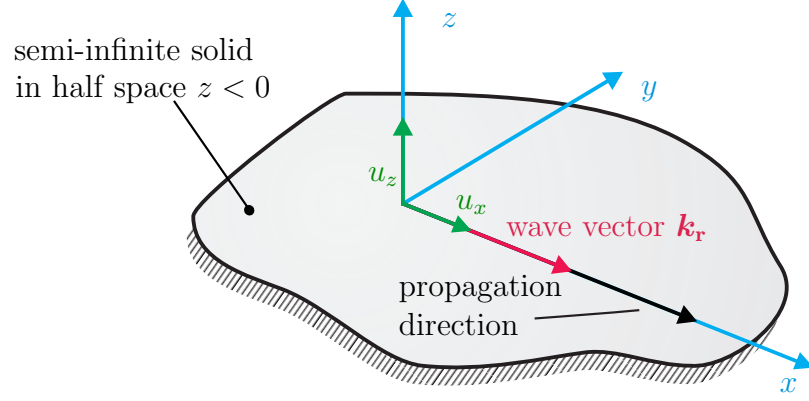


Figure 2.5: Propagation of an evanescent Rayleigh wave in an semi-infinite elastic solid with wave vector \mathbf{k}_r .

Rayleigh wave propagates along the x -axis, the vectorial potential Ψ simplifies to a scalar potential Ψ

$$\Psi = \begin{pmatrix} 0 \\ \Psi \\ 0 \end{pmatrix}. \quad (35)$$

The Rayleigh wave can consequently be regarded as a combination of P-waves and vertically polarized S-waves. As we know that Rayleigh waves have an evanescent nature in z -direction, we can write the general solution form of the potentials with a real exponent in z as

$$\Phi = A_1 \underbrace{e^{\sqrt{k_r^2 - \frac{\omega^2}{c_p^2}} z}}_{\text{evanescent}} e^{i(k_r x - \omega t)} \quad (36)$$

$$\Psi = A_2 \underbrace{e^{\sqrt{k_r^2 - \frac{\omega^2}{c_s^2}} z}}_{\text{evanescent}} e^{i(k_r x - \omega t)} \quad (37)$$

which fulfill the wave equations (21) and (23). At this, ω and k_r denote the the angular velocity and wavenumber of the Rayleigh wave and are related by $\omega = c_r k_r$. A_1 and A_2 are arbitrary amplitudes. Note, that the solutions with increasing exponential

functions have been ignored as they are physically not meaningful. Let us now define

$$\xi_p = \left(\sqrt{k_r^2 - \frac{\omega^2}{c_p^2}} \right) / k_r = \sqrt{1 - \frac{c_r^2}{c_p^2}} \quad (38)$$

$$\xi_s = \left(\sqrt{k_r^2 - \frac{\omega^2}{c_s^2}} \right) / k_r = \sqrt{1 - \frac{c_r^2}{c_s^2}} \quad (39)$$

which will help to simplify the equations later on. By using Equation (4) we can now express the displacement components as

$$u_x = k_r \left(iA_1 e^{\xi_p k_r z} - \xi_s A_2 e^{\xi_s k_r z} \right) e^{i(k_r x - \omega t)} \quad (40)$$

$$u_z = k_r \left(\xi_p A_1 e^{\xi_p k_r z} + iA_2 e^{\xi_s k_r z} \right) e^{i(k_r x - \omega t)} \quad (41)$$

and the stress components as

$$\begin{aligned} \sigma_{zz} = k_r^2 \left[\lambda \left(-A_1 e^{\xi_p k_r z} - i\xi_s A_2 e^{\xi_s k_r z} \right) \right. \\ \left. + (\lambda + 2\mu) \left(\xi_p^2 A_1 e^{\xi_p k_r z} + i\xi_s A_2 e^{\xi_s k_r z} \right) \right] e^{i(k_r x - \omega t)} \end{aligned} \quad (42)$$

$$\begin{aligned} \sigma_{zx} = \mu k_r^2 \left[\left(i\xi_p A_1 e^{\xi_p k_r z} - \xi_s^2 A_2 e^{\xi_s k_r z} \right) \right. \\ \left. + \left(i\xi_p A_1 e^{\xi_p k_r z} - A_2 e^{\xi_s k_r z} \right) \right] e^{i(k_r x - \omega t)} \end{aligned} \quad (43)$$

Note that the first index of the stress components denotes the normal direction of the considered surface and the second index denotes the direction of the force related to the stress. For further simplification we can eliminate λ out of Equation (42) by making use of

$$\begin{aligned} -\lambda + (\lambda + 2\mu)\xi_p^2 &= -\lambda \frac{c_r^2}{c_p^2} + 2\mu \left(1 - \frac{c_r^2}{c_p^2} \right) \\ &= 2\mu - (\lambda + 2\mu) \frac{c_r^2}{c_p^2} = 2\mu - \mu \frac{c_r^2}{c_s^2} = \mu \left(1 + \xi_s^2 \right) \end{aligned} \quad (44)$$

With Equation (44) and the boundary conditions for the stress free surface

$$\sigma_{zz}|_{z=0} = 0 \quad (45)$$

$$\sigma_{zx}|_{z=0} = 0 \quad (46)$$

we obtain the following characteristic equations for the Rayleigh wave

$$(1 + \xi_s^2) A_1 + 2i\xi_s A_2 = 0 \quad (47)$$

$$(1 + \xi_s^2) A_2 - 2i\xi_p A_1 = 0. \quad (48)$$

From these equations we can find the ratio A_1/A_2 as

$$\frac{A_1}{A_2} = -\frac{2i\xi_s}{1 + \xi_s^2} = \frac{1 + \xi_s^2}{2i\xi_p}. \quad (49)$$

Now, we define

$$\eta = -\frac{2\xi_s}{1 + \xi_s^2} \quad (50)$$

and substitute Equation (50) into Equation (49) which yields

$$\frac{A_1}{A_2} = i\eta = -\frac{\xi_s}{i\eta\xi_p} \implies \eta^2 = \frac{\xi_s}{\xi_p} \quad (51)$$

from which we can calculate the Rayleigh wave velocity c_r by plugging Equations (38),(39) and (50) in Equation (51). The Rayleigh wave speed depends on the considered material but is typically close to $0.9c_s$ and independent of the frequency.

As a next step, we can simplify the displacement terms by canceling out the common k_r terms, presenting all parts with a positive sign, shifting all imaginary numbers to one equation and by writing everything in dependence of only one variable amplitude. To perform these manipulations, we first take A_1 as a function of A_2 obtained in Equation (51) and plug it into the displacement Equations (40) and (41). Secondly, we define a new amplitude b_1 which is related to A_2 as

$$A_2 = \frac{-ib_1}{k_r}, \quad (52)$$

which yields the displacements of the Rayleigh wave as

$$u_x = ib_1 (\eta e^{\xi_p k_r z} + \xi_s e^{\xi_s k_r z}) e^{i(k_r x - \omega t)} \quad (53)$$

$$u_z = b_1 (\xi_p \eta e^{\xi_p k_r z} + e^{\xi_s k_r z}) e^{i(k_r x - \omega t)}. \quad (54)$$

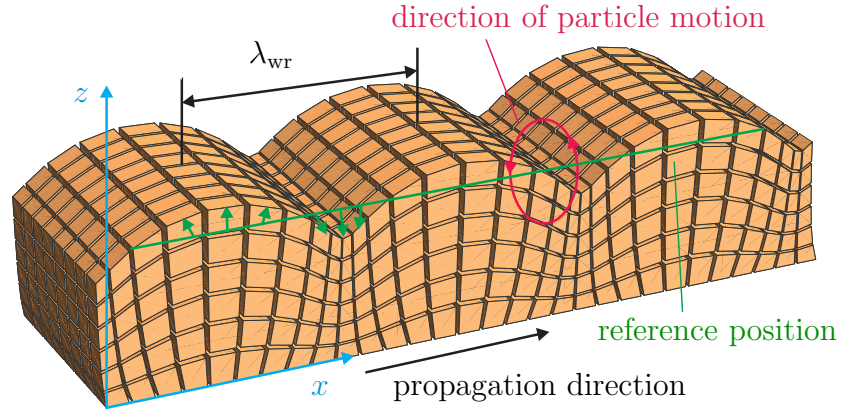


Figure 2.6: Three dimensional model from [39] of a Rayleigh wave propagating through a solid.

This corresponds to the representation in [41] and will help to easily compare the mixing model of Chapter 3 to the one wave model of Zabolotskaya which serves as a major basis in the analyses later on. From Equations (53) and (54) we can see that there is a phase shift of 90° between both displacements. This causes the material points of a solid subjected to a Rayleigh wave to move counterclockwise on an ellipsis on the surface when the wave travels from left to right as the vertical component is larger. The counterclockwise motion is illustrated in Figure (2.6). However, at about a fifth of a Rayleigh wave length away from the surface, the direction of particle motion reverses. In this three dimensional model from Wolfram Research [39] one can easily see that we have on the one hand a mix of P-waves and S-waves in a Rayleigh wave. The P-waves are the reason that the valleys are condensed and the hills are relatively wide. And the S-waves are responsible for the magnitude of the vertical displacement. On the other hand we can see the evanescent behavior of the wave, as the displacements decrease in the negative z -direction and have there maximum on the surface.

2.4 *Nonlinear Wave Propagation*

As stated in Chapter 1, nonlinear measurement techniques are relatively sensitive to changes in the micro structure of a material and thus are a promising concept

in the field of nondestructive evaluation. As pointed out in Chapter 1 reasons for the material nonlinearity are amongst others dislocations and precipitates. Nonlinear effects cause higher harmonics and combination frequencies in the case of mixing to be generated. From measuring the amplitudes of the involved waves typically over the propagation distance in the case of Rayleigh waves, we can get an insight about the micro structure of the material which helps to monitor the health of a specimen. As the nonlinear effects will play the major role in this thesis, the main concepts are outlined in the following. The nonlinear wave equation will be discussed and the acoustic nonlinearity parameter β defined for P-waves will be covered.

2.4.1 Derivation

To realize wave mixing we need to model nonlinear equations of motion i.e. energy up to the third order of approximation or higher. Therefore, we express the elastic energy density \mathcal{E} for isotropic and weakly nonlinear solids up to a third order approximation which is given by Landau and Lifshitz [22] as

$$\mathcal{E} = \mu E_{ij}^2 + \left(\frac{K}{2} - \frac{\mu}{3} \right) E_{kk}^2 + \frac{1}{3} A E_{ij} E_{ik} E_{jk} + B E_{il}^2 E_{kk} + \frac{1}{3} C E_{kk}^3. \quad (55)$$

Here, K denotes the bulk modulus, E is the Lagrangian strain tensor of Equation (14) plus A , B and C are third order elastic constants to describe the nonlinear elastic properties. A relation to other third order elastic constants can be found in [41] and [4]. Note, that by modeling the system based on such a strain energy density function we obtain a hyperelastic material, which will give us a nonlinear stress strain relationship. Note that all terms used in the following are expressed in Lagrangian coordinates. By plugging in the strain tensor in the expression of the elastic energy density \mathcal{E} , we obtain terms of an order higher than cubic as we consider also geometric

nonlinearities. If we neglect those, we arrive at the following formulation

$$\begin{aligned} \mathcal{E} = & \frac{\mu}{4} (\partial_j u_i + \partial_i u_j)^2 + \left(\frac{K}{2} - \frac{\mu}{3} \right) (\partial_k u_k)^2 + \left(\mu + \frac{A}{4} \right) \partial_j u_i \partial_i u_k \partial_j u_k \\ & + \left(\frac{B}{2} + \frac{K}{2} - \frac{\mu}{3} \right) \cdot \partial_k u_k (\partial_j u_i)^2 + \frac{A}{12} \partial_j u_i \partial_k u_j \partial_i u_k + \frac{B}{2} \partial_j u_i \partial_i u_j \partial_k u_k + \frac{C}{3} (\partial_k u_k)^3, \end{aligned} \quad (56)$$

which will yield quadratic equations of motion. According to [22], we obtain the first Piola-Kirchhoff stress tensor P_{ij} by using the relation

$$P_{ij} = \frac{\partial \mathcal{E}}{\partial (\partial_j u_i)}. \quad (57)$$

Thus, the stress can be obtained by derivation after the strains. Finally, to obtain the equation of motion when we apply a the formula similar to Cauchy's first law of motion from Equation (12), but now with the first Piola-Kirchhoff stress tensor instead of σ_{ij} and neglected body forces. This gives

$$\rho \ddot{u}_i = \partial_j P_{ij}. \quad (58)$$

By making use of Equations (56),(57) and (58), we can write the nonlinear wave equation as

$$\begin{aligned} \rho \ddot{u}_i - \mu \partial_j \partial_j u_i - (K + \mu/3) \partial_k \partial_i u_k = & (\mu + A/4) (\partial_j \partial_j u_k \partial_i u_k + \partial_j \partial_j u_k \partial_k u_i + 2 \partial_k \partial_j u_i \partial_j u_k) \\ & + (K + \mu/3 + A/4 + B) (\partial_i \partial_j u_k \partial_j u_k + \partial_k \partial_j u_j \partial_k u_i) + (K - 2/(3\mu) + B) (\partial_j \partial_j u_i \partial_k u_k) \\ & + (A/4 + B) (\partial_k \partial_j u_j \partial_i u_k + \partial_i \partial_j u_k \partial_k u_j) + (B + 2C) (\partial_i \partial_j u_j \partial_k u_k) \end{aligned} \quad (59)$$

according to [13] where the same third order elastic constants A, B and C have been used as in [22].

2.4.2 Acoustic Nonlinearity Parameter for P-waves

After deriving the fairly complex nonlinear wave equation, we can simplify the equations for the special case of a one dimensional P-wave which travels in x -direction with displacement u_x . As a result, all displacements or partial derivatives in the y -

and z -direction are zero. This gives us with the partial derivative notation for specific components

$$\begin{aligned}\rho\ddot{u} &= \rho c_p^2 \frac{\partial^2 u_x}{\partial x^2} + (3\lambda + 6\mu + 2A + 6B + 2C) \frac{\partial^2 u_x}{\partial x^2} \frac{\partial u_x}{\partial x} \\ \ddot{u} &= c_p^2 \frac{\partial^2 u_x}{\partial x^2} \left(1 - \beta \frac{\partial u_x}{\partial x}\right),\end{aligned}\tag{60}$$

with $\beta = -(3 + (2A + 6B + 2C)/(\rho c_p^2))$ being the acoustic nonlinearity parameter, which is only dependent on material properties. When we write β in Brugger notation with $C111 = 2A + 6B + 2C$ and $C11 = \rho c_p^2$ we can see that this is indeed the expression supported by the literature [2, 18].

As we want to quantify the acoustic nonlinearity parameter in experiments solely by measuring the amplitudes of the involved waves as we do not know the involved material properties for damaged materials, we need to derive an equation that expresses β as a function of the fundamental amplitude A_1 and the amplitude of the generated second harmonic A_2 . As only harmonic excitations will be used in this thesis, we assume the excitation to be of the form

$$u_{in} = A_1 \sin(\omega t - kx).\tag{61}$$

By making use of the perturbation approach [18] in a case of only one involved P-wave, we obtain the solution of the form

$$u_{out} = A_1 \sin(\omega t - kx) + \underbrace{\frac{\beta k^2 A_1^2 x}{8}}_{A_2} \sin(2\omega t - 2kx).\tag{62}$$

Thus, it follows

$$\beta = \frac{8A_2}{k^2 A_1^2 x}\tag{63}$$

and we can experimentally determine β . This section will later serve as a basis for the discussion on β for Rayleigh wave mixing in Section 3.5.

CHAPTER III

ANALYTICAL MODEL OF THE MIXING PROCESS

This chapter analyzes the nonlinear mixing of two collinear, initially monochromatic, Rayleigh waves propagating in the same direction in a nonlinear elastic solid. The following derivations are modifications and extensions of the work of Zabolotskaya et al. [33, 34, 40, 41] to account for the mixing process of Rayleigh waves.

The main purpose of this section is to model and analyze the dynamical behavior of the amplitudes of the involved frequency components over the propagation distance. First of all solution forms for nonlinear and mixed Rayleigh waves are postulated. As a next step, the energy of the system will be modeled up to the third order to take wave interactions into account. These interactions caused by the nonlinear material, lead to the generation of higher harmonics and combination frequencies over the propagation distance. Based on the modeled energy, the Lagrangian equations of second kind are used to derive a system of coupled second order differential equations describing the dynamics of amplitudes of the different frequency components.

Subsequently, numerical simulations of the derived equations will be conducted to analyze the effects caused by wave mixing. The goal is to analyze the behavior of the involved frequency components as a function of the propagation distance.

Then, the model will be extended to the case of a finite size source. The obtained diffraction effects are represented in a parabolic approximation.

Finally, the obtained results will be used to develop a framework to calculate the acoustic nonlinearity parameter β for mixed Rayleigh waves.

3.1 Two Dimensional Model

3.1.1 Modeling

3.1.1.1 Assumptions

In order to simplify the physical modeling to keep the model at a reasonable complexity and at the same time to obtain the essential results, several assumptions have to be made. They will come into play throughout this modeling section and are listed in the following:

- Semi-infinite solid medium is assumed in which Rayleigh waves propagate according to Figure (2.5).
- Isotropic material having the same properties in all spatial directions.
- Elastic material, no plastic deformations.
- Phase matching, which leads to a basic solution form presented in Section 3.1.1.3.
- Steady-state waves so that we can later neglect partial derivatives after the time variable.
- Weakly nonlinear material, yielding a precise solution for an elastic energy up to the third order.

3.1.1.2 Phase Matching of Rayleigh waves

The concept of phase matching deals with the correct choice of the phase of the involved waves to obtain a large energy flow to the generated waves, which is desired to make them practically useful or measurable. If we have no phase matching our generated waves will be small and tend to oscillate around a small amplitude level [28]. Thus, we have to choose the wavenumbers k and the directions of the mixed waves accordingly to obtain resonance as shown for the example of P- and S-waves

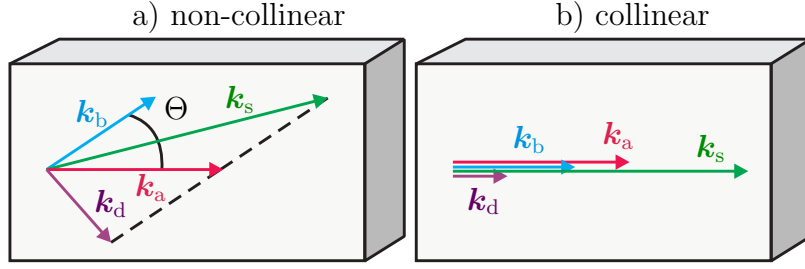


Figure 3.1: Phase matching for non-collinear and collinear mixing of two Rayleigh waves.

waves in [13].

As two wave mixing for Rayleigh waves is considered in this thesis, the phase matching concept will be explained for this specific case in the following. Phase matching for two Rayleigh waves which takes place close to the surface of a solid is illustrated in Figure (3.1), where the arrows in the collinear case have been shifted for a better recognizability. Here, \mathbf{k}_a and \mathbf{k}_b denote the wave vectors of the fundamental Rayleigh waves that are mixed and \mathbf{k}_s and \mathbf{k}_d are the sum and difference frequency that are generated through the nonlinear interaction. Note that the magnitude of a wave vector \mathbf{k} is the wavenumber k . As we can see from the non-collinear mixing case we have several directions involved which would make a nonlinear measurement of all components very complicated in contrast to the collinear or co-directional mixing, as we usually measure at many points over the propagation distance of the wave. Note that the direction of propagation, which is equal to the direction of the wave vector \mathbf{k} , of the difference frequency component drawn does not hold in general and has to be calculated case by case, unlike the direction of the sum frequency component. To determine the propagation direction of k_d , we assume in the following that the internal resonance condition of Jones and Kobett [13], holds similarly for Rayleigh waves as they consist of a P-wave and S-wave part. Also, we assume weak nonlinearity making the nonlinear effects small as they were in the derivation by Jones and Kobett. The terms internal resonance condition and phase matching condition are used in the same

way in the following and they can be stated as

$$\frac{(\omega_a \pm \omega_b)\mathbf{p}}{c} = \mathbf{k}_a \pm \mathbf{k}_b \xrightarrow{|p|=1} \frac{|\omega_a \pm \omega_b|}{c} = |\mathbf{k}_a \pm \mathbf{k}_b|. \quad (64)$$

where c is the wave speed and \mathbf{p} the propagation direction of the generated wave. Moreover, a positive sign denotes the sum frequency and a negative sign denotes the difference frequency component. The propagation direction of the generated wave is in general determined by

$$\frac{\mathbf{k}_a \pm \mathbf{k}_b}{\omega_a \pm \omega_b}. \quad (65)$$

As we consider the mixing of two fundamental Rayleigh waves with the same wave speed, the direction of propagation of the difference frequency component is determined by the higher fundamental frequency which leads to the directions drawn in Figure (3.1) for a dominant ω_a .

As we are interested in nonlinear ultrasonic measurements in this thesis, we want to compare nonlinearly generated Rayleigh waves to the fundamental Rayleigh waves. Thus, to obtain strong sum and difference frequencies, we want them to be generated directly out of the interaction of our fundamental Rayleigh waves \mathbf{k}_a and \mathbf{k}_b . Therefore, we have to set the wave speed c of the generated waves within Equation (64) equal to the Rayleigh wave velocity c_r as Rayleigh waves are non-dispersive, meaning the wave speed is independent of the frequency. When we square Equation (64) we obtain similar to [13]

$$\left(\frac{\omega_a \pm \omega_b}{c_r}\right)^2 = k_a^2 + k_b^2 \pm 2\mathbf{k}_a\mathbf{k}_b \quad (66)$$

which can be written as

$$(\omega_a \pm \omega_b)^2 = \omega_a^2 + \omega_b^2 \pm 2\omega_a\omega_b \cos \Theta, \quad (67)$$

where Θ is the angle between the fundamental waves. This yields the condition

$$1 = \cos \Theta, \quad (68)$$

which does only hold for $\Theta = 0^\circ$. As a result, we only have phase matching or resonance for collinear Rayleigh wave mixing in the same direction or co-directional. This is the only setup that is useful to get large enough generated level 2 Rayleigh waves by mixing two fundamental Rayleigh waves and will therefore be the basis for all further considerations. That collinear mixing in opposite directions does not lead to phase matching for Rayleigh waves is also supported by Kalyanasundaram [17]. As it has now been decided to use co-directional mixing, we can also test if we do not obtain P- or S-waves within the mixing process of the fundamentals. Therefore, we set $\Theta = 0$ leading to scalar wave vectors within Equation (64), which takes us to the condition

$$\frac{c_r}{c} = 1. \quad (69)$$

Thus, only Rayleigh waves will be generated for the interaction of the fundamentals. Besides, as one can also see in Figure (3.1), co-directional mixing helps to increase the wavenumber of the sum frequency component \mathbf{k}_s . It should also be pointed out that the concept of co-directional phase matching also applies to the generation of higher harmonics of one wave that propagates through a nonlinear material. Here, the wave will interact with itself according to [13, 18, 22] which causes the resonance condition to simplify to

$$\frac{\omega_a \pm \omega_a}{c_r} = k_a \pm k_a. \quad (70)$$

The solution with zero frequency is no wave and will be neglected as it is out of the scope of the present investigation. However, we also obtain the second harmonic of a wave. This means that the nondispersive characteristic of Rayleigh waves supports the nonlinear interactions within a single fundamental wave to generate higher harmonics.

3.1.1.3 Form of the Solutions of Nonlinear Rayleigh Wave Mixing

After discussing the phase matching condition of Section 3.1.1.2 it is now clear what kind of frequency components will be generated for co-directional mixing of two

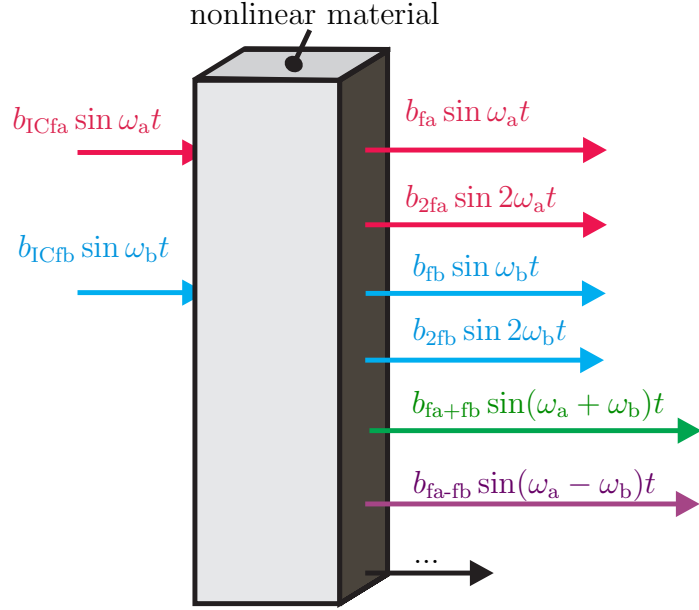


Figure 3.2: Sketch of the effect of a nonlinear material on initially monochromatic waves.

Rayleigh waves because of “internal resonance” that can develop a significant amplitude even in the case of weak nonlinearity. Due to the nonlinearity of the material, the two fundamentals will directly generate a sum and difference frequency component and second harmonics as presented in Figure 3.2 and in the discussions before. In the Figure, the coefficients in front of the sine terms denote amplitudes that will be discussed later on in a similar form. By generalizing the mixing of the two fundamentals we can see that all generated waves will interact again with all other waves leading to the formation of third harmonics and sum and difference frequencies which can be written as $2f_a \pm f_a$, $f_a \pm 2f_a$, $2f_a \pm 2f_a$, where f_a and f_b are the frequencies of the fundamental waves. This process will begin from new generating more and more frequency combinations in an analogous way until we obtain all kinds of harmonics and combination frequencies. Thus we obtain the components nf_a , mf_b and $nf_a \pm mf_b$ for $n = 1, 2, 3..$ and $m = 1, 2, 3..$. However, these components are generated through interactions in which non-fundamental components are involved. As these are small in realistic scenarios, they will generate even smaller components. This is the reason

why the further produced components are in general very small and difficult to measure. Therefore, this thesis will mostly focus only on the six frequency components of Figure 3.2.

As we have weak nonlinearity, the solution form of the nonlinear wave equation for two mixed nonlinear Rayleigh waves has to be close to the linear solution derived in Section 2.3.6 to approximately fulfill the linear wave equation in order that significant new frequency components can be generated [19, 41]. In order to fulfill this condition and the internal resonance condition we can take the formulation from Equations (53) and (54) for linear Rayleigh waves and write the solution form for nonlinear Rayleigh waves as a sum of all phase matched frequency components each close to the linear solution. This gives us similarly to [14, 41] the overall displacement, including a variable number of frequency components, as

$$u_x = \sum_n \underbrace{b_n(t)e^{-in\omega_a t}}_{a_n(t)} \cdot i \frac{n}{|n|} \underbrace{(\eta e^{n|\xi_p k_a z} + \xi_s e^{n|\xi_s k_a z})}_{u_{xn}} e^{ink_a x} \quad (71)$$

$$u_z = \sum_n \underbrace{b_n(t)e^{-in\omega_a t}}_{a_n(t)} \underbrace{(\xi_p \eta e^{n|\xi_p k_a z} + e^{n|\xi_s k_a z})}_{u_{zn}} e^{ink_a x}. \quad (72)$$

As each term in the summation operators for u_x and u_z does approximately fulfill the linear Rayleigh wave equation as the $b_n(t)$ change relatively slowly, the total sums will as well and is therefore a meaningful solution form. As we consider co-directional Rayleigh waves the vectorial wavenumbers have been already simplified to scalars. Also, each n describes a wave component i.e. a distinct wave with an individual frequency. Furthermore, negative n represent the corresponding complex conjugates to each positive n , while the propagation direction stays fixed into the positive x -direction. The term $n/|n|$ serves as signum function to ensure that $a_n^* = a_{-n}$ and $b_n^* = b_{-n}$ holds, respectively. The term $a_n(t)$ has been introduced here to later realize the slowly varying assumption of the complex amplitudes $b_n(t)$ more easily. Besides, according to Section 2.1 k_a and ω_a are the wavenumber and angular frequency of the

first fundamental wave denoted by “wave_a”. This wave_a mixes with wave_b while

$$\omega_a > \omega_b \quad \text{and} \quad k_a > k_b \quad (73)$$

hold without loss of generality.

What differentiates this formulation from [14] is that all different frequency components are pulled into only one sum. This not only makes the formulation shorter but will also help a lot to handle all further calculations as one got four times less expression to handle compared to a case where we consider pure wave_a terms, pure wave_b terms plus their sums and their differences in separated cases. Reducing the expressions to one summation involves a special definition of the control variable n . It does not simply go over a defined range of positive and negative integers as one might assume, but it takes values from a list which helps to keep the calculations as simple as possible. Thus, with the mixing ratio $\phi = k_b/k_a = \omega_b/\omega_a$ and $0 < \phi \leq 1$ n is defined as

$$n = \{1, 2, 3, \dots, \phi, 2\phi, 3\phi, \dots, 1 + \phi, 2 + \phi, 1 + 2\phi, 2 + 2\phi, \dots, |1 - \phi|, |2 - \phi|, |1 - 2\phi|, |2 - 2\phi|, \dots\}. \quad (74)$$

Note that negative n simply denote the negative version of this list. Also, the control variable n in an equation always represents a specific element of this list. Moreover, the elements of the list n with only integers and only multiples of ϕ are related to the fundamental and higher harmonic frequencies of wave_a and wave_b, respectively. The other terms are related to the combination frequencies. This means that for example $b_{1+\phi}$ describes the amplitude of the sum frequency. Besides, we will later only consider equations of motion with quadratic nonlinearity which means we will model the elastic energy up to the third order approximation. This implies that we will only consider combinations of two frequency components at once as pointed out in the phase matching conditions. This is a very good assumption in the case of weak nonlinearity. Thus, the elements of the list n in Equation (74) can be regarded as

subsequently generated by the interaction of always two waves.

However, if the energy is modeled to a higher approximation than the third order, we would obtain the same frequency elements as in list n , but mode coupling up to the third order would occur as well, i.e. interaction of three waves [23].

Another aspect is that the interaction of waves generates frequencies throughout the propagation that coincide with existing ones. For example the frequency element of the list n with 4 could be generated by 2 and 2 or by $2+2\phi$ and $2-2\phi$ and so on. This fact itself does not make much of a difference in this context. However, if frequencies arise more than once as a result of a special choice of ϕ , we obtain multiple elements in the list n . So e.g. for $\phi = 0.5$ the fundamental harmonic of wave_a would arise again in the second harmonic of wave_b. To account for that phenomenon, we can combine the multiple frequencies in Equations (71) and (72) to one component for each distinct frequency, which yields a reduction of different elements in the list n . This is necessary as we can only calculate as many different amplitudes b_n as we have individual frequencies, i.e. the number of generalized coordinates corresponds to the number of different components. Additionally, in the case the difference frequencies between wave_a and wave_b result in zero frequencies, i.e. static modes, they will be neglected as they are not relevant for the considered problem.

3.1.1.4 *Dynamic equations for varying amplitudes*

The following approach is an extension to the work done by Zabolotskaya [41]. Because of the generation of new frequency components and the interaction of all existing waves, the amplitudes of all involved frequency components is subject to dynamic variation and not constant anymore. We already stated a solution form for nonlinear Rayleigh waves in Section 3.1.1.3. What is now left to do is to develop the dynamic equations which can be used to solve for the unknown and varying amplitudes b_n in

Equations (71) and (72).

In the following, a coupled system of ordinary differential equations is derived based on the Lagrange equations of second kind for a conservative system for the varying amplitudes of the harmonic and combination frequency components of the fundamental waves. To be able to apply the Lagrangian formalism according to Section 2.2.3, we first need to calculate the Lagrangian of the system i.e. the kinetic and potential or elastic energy. The kinetic energy of the system can be calculated with [9]

$$\mathcal{T} = \frac{\rho}{2} \int \int \int \left(\dot{u}_x^2 + \overset{0}{\dot{u}_y^2} + \dot{u}_z^2 \right) dx dy dz \quad (75)$$

where the displacement in y -direction is equivalent to zero here, which yields a \dot{u}_y of zero. In this equation, ρ describes again the material or mass density in material coordinates. As only the different $a_n(t)$ in u_x and u_z are time varying we obtain the double summations

$$\dot{u}_x^2 = \sum_n \sum_m \dot{a}_n(t) \dot{a}_m(t) u_{xn} u_{xm} e^{i(n+m)k_a x} \quad (76)$$

and

$$\dot{u}_z^2 = \sum_n \sum_m \dot{a}_n(t) \dot{a}_m(t) u_{zn} u_{zm} e^{i(n+m)k_a x}. \quad (77)$$

Now, we can calculate the kinetic energy for a volume element. Therefore, we plug Equations (76) and (77) in Equation (75) and set the integration boundaries over z from $-\infty$ to 0. Besides, in the x -direction it is useful to integrate over a distance which contains full periods of all frequency elements as they are all periodic to simplify the problem. Thus, in a first step we choose the boundaries of x from 0 to a multiple of the wavelength of the fundamental frequency of wave_a which can be written as $\frac{2\pi\chi}{k_a}$ with the factor χ . The boundaries for y are chosen to make up a unit surface combined with the x -coordinate, i.e. $y \in \left[0, \frac{k_a}{2\pi\chi}\right]$. When integrating Equation (75) over x we can pull the integral into the double summation, which yields the common

factor

$$e^{i(n+m)k_a \frac{2\pi x}{k_a}} = \underbrace{e^{i(n+m)k_a 0}}_1 \quad (78)$$

after plugging in the boundaries. If the fundamental wave frequencies of wave_a and wave_b are

- decimals with a finite number of decimal places
- fractions of such decimals
- fractions of integers
- or if numbers with infinite decimal places cancel out in the FMR $\phi = k_b/k_a = \omega_b/\omega_a$

then we can always find a χ which ensures that $(n+m)\chi$ yields an integer. It is evident that we cannot find a common multiple of the wavelengths $\lambda_w = 2\pi/nk_a$ of the considered frequency components when we have different infinite numbers within the list n . However, the other cases are fairly general and cover all practical cases. Now, let us assume we are in a case where we can obtain an integer for $(n+m)\chi$. This finally makes the common factor in (78) zero. As a result, only the terms of the kinetic energy for which $n+m=0$ holds are non-zero as the according exponential terms in Equations (76) and (77) become unity and independent of x , which eventually yields a factor of one for the integrals over x and y . Additionally, the double summation can now be simplified to a single summation by replacing all m by $-n$. After integrating over z and putting the summations for \dot{u}_x^2 and \dot{u}_z^2 together in one summation we obtain the expression

$$\mathcal{T} = \frac{M}{4} \sum_n \frac{\dot{a}_n \dot{a}_{-n}}{|n|} \quad (79)$$

for the kinetic energy with

$$M = \frac{\rho}{k_a} \left(\xi_s + \frac{1}{\xi_s} + \eta^2 \xi_p + \frac{\eta^2}{\xi_p} + 4\eta \right) \quad (80)$$

which has the same form as in [41]. Note that $\dot{a}_n \dot{a}_{-n} = \dot{a}_n \dot{a}_n^* = |\dot{a}_n|^2$ which confirms that \mathcal{T} is a real valued quantity.

Now we need to derive the potential energy of the system up to the third order to take wave interactions into account. The potential energy consists solely of elastic energy and can be described by Equation (56). We divide this Equation on the one hand in a part quadratic in strain which characterizes the linear equations of motion and it will be called \mathcal{E}_2 . On the other hand, we divide it in a part cubic in strain which characterizes the nonlinear interactions within the nonlinear equations of motion and will be called \mathcal{E}_3 .

As we want to find the elastic energy of the volume element used for the calculation of the kinetic energy, we need to take the volume integral over the same domain of the according energy densities which can be written as

$$\mathcal{V} = \int_0^{\frac{2\pi\chi}{k_a}} \int_0^{\frac{k_a}{2\pi\chi}} \int_{-\infty}^0 \mathcal{E}_2 dx dy dz, \quad (81)$$

which will be called the second order elastic energy and the third order elastic energy

$$\mathcal{W} = \int_0^{\frac{2\pi\chi}{k_a}} \int_0^{\frac{k_a}{2\pi\chi}} \int_{-\infty}^0 \mathcal{E}_3 dx dy dz \quad (82)$$

will be called interaction energy in the following. There are basically three ways to calculate \mathcal{V} :

1. recognizing that \mathcal{V} is a homogeneous function and making use of the relation between kinetic and potential energy by the virial theorem as described in [23].
2. calculate the terms of \mathcal{E}_2 explicitly by inserting the expressions of Equations (71) and (72)
3. recognizing that \mathcal{V} is a homogeneous function and conducting several manipulations and using the linear equations of motion as pointed out in [41]

Here, the first and second way will be discussed. The first way is by far faster and easier, however the second way will be used to confirm the validity of the used approach and to test the result.

Let us now neglect \mathcal{W} for the moment. Then, the entire potential energy that is left is a quadratic function of the coordinates. Thus, the potential energy in this consideration is a homogeneous function of degree two and corresponds to the energy \mathcal{V} defined in Equation (81). As pointed out in [23] the mean values of the kinetic and potential energy are then identical by the virial theorem. Therefore, as the calculation of the kinetic energy \mathcal{T} involves integration over full spatial periods of all frequency elements, we can infer that $\mathcal{T} = \mathcal{V}$ holds. However, as the potential energy is only a function of position but not velocity we need to transform the kinetic energy of Equation (79) to yield the expression for the potential energy we are seeking. As we neglected energy terms of degree three and higher in this consideration, the linear equations of motion are governing which means that all b_n are constant. This yields

$$\dot{a}_n = -in\omega_a b_n e^{-in\omega_a t} = -in\omega_a a_n, \quad (83)$$

which holds analogously for \dot{a}_{-n} . Substituting Equation (83) in (79) results in

$$\mathcal{V} = \frac{M\omega_a^2}{4} \sum_n |n| a_n a_{-n}, \quad (84)$$

which now only depends on position instead of velocity. This result is identical to the result in [41] calculated with the third way listed before.

The second and direct way to calculate \mathcal{V} is now presented to show that the virial theorem indeed leads to the correct result and that by only considering \mathcal{E}_2 of the elastic energy it is in fact true that the linear equations of motion become the governing equations, which has been used in the first and third way to calculate \mathcal{V} . Therefore, we should arrive at the exact same result. When we plug Equations (71) and (72) in \mathcal{E}_2 we can see that for the same integration limits as for the kinetic energy we obtain only terms that are non-zero if the control variables of the involved double sums add

up to zero, i.e. $n + m = 0$ as before. Thus, the integration over x and y are only factors that cancel out. The resulting term after substituting in the displacements in \mathcal{E}_2 and integrating over x and y yields

$$\begin{aligned} \mathcal{V} = \sum_n \int_{-\infty}^0 \frac{1}{6} k_a^2 n^2 & \left((3K + 4\mu) (\eta e^{zk_a|n|\xi_p} + \xi_s e^{zk_a|n|\xi_s})^2 + 3\mu (\eta \xi_p e^{zk_a|n|\xi_p} + e^{zk_a|n|\xi_s})^2 \right. \\ & - 2(3K - 2\mu) (\eta e^{zk_a|n|\xi_p} + \xi_s e^{zk_a|n|\xi_s}) (\eta \xi_p^2 e^{zk_a|n|\xi_p} + \xi_s e^{zk_a|n|\xi_s}) \\ & + (3K + 4\mu) (\eta \xi_p^2 e^{zk_a|n|\xi_p} + \xi_s e^{zk_a|n|\xi_s})^2 + 6\mu (\eta \xi_p e^{zk_a|n|\xi_p} + e^{zk_a|n|\xi_s}) \\ & \left. \cdot (\eta \xi_p e^{zk_a|n|\xi_p} + \xi_s^2 e^{zk_a|n|\xi_s}) + 3\mu (\eta \xi_p e^{zk_a|n|\xi_p} + \xi_s^2 e^{zk_a|n|\xi_s})^2 \right) a_n a_{-n} dz. \end{aligned} \quad (85)$$

After integrating over z we obtain

$$\begin{aligned} \mathcal{V} = \sum_n \frac{k_a |n|}{12 \xi_p \xi_s} & \left(\eta^2 (3K + 4\mu) \xi_p^4 \xi_s + \eta^2 (3K + 4\mu) \xi_s \right. \\ & \left. + 2\eta \xi_p^2 \xi_s (8\eta\mu - 3\eta K + 12\mu \xi_s) + 3\mu \xi_p (8\eta \xi_s + \xi_s^4 + 6\xi_s^2 + 1) \right) a_n a_{-n}. \end{aligned} \quad (86)$$

If we use the relation $\xi_2^2(\lambda + 2\mu) - \lambda = \mu(\xi_1^2 + 1)$ from Equation (44), which will help to cancel all λ 's and compare the \mathcal{V} of Equations (84) and (86), we can find after several manipulations that both expressions are only equal if $\eta^2 = \frac{\xi_s}{\xi_p}$ holds. However, as this equation is exactly the Rayleigh wave Equation (51) it is obviously always true in the case of Rayleigh waves. This proves that all three ways to calculate \mathcal{V} lead to the same result and incorporate the same assumptions.

To obtain the interaction energy in Equation (82) we take again the direct way of plugging the displacements of Equations (71) and (72) into \mathcal{E}_3 to calculate the according strains. Here, the other ways are not applicable as they were based on negligible third order elastic energy which is exactly what we are about to calculate. Thus, we can calculate the involved sums and write the displacements u_1, u_2 and u_3 now as u_x, u_y and u_z with $u_y = 0$ and " $\frac{\partial}{\partial y} = 0$ ". As a result, we obtain the following

expression for the energy density

$$\begin{aligned}
\mathcal{E}_3 = & \left(\frac{A}{3} + B + \frac{C}{3} + \frac{K}{2} + \frac{2}{3}\mu \right) \left(\frac{\partial u_x}{\partial x} \right)^3 + \left(\frac{A}{4} + \frac{B}{2} + \frac{K}{2} + \frac{2}{3}\mu \right) \frac{\partial u_x}{\partial x} \left(\frac{\partial u_x}{\partial z} \right)^2 \\
& + \left(\frac{A}{2} + B + \mu \right) \frac{\partial u_x}{\partial x} \frac{\partial u_x}{\partial z} \frac{\partial u_z}{\partial x} + \left(\frac{A}{4} + \frac{B}{2} + \frac{K}{2} + \frac{2}{3}\mu \right) \frac{\partial u_x}{\partial x} \left(\frac{\partial u_z}{\partial x} \right)^2 \\
& + \left(B + C + \frac{K}{2} - \frac{\mu}{3} \right) \left(\frac{\partial u_x}{\partial x} \right)^2 \frac{\partial u_z}{\partial z} + \left(\frac{A}{4} + \frac{B}{2} + \frac{K}{2} + \frac{2}{3}\mu \right) \left(\frac{\partial u_x}{\partial z} \right)^2 \frac{\partial u_z}{\partial z} \\
& + \left(\frac{A}{2} + B + \mu \right) \frac{\partial u_x}{\partial z} \frac{\partial u_z}{\partial x} \frac{\partial u_z}{\partial z} + \left(\frac{A}{4} + \frac{B}{2} + \frac{K}{2} + \frac{2}{3}\mu \right) \left(\frac{\partial u_z}{\partial x} \right)^2 \frac{\partial u_z}{\partial z} \\
& + \left(B + C + \frac{K}{2} - \frac{\mu}{3} \right) \frac{\partial u_x}{\partial x} \left(\frac{\partial u_z}{\partial z} \right)^2 + \left(\frac{A}{3} + B + \frac{C}{3} + \frac{K}{2} + \frac{2}{3}\mu \right) \left(\frac{\partial u_z}{\partial z} \right)^3, \quad (87)
\end{aligned}$$

which consists of triple summations. When integrating over the volume used before to get the interaction energy \mathcal{W} we find a common factor similar to (78) which is

$$e^{i(n+l+m)2\pi\chi} - \underbrace{e^{i(n+l+m)k_a 0}}_1, \quad (88)$$

where n , l and m are control variables. Thus, for the same χ chosen for the kinetic energy, all terms included in \mathcal{W} will be zero, except for those for which $n + l + m = 0$ holds as the exponential terms will become unity and independent of x . When calculating the interaction energy \mathcal{W} , pretty large terms are involved. However, a simplified form is given in [41], which is based on $n + m + l = 0$ and therefore is only true for specific cases. Nevertheless, this term holds for all elements of the list n and can therefore be used analogously for the mixing case. Using this simplified expression, the interaction energy can then be written as

$$\mathcal{W} = \mu k_a^2 \sum_{n+l+m=0} S_{nlm} a_n a_l a_m, \quad (89)$$

with

$$S_{nlm} = -|nlm| \left(\frac{\alpha'}{|n|\xi_s + |l|\xi_s + |m|\xi_p} + \frac{\beta'}{|n|\xi_s + |l|\xi_p + |m|\xi_p} + \frac{\gamma'}{|n|\xi_p + |l|\xi_p + |m|\xi_p} \right). \quad (90)$$

The constants α' , β' and γ' are given in [41] and include solely material properties. In Equation (90) we can see that the denominators of the three terms are formed

through the integration of the exponential terms within u_{xn} and u_{zn} in Equations (71) and (72). Consequently, the first two terms describe interactions between S and P wave components of the Rayleigh waves. However, the third term does not only describe interactions between three P-wave components but also between three S-wave components as it is just a matter of what factor is taken into the γ' component.

Eventually, we can calculate the Lagrangian \mathcal{L} as

$$\mathcal{L} = \mathcal{T} - \mathcal{V} - \mathcal{W}. \quad (91)$$

Now, to be able to apply the Lagrangian equations of the second kind we need to choose generalized coordinates that completely describe the system. For practicality, we select the complex amplitudes a_n of each distinct wave frequency as generalized coordinates. If we know all a_n 's we can select any point on the xz -layer and simulate its behavior over time. This would be not the case if we chose b_n as coordinates as they are not generalized. The reason is that they alone do not describe the behavior of each point over time because the information about the oscillation $e^{-in\omega_a t}$ is missing. Within the a_n the n 's are as usual any element of a positive and negative list n , which is reduced by the multiple and zero frequencies that may appear. Thus, we obtain $2n$ generalized coordinates, n for the amplitudes of the different frequency components and n for their phases. Thus, the number of coordinates matches the number of degrees of freedom which is necessary for the coordinates to be generalized and independent of one another.

According to the Theorem 2.2 we now need to calculate the generalized momenta $\partial\mathcal{L}/\partial\dot{a}_n$ and $\partial\mathcal{L}/\partial a_n$, with \dot{a}_n being the generalized velocities. As the partial derivative of \mathcal{V} and \mathcal{W} with respect to the velocities \dot{a}_n are zero we can write

$$\frac{\partial\mathcal{L}}{\partial\dot{a}_{-n}} = \frac{\partial\mathcal{T}}{\partial\dot{a}_{-n}} = \frac{M}{2} \frac{\dot{a}_n}{|n|} \quad (92)$$

where negative n have been used in the partial derivatives to obtain positive n 's in the results. Also, a factor of two comes up when taking the derivative, as the element a_{-n} exists exactly twice in the sum within the kinetic energy, as n goes over positive and negative elements.

In contrast to this, the other element necessary for the Lagrange equations is only dependent on the potential energy and follows as

$$\frac{\partial \mathcal{L}}{\partial a_{-n}} = -\frac{\partial \mathcal{V}}{\partial a_{-n}} - \frac{\partial \mathcal{W}}{\partial a_{-n}}. \quad (93)$$

Let us now take the simple representation of \mathcal{V} according to Equation (84), which gives

$$\frac{\partial \mathcal{V}}{\partial a_{-n}} = \frac{M\omega_a^2}{2} |n| a_n. \quad (94)$$

Additionally, to be able to take the partial derivative of \mathcal{W} with respect to a_{-n} we write \mathcal{W} now as

$$\mathcal{W} = \mu k_a^2 \sum_{n=l+m} S_{nlm} a_{-n} a_l a_m, \quad (95)$$

where we replaced n by $-n$ within the sum, which is legitimate as n is only a control variable and appears solely as absolute values within S_{nlm} . Therefore, S_{nlm} is not affected. Consequently, we obtain

$$\frac{\partial \mathcal{W}}{\partial a_{-n}} = \mu k_a^2 \sum_{n=l+m} S'_{lm} b_l b_m e^{i(l+m)\omega_a t} \quad (96)$$

where S'_{lm} is similar to S_{nlm} and is defined as

$$\begin{aligned} S'_{lm} = -|nlm| & \left(\frac{\alpha'}{|n|\xi_s + |l|\xi_s + |m|\xi_p} + \frac{\alpha'}{|l|\xi_s + |n|\xi_s + |m|\xi_p} + \frac{\alpha'}{|l|\xi_s + |m|\xi_s + |n|\xi_p} \right. \\ & + \frac{\beta'}{|n|\xi_s + |l|\xi_p + |m|\xi_p} + \frac{\beta'}{|l|\xi_s + |n|\xi_p + |m|\xi_p} + \frac{\beta'}{|l|\xi_s + |m|\xi_p + |n|\xi_p} \\ & \left. + \frac{3\gamma'}{|n|\xi_p + |l|\xi_p + |m|\xi_p} \right). \end{aligned} \quad (97)$$

This ensures that all possible terms for a specific n are taken into account. Now, the last step for the equations of motion is the calculation of the time derivative

$$\frac{d}{dt} \frac{\partial \mathcal{L}}{\partial \dot{a}_{-n}} = \frac{M}{2} \frac{\ddot{a}_n}{|n|}. \quad (98)$$

With $a_n = b_n e^{-in\omega_a t}$ we obtain

$$\dot{a}_n = \underbrace{(\dot{b}_n - in\omega_a b_n)}_{v_n} e^{-in\omega_a t}, \quad (99)$$

where v_n is defined as the particle velocity amplitude of the different frequency components. Now, \ddot{a}_n follows as

$$\ddot{a}_n = (\ddot{b}_n - 2in\omega_a \dot{b}_n - n^2 \omega_a^2 b_n) e^{-in\omega_a t}. \quad (100)$$

As we derived all necessary terms, we can now state the Lagrange equations of second kind by substituting Equations (94), (96) and (100) as

$$\begin{aligned} \frac{d}{dt} \frac{\partial \mathcal{L}}{\partial \dot{a}_{-n}} &= \frac{\partial \mathcal{L}}{\partial a_{-n}} \\ \frac{M}{2|n|} (\ddot{b}_n - 2in\omega_a \dot{b}_n - n^2 \omega_a^2 b_n) e^{-in\omega_a t} &= -\frac{M\omega_a^2}{2} |n| b_n e^{-in\omega_a t} - \mu k_a^2 \sum_{n=l+m} S'_{lm} b_l b_m e^{i(l+m)\omega_a t}. \end{aligned} \quad (101)$$

If we now multiply $e^{in\omega_a t}$ to Equation (101), we can pull this exponential within the sum in the last term. As we changed the sign of all n within this sum, we have to do it now as well. This gives

$$\frac{M}{2|n|} (\ddot{b}_n - 2in\omega_a \dot{b}_n) = -\mu k_a^2 \sum_{n=l+m} S'_{lm} b_l b_m e^{i(l+m-n)\omega_a t}, \quad (102)$$

where $-M\omega_a^2 |n| b_n/2$ has been canceled on both sides. As $n = l + m$ holds, we finally obtain

$$\frac{M}{2|n|} (\ddot{b}_n - 2in\omega_a \dot{b}_n) = -\mu k_a^2 \sum_{n=l+m} S'_{lm} b_l b_m. \quad (103)$$

It is meaningful that now the dynamics of b_n is basically only dependent on the nonlinear terms, which are physically the reason why we obtain amplitude changes. If these nonlinear terms were not present and the initial derivatives of b_n zero, then the b_n terms would just stay constant. To obtain the variation of b_n in time and space, we write

$$\dot{b}_n = \frac{\partial b_n}{\partial x} \underbrace{\frac{dx}{dt}}_{=c_r} + \frac{\partial b_n}{\partial t} \quad (104)$$

If we now make the common assumption of periodic steady-state waves as stated in Section 3.1.1.1, then $\partial b_n / \partial t = 0$ [14, 41]. With this assumption we get

$$\ddot{b}_n = \frac{\partial^2 b_n}{\partial x^2} c_r^2 + \frac{\partial^2 b_n}{\partial x \partial t}, \quad (105)$$

where in $\partial^2 b_n / \partial x \partial t$ the order of the partial derivatives does not matter and it follows analogously $\partial^2 b_n / \partial x \partial t = 0$ because of steady-state waves, which yields

$$\ddot{b}_n = \frac{\partial^2 b_n}{\partial x^2} c_r^2. \quad (106)$$

Moreover, to stick to the notation similar to [41], we define

$$S_{lm} = -\frac{S'_{lm}}{|n|lm} \quad (107)$$

$$(108)$$

By plugging Equations (104),(106) and (107) into (103) one gets

$$\frac{M}{2|n|} \left(\frac{\partial^2 b_n}{\partial x^2} c_r^2 - 2in\omega_a \frac{\partial b_n}{\partial x} c_r \right) = \mu k_a^2 |n| \sum_{n=l+m} lm S_{lm} b_l b_m. \quad (109)$$

To be able to reproduce more realistic and numerically stable results, it is desirable to implement attenuation. Similarly to [4], attenuation of a constant wave amplitude b without influences from nonlinear effects can be written as

$$\frac{\partial b}{\partial x} = -\alpha b \quad (110)$$

where α is the attenuation coefficient. By realizing that the attenuation coefficient is a quadratic function of the frequency, we can now transfer this behavior to Equation (109) [4, 19, 22]. To get an easier representation, all factors in front of $\partial b_n/\partial x$ will be canceled out. This gives

$$\frac{i c_r}{2n\omega_a} \frac{\partial^2 b_n}{\partial x^2} + \frac{\partial b_n}{\partial x} = \frac{in\mu\omega_a}{Mc_r^3} \sum_{n=l+m} lmS_{lm}b_l b_m - \alpha n^2 b_n. \quad (111)$$

This is the final two dimensional system of simulation equations for the different amplitudes b_n in its most complex form. It represents a coupled system of second order ordinary differential equations with quadratic terms as the modeled energy was of cubic order. In this equation, the left side characterizes the dynamic behavior of the b_n , the first term on the right side represents the interactions between the considered frequency components, also called the interaction term. In this term we have second and third order elastic constants which cause the nonlinear effects. Clearly, they come from both, the modeled geometrical and material nonlinearities, which generate higher harmonics and combination frequencies. Moreover, the last term of the dynamic equation is the discussed attenuation effects. Note, that the sum in Equation (111) takes all elements of the list n into account which means that for a positive n we could also have negative elements in l or m .

Finally, we can write the time derivative of the displacements which will be later useful to investigate particle velocities. The according equations are

$$\dot{u}_x = v_x = \sum_n v_n e^{-in\omega_a t} u_{xn} e^{ink_a x} \quad (112)$$

$$\dot{u}_z = v_z = \sum_n v_n e^{-in\omega_a t} u_{zn} e^{ink_a x} \quad (113)$$

with v_n defined in Equation (99).

3.1.1.5 Slowly Varying Envelope Approximation Model

A common assumption which is in line with many scientific papers in the considered field is to use the slowly varying envelope approximation (SVEA), meaning that the

amplitudes of the wave change slowly compared to the its oscillation described by its frequency [14–16, 40, 41]. According to [3] if

$$\left| \frac{\partial^2 b_n}{\partial x^2} \right| \ll 2nk_a \left| \frac{\partial b_n}{\partial x} \right| \quad (114)$$

holds, we can neglect the highest order derivative. This gives us the first order ordinary differential equation incorporating the SVEA

$$\frac{\partial b_n}{\partial x} = \frac{in\mu\omega_a}{Mc_r^3} \sum_{n=l+m} lmS_{lm}b_l b_m - \alpha n^2 b_n. \quad (115)$$

We can accordingly approximate the components of the particle velocity v_n as [41]

$$v_n = -i\omega_a n b_n \quad (116)$$

and plug it into Equation (115), which gives

$$\frac{\partial v_n}{\partial x} = -\frac{n^2\mu}{Mc_r^3} \sum_{n=l+m} S_{lm}v_l v_m - \alpha n^2 v_n. \quad (117)$$

This is the same result that Zabolotskaya obtained for the SVEA and one wave, only a different attenuation term has been used here [41]. However, with the presented approach when considering only waves in one direction, there have not been problems with getting a unique formulation of the dynamic equation as the SVEA has been done in the very last step. When implementing the SVEA earlier as in [41] there have been problems with uniqueness for a wave traveling in one direction. As Zabolotskaya first considered waves in both directions this problem did not arise.

Moreover, as we can see from Equation (117), if we choose the initial conditions of v_n to be real, then all v_n 's stay real as the change on the left side equals a real quantity on the right side. In this case $v_n = v_{-n}$ holds and we can reduce the number of involved computations by around fifty percent. This would not be the case for imaginary or complex initial conditions. The choice of real initial conditions does not lose any generality as the initial conditions can be chosen arbitrarily [14].

This model incorporating the SVEA will be important later for the diffraction model in Section 3.3.

3.1.1.6 Discontinuity Distance

A characteristic quantity for wave propagation problems is the discontinuity distance, which will be useful for numerical analyses in the next section. At this distance the waveform of the velocity component will turn into a shock wave with a theoretically infinite slope. The definition for a single bulk wave is [4]

$$x_{d,\text{bulk}} = \left| \frac{2c^2}{\omega\beta_{\text{bulk}}v_{\text{IC,bulk}}} \right|, \quad (118)$$

where c and ω are the wave and angular speed and of the considered wave. The variable $v_{\text{IC,bulk}}$ denotes the initial condition of the particle velocity of the fundamental bulk wave. Additionally, β_{bulk} denotes the acoustic nonlinearity parameter as defined for the considered wave. According to [33] nonlinear Rayleigh waves show similar effects as bulk waves in fluids. Therefore, the idea is to transfer this bulk wave definition to a characteristic quantity for Rayleigh waves. The term for β_{bulk} for Rayleigh waves will be derived later on and is given in Equation 152 as

$$\beta_{\text{true}} = \frac{8i\mu S_{11}}{Mc_r^2 k_a} \quad (119)$$

where S_{11} denotes S_{lm} for $l = m = 1$. Furthermore, we want to write the the initial velocity for a mixed wave. Analogously to [33], we take the initial values of the particle velocities v_n for the fundamentals. With v_{ICa} being the initial condition for v_1 and v_{ICb} for v_ϕ , we obtain $2(v_{\text{ICa}} + v_{\text{ICb}})$ as overall initial particle velocity amplitudes. The factor two comes from the definition of the complex conjugate in the solution form of Section 3.1.1.3. As the discontinuity distance is a real and positive quantity, we can write the final expression for the discontinuity distance for Rayleigh waves with fundamentals having the same initial phase as

$$x_d = \left| \frac{Mc_r^3}{8\mu S_{11}(v_{\text{ICa}} + v_{\text{ICb}})} \right| \quad (120)$$

or on amplitude level

$$x_d = \left| \frac{Mc_r^3}{8\mu S_{11}\omega_a(b_{\text{ICa}} + \phi b_{\text{ICb}})} \right| \quad (121)$$

where Equation 116 has been used with the assumption that the derivatives in x direction of the fundamentals are zero at the beginning. Analogously to the particle velocities, b_{ICa} denotes the initial value of b_1 and b_{ICb} denotes the initial value of b_ϕ

3.1.2 Numerical Simulations

In the following Equation 111 will be used to investigate the behavior of the waveforms and the development of the amplitudes of the different frequency components over the propagation distance for different fundamental frequencies and amplitudes.

3.1.2.1 Waveforms

The NDSolve command of Mathematica 9.0 has been used to numerically solve the differential equations and simulations where conducted on the Partnership for an Advanced Computing Environment (PACE) cluster on a single node with between 32 and 64 cores and 120 to 180 gigabyte memory. The first step in this section will be the verification of the dynamic model and the implemented simulation code. Therefore two initially monochromatic waves are mixed at a frequency mixing ratio of $\phi = 1$ which can be regarded as a single wave interacting with itself and generating higher harmonics. The material properties used are given in Table 3.1 for steel and are the same used in [41] to compare the results easily with the results of Zabolotskaya.

Table 3.1: Elastic parameters of steel.

	Value	Description
E	$2 \cdot 10^{11} \frac{\text{N}}{\text{m}^2}$	Young's modulus
ν	0.27	Poisson's ratio
ρ	$7850 \frac{\text{kg}}{\text{m}^3}$	mass density
A	$-7.6 \cdot 10^{11} \frac{\text{N}}{\text{m}^2}$	Landau's constant
B	$-2.5 \cdot 10^{11} \frac{\text{N}}{\text{m}^2}$	Landau's constant
C	$-9 \cdot 10^{10} \frac{\text{N}}{\text{m}^2}$	Landau's constant

A table for a conversion of the third order elastic constants used by Landau and Lifshitz to other common representations can be found in [4]. As we do not look at a normalized system of equations but rather try to keep the involved terms physically meaningful as for example the representation of attenuation, we need to decide upon a simulation setup. A value of $7.5ie^{-10}$ m has been chosen as initial displacement amplitudes b_{ICa} and b_{ICb} of b_1 and b_ϕ to obtain a real start value in the x -direction for the particle velocity v_x . This helps to easier compare the results to [41]. As no absolute data of experimental Rayleigh wave displacement has been published, the initial values have been chosen of the same dimensions as the fundamentals of longitudinal waves presented in [2]. Moreover, these amplitudes will be similar within the finite element method Chapter 4. Also, we will assume to have no phase shift between the fundamentals for now. The frequency of the fundamentals are 2.5MHz and an attenuation of $\alpha = 6e^{-4}\text{Np/m}$ has been chosen. It is crucial that we set the attenuation to very low values as otherwise the wave would get damped out before effects as shock formations arise. However, a too low attenuation is numerically very difficult to handle. Thus, a good balance needs to be found. The results in Figure 3.3 match the plots presented in [41] for a single Rayleigh wave very well. Here, plot a) shows the vertical velocity component normalized by v_{x_0} which denotes the amplitude of v_x at $x = 0$ when only the two initial waves exist. The propagation distance has been normalized by the discontinuity distance x_d as defined in Section 3.1.1.6. Furthermore, the horizontal axis represents the dimensionless variable $\theta = \omega_a \left(t - \frac{x}{c_r} \right) / 2\pi$, which means that we normalize to full periods of the higher fundamental frequency f_a .

In plot (a) one can observe that the vertical velocity component forms a shock while in plot (b) we can observe a pulse formation with an increasing propagation distance x . The shock wave characteristic is similar to the behavior of liquids like e.g. water waves and we the discontinuity distance x_d gave a good prediction of the distance

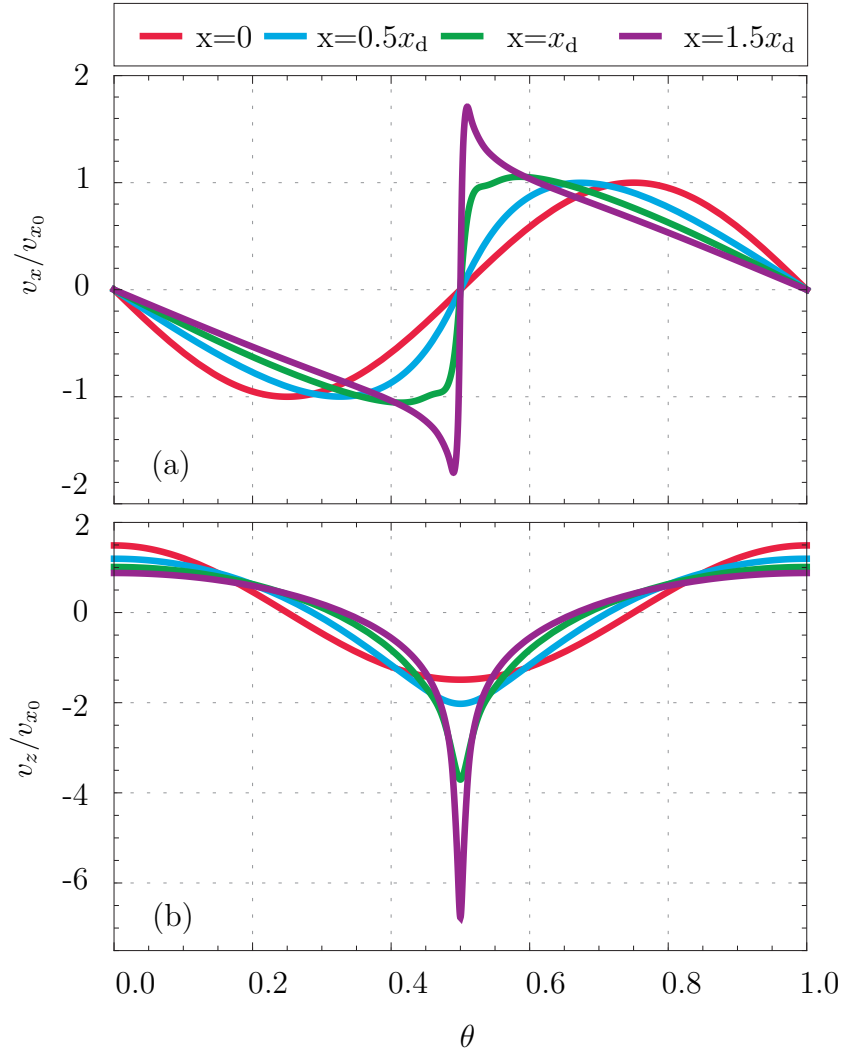


Figure 3.3: Velocity profile of horizontal component (a) and vertical component (b) at $z = 0$ for $f_a=2.5\text{MHz}$, $f_b=2.5\text{MHz}$, $\alpha = 6e^{-4}\text{Np/m}$ and including the first 120 harmonics.

at which the shock formation starts. The peak values of the horizontal and vertical components in plot (a) and (b) become larger before they finally decrease because of attenuation. Consequently, the energy at the surface $z = 0$ increases. However, the total energy of the system cannot grow as it has been modeled as conservative and an attenuation term has later been added. Thus, the energy is only shifted to the surface. The explanation for this phenomenon is that the energy of the fundamental waves is transferred to the higher harmonics while the wave is propagating. And as the penetration depth of higher frequencies is lower according to the u_{xn} and u_{zn} terms, energy conservation demands that the energy needs to be confined more closely to the surface if the damping is not predominant [40, 41].

It should be pointed out that the involved second order differential equations are very costly to solve accurately near the shock formation. Therefore, the SVEA of Section 3.1.1.5 offers a good alternative for long propagation distances to obtain smoother curves in a much smaller time.

Now, in the case of mixing of two waves at different mixing ratios, we also need to include the combination frequencies to around the same level as the level of the harmonics that are necessary for an accurate solution. This means, the simulation of the mixing case becomes even more costly which makes it problematic to obtain a good resolution near the shock in the horizontal velocity component. Hence, it is more efficient to use the SVEA to obtain smooth results at the shock. As it has been shown that the results of the two dimensional model with and without SVEA give very similar results, which supports the assumption of slowly varying amplitudes and shows that both models are in line, we will include the SVEA in the following simulations.

In the next plot shown in Figure 3.4 the mixing ratio is set to $\phi = 0.7$ resulting in $f_a = 2.5\text{MHz}$ and $f_b = 1.75\text{MHz}$. Everything else is kept the same as in Figure 3.3. The number of elements considered reaches up to a level of 120. This means higher

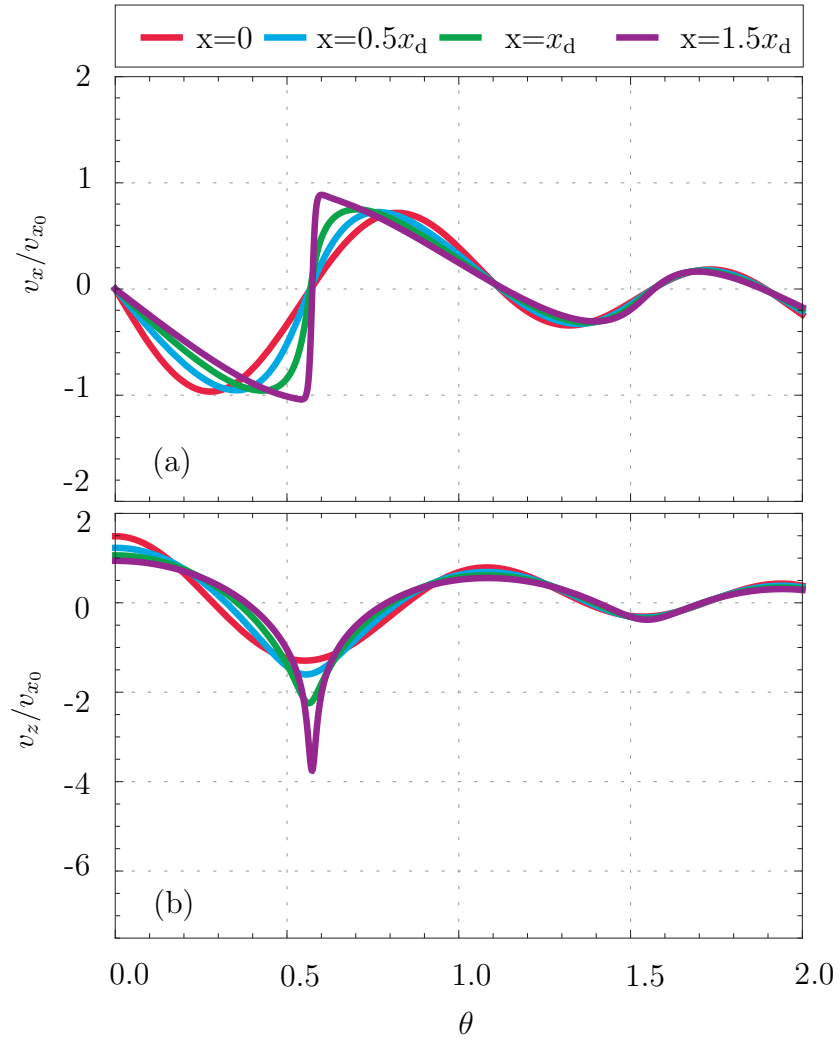


Figure 3.4: Velocity profile of horizontal component (a) and vertical component (b) at $z = 0$ for $f_a=2.5\text{MHz}$, $f_b=1.75\text{MHz}$, $\alpha = 6e^{-4}\text{Np/m}$ and including all frequency components up to a level of 120.

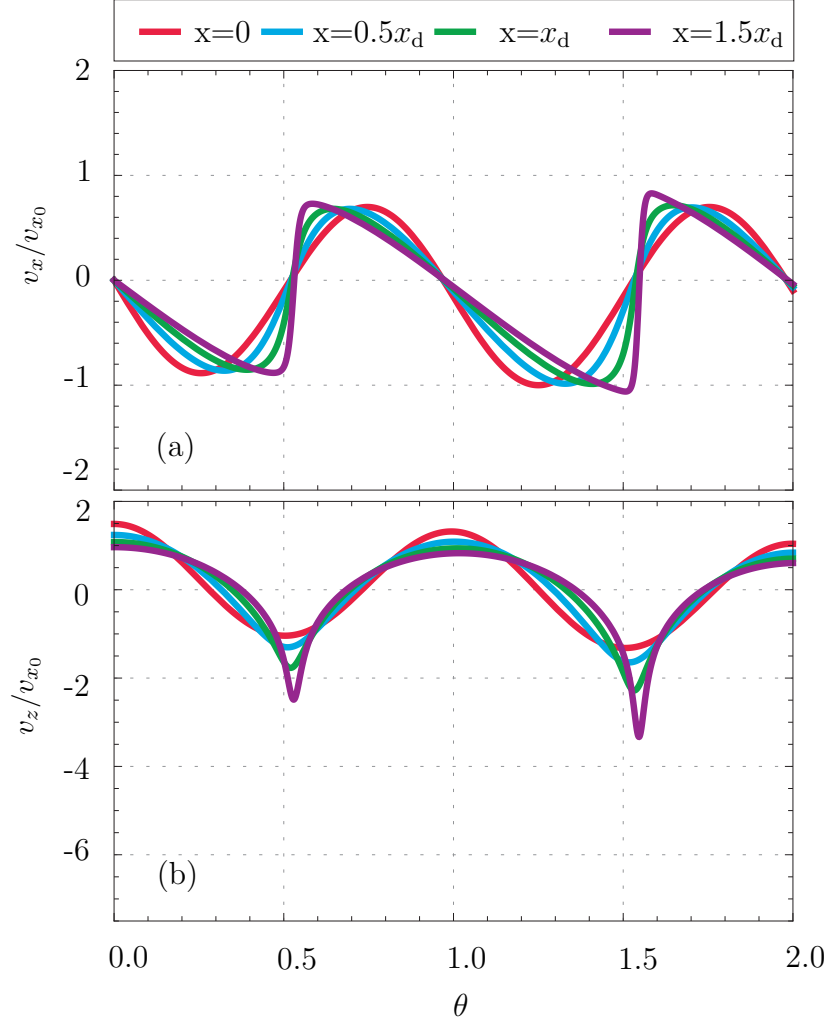


Figure 3.5: Velocity profile of horizontal component (a) and vertical component (b) at $z = 0$ for $f_a=2.5\text{MHz}$, $f_b=0.5\text{MHz}$, $\alpha = 6e^{-4}\text{Np/m}$ and including all frequency components up to a level of 120.

harmonics up 120 times the fundamental frequency and all combination frequencies up to $60 \pm 60\phi$. This ensures that all considered elements are of a similar order of magnitude. We can see that we get a similar result compared to Figure 3.3 as we can also observe a shock and pulse formation in the according velocity plots. A full period where the waveform completely repeats becomes now a lot larger compared to Figure 3.3 since we now have a lower fundamental frequency included.

When we now use the same settings but plot a mixing ratio of $\phi = 0.2$ with $f_a=2.5\text{MHz}$ and $f_b=0.5\text{MHz}$ we obtain the behavior which can be seen in Figure 3.5. Thus,

Table 3.2: Elastic parameters of fused quartz.

	Value	Description
E	$7.17 \cdot 10^{10} \frac{\text{N}}{\text{m}^2}$	Young's modulus
σ	0.17	Poisson's ratio
ρ	$2203 \frac{\text{kg}}{\text{m}^3}$	mass density
A	$-5.28 \cdot 10^{10} \frac{\text{N}}{\text{m}^2}$	Landau's constant
B	$5.4 \cdot 10^{10} \frac{\text{N}}{\text{m}^2}$	Landau's constant
C	$2.148 \cdot 10^{11} \frac{\text{N}}{\text{m}^2}$	Landau's constant

we can see that we can obtain a shock and pulse formation independently of the frequency mixing ratio. Similar investigations with the ratio of the initial amplitudes lead to the same conclusion that the shock and pulse formations are not affected by the specific amplitude mixing ratio. Besides, we can see that the peaks do not become that high when mixing two waves at different frequencies, compared to a single frequency. The less sharp behavior is related to the fact that higher frequencies have a lower penetration depth as mentioned before. As we now got more low frequency terms, especially the combination frequencies that involve differences, the energy in the surface and with that the value of the peak decreases compared to a FMR of one. Nevertheless, it is important to point out that the peaks of Figures 3.4 and 3.5 increase even more for larger propagation distances but will stay smaller than for a single wave.

3.1.2.2 Amplitudes of Frequency Components

Now, we will look at the distinct displacement amplitudes b_n of the level 1 and 2 waves. To be able to evaluate the results, the following simulations are performed for fused quartz according to Table 3.2 to be able to compare them with [14]. The results for three different FMRs are illustrated in Figure 3.6 where the SVEA has been used.

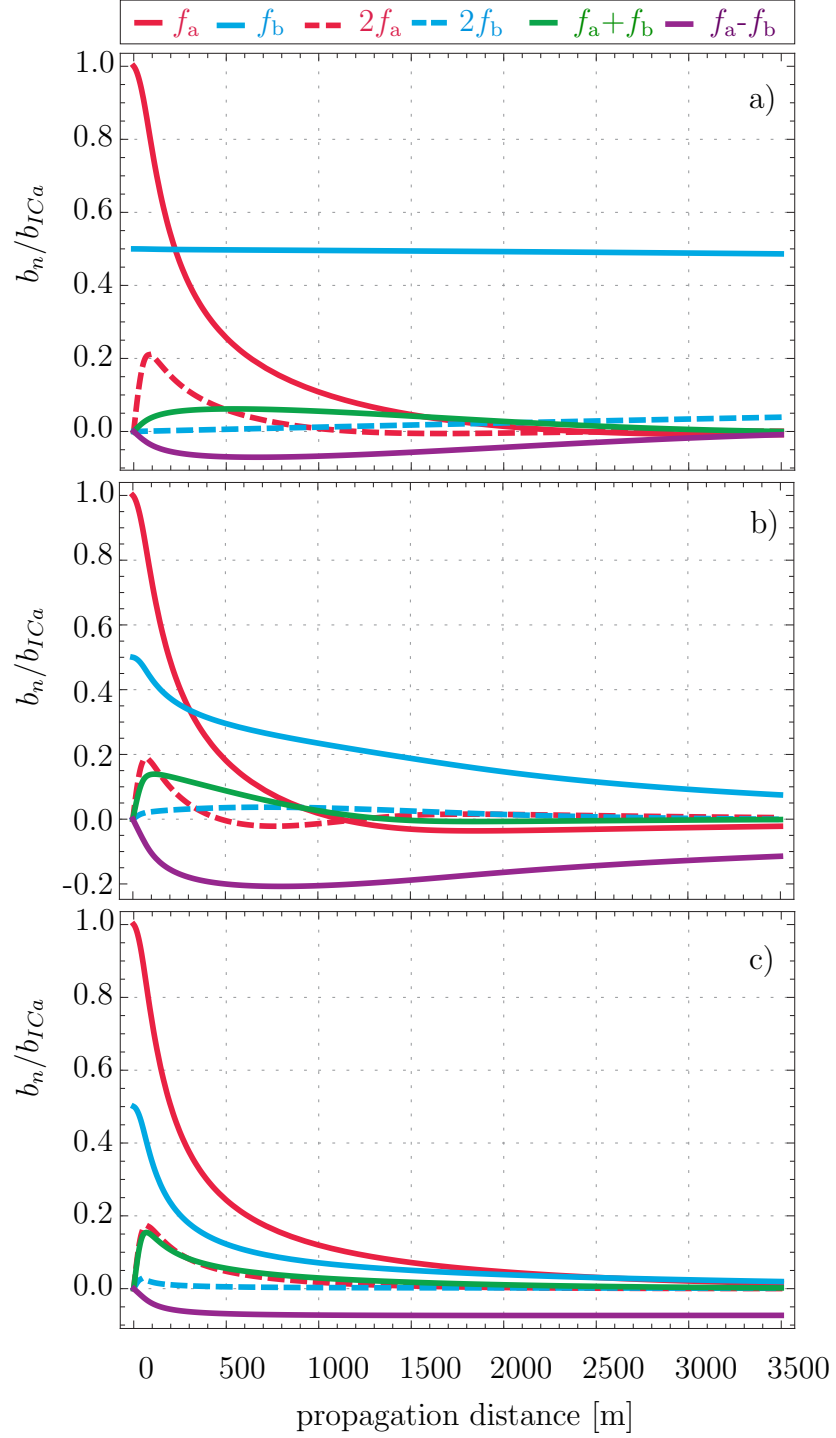


Figure 3.6: Amplitudes of the level 1 and 2 waves normalized to $b_{ICa} = 2b_{ICb} = 7.5e^{-10}$ m over propagation distance. The damping within is $6e^{-4}$ Np/m for fused quartz according to Table 3.2 and the frequency $f_a=2.5$ MHz is fix while f_b is given according to the FMR of a) 0.1, b) 0.6, c) 0.9. All frequency elements up to level 120 are included in the simulations.

Here, the frequency f_a stays fixed at 2.5MHz and f_b varies according to the FMRs of $\phi = 0.1, 0.6$ and 0.9 . The initial condition of wave_b has been chosen as half the value of wave_a which is in line with [14]. However, in contrast to Kalyanasundaram $\phi = 0.5$ has not been chosen as we would have multiple frequencies within the first six wave components. Here are also wave components up to a level of 120 considered instead of only six wave components.

The plots clearly show that the energy transfer is higher for higher frequencies as they oscillate more while propagating the same distance when compared to lower frequencies. This means on the one hand that the damping is higher for higher frequencies, which is obviously the case as the attenuation has been modeled as a function of the square of the specific frequency in Equation (111). But the increased energy transfer for higher frequencies means also that the slope for small propagation distances tends to be larger meaning a steeper rise or fall. These two effects can be observed in the f_b component. For a small FMR it stays approximately constant as the damping is low and the energy transfer to other components as well. For high FMRs the frequency of f_b will be much larger causing higher damping and higher energy transfer to other wave components. This holds analogously for the f_b component. That waves with small frequencies stay relatively constant can also be seen for $\phi = 0.9$ where the difference frequency rises to a certain level which does not change much over the propagation distance. Besides, as the frequencies of f_a and $2f_a$ do not change in the considered simulations, we can see that they stay approximately the same as their energy transfer characteristic stays the same. The fact that the slope at small propagation distances is higher for higher frequencies can also be seen for the sum frequency and the second harmonic of wave_b. As both frequencies increase for higher FMRs, we can see that the slope also rises. However, the most complicated behavior can be found within evolution of the difference frequency component. As this component becomes larger for smaller FMRs one could infer that its slope should be largest for

plot a). This is definitely not the case. The reason is that the difference frequency is mostly generated through the interaction of both fundamentals. However, for small FMRs we have also have a small f_b component, which means that the difference frequency does not get much energy from this fundamental. When the FMR rises, we obtain a larger f_b and therefore a larger slope of the difference frequency until it reaches maximum and drops of again for high FMRs. At these high FMRs f_b is high but the difference frequency itself is low. Thus, the difference frequency component relies on a balance of its own frequency and the frequency of the fundamentals generating it, as both work in different directions. More detailed analyses and ways to optimize the energy transfer towards this component are discussed in Section 3.2.

According to the discussed plots and numerous other simulations, there is a clear trend that the energy oscillates more for lower FMRs. This means that there are more changes in direction and sign switches involved in the evolutions of the different b_n 's of level 1 and 2. An increased initial amplitude b_{ICb} promotes as well more oscillations in the amplitude evolutions.

Furthermore, the negative signs of some b_n can be regarded as a 180° phase shift which would be necessary to conserve the energy in a case of no damping. Note, that the signs of the sum and difference frequencies switch in the case of steel.

The obtained results are partially in line with the results presented in [14]. The behavior of f_b shows also a very constant behavior for small FMRs and changes more for larger ones. Also, the dependence of the slope of the combination frequencies on the FMR and their signs matches pretty well in both models. However, Kalyanasundaram states that for larger FMRs the fundamentals as well as the sum and difference frequency components would reach their minima and maxima faster which is not the case for the difference frequency and the fundamental of wave_a in the presented plots. Also, the f_a component has a differing behavior. These differences could be based on implementation of damping, different material parameters or because of different

modeling approaches which are based on different assumptions.

3.1.3 Justification of Weak Nonlinearity Assumption

One advantage of modeling with the Lagrangian equations is that we automatically have energy conservation incorporated or even attenuation if we choose so. This is not the case as in the classical perturbation method which holds only for finite propagation distances as the correction terms to the primary field must be of smaller dimension than the primary field itself [18]. This would not be the case if we have small attenuation as the higher harmonics could grow as big as the fundamentals. Therefore, the presented approach makes it possible to obtain information about the dynamical behavior for small attenuation and very long propagation distances, which is not possible with the perturbation method. This is confirmed by [19], where it is written that we cannot use the perturbation approach to investigate for example shock formations.

However, to further strengthen the idea that the approach holds for propagation distances even up to where discontinuities appear and higher harmonics can become dominant we have to have a bit closer look at the model and the simulation. One of the main assumptions made was weak nonlinearity, meaning that it is precise enough to model the elastic energy density up the third order to be able to see nonlinear effects. This point can be verified if we calculate the strains

$$\partial_x u_x, \partial_z u_x, \partial_x u_z \text{ and } \partial_z u_z \quad (122)$$

and check if their absolute values stay small in the area of the discontinuity in the particle velocity. Indeed, the strains do not grow much and stay well below unity. The reason is that the displacement field does not develop a discontinuity in opposition to the velocity field [8]. If we would plot a spatial derivative of the particle velocity, it would become very large and theoretically go to infinity for a perfect discontinuity. As a result, the values for the displacement are relatively small and it is safe to say that the nonlinear contributions stay small, which means modeling the energy up to

the third order is accurate enough and the total solution still resembles the form of the linear solution making the model still feasible at the discontinuity.

Note that the small strain basically confirms that also linear equations of motion would be already pretty accurate. However, as we are specifically interested in nonlinear effects this section confirmed that modeling the elastic energy up to the third order gives us already the main part of the nonlinear impact and a good approximation for studying nonlinear effects in an elastic solid.

3.2 Simplified Two Dimensional Model

3.2.1 Modeling

To be able to state some basic characteristics of Rayleigh wave mixing it is desirable to also look at a simplified model. Therefore, we build up on the SVEA model of 3.1.1.5 to get a system of first order ordinary differential equations with reduced complexity. Let us now assume that the generated waves are small compared to the fundamentals and we only look at small propagation distances. Then usually damping can be assumed to be negligible and we obtain the following system of equations

$$\frac{\partial b_n}{\partial x} = \frac{in\mu\omega_a}{Mc_r^3} \sum_{n=l+m} lmS_{lm}b_l b_m. \quad (123)$$

Additionally, for small propagation distances the influence from lower level waves on higher level waves is much higher than the other way around as for example in the interaction term on the right side of Equation (123) b_1b_1 which will influence b_2 will be much larger than b_2b_{-1} which will influence b_1 , as the higher the level the smaller the amplitude for small propagation distances. The reason is, that the energy from the fundamentals will first be transferred to the second level causing small level 2 waves to arise. Then, an interaction of those level 2 waves with the fundamentals will cause level 3 waves to arise which are then of course much smaller than the level two waves as the product of for example b_2b_1 will be much smaller than b_1b_1 . As a result, the trend is that with each step the energy of the fundamentals gets transferred to

a next level where a decrease in amplitude of the according components will happen as they are generated from waves from the levels before. Therefore, we will now assume for small propagation distances that we only have influences from lower to higher levels similar to equations for one wave given in [33, 34]. However, it should be pointed out the the classification in levels does not imply that the levels are generated one after another. It rather gives information about the order of magnitude of the amplitudes of the frequency components, which helps to make consistent decisions about which components should be taken into account. The mentioned assumptions can be denoted as the so-called plane wave assumption where the fundamentals stay unaffected. And we will assume that the influence of the level 3 components on the system is already negligible and therefore we only fundamentals and level 2 components into account. By incorporating these points into Equation (123) we obtain the amplitudes b_1 and b_ϕ of the fundamentals of wave_a and wave_b which are denoted by the according element of the list n as

$$\frac{\partial b_1}{\partial x} = 0 \rightarrow b_1 = \text{constant}, \quad \frac{\partial b_\phi}{\partial x} = 0 \rightarrow b_\phi = \text{constant}. \quad (124)$$

Furthermore, the level 2 waves are given as

$$b_n = \frac{in\mu\omega_a x}{M c_r^3} \sum_{n=l+m} lm S_{lm} b_l b_m. \quad (125)$$

where b_l and b_m are fundamental waves. Consequently, the level 2 waves behave linearly. This model describes Rayleigh waves similarly as solutions for bulk waves via the perturbation method where the fundamental is assumed to be constant and the level 2 waves rise linearly [18]. Nevertheless, it is important to note, that this violates the energy conservation and is therefore only valid for small propagation distances in opposition the complex model as pointed out in Section 3.1.3.

Besides, Equation (125) gives an easy insight into the basic physics of wave generation. The inhomogeneity on the right side can be interpreted as a source term which generates higher harmonics and combination frequencies and one can exactly

Table 3.3: Elastic parameters of 7075-T651 Aluminum.

	Value	Description
E	$7.08729 \cdot 10^{10} \frac{\text{N}}{\text{m}^2}$	Young's modulus
σ	0.337224	Poisson's ratio
ρ	$2700 \frac{\text{kg}}{\text{m}^3}$	mass density
A	$-3.512 \cdot 10^{11} \frac{\text{N}}{\text{m}^2}$	Landau's constant
B	$-1.494 \cdot 10^{11} \frac{\text{N}}{\text{m}^2}$	Landau's constant
C	$-1.028 \cdot 10^{11} \frac{\text{N}}{\text{m}^2}$	Landau's constant

see which fundamentals generate which level 2 waves. So obviously the the combination frequencies are generated of both fundamentals and the second harmonics of the according fundamental wave. This basic relation will be confirmed experimentally in Section 5.2.2.

3.2.2 Simulation

In the following simulations have been undertaken for the level 2 waves modeled according to Equation 125. Aluminum 7075-T651 is used as shown in Table 3.3. This will also be the material used within the experimental Chapter 5.

In Figure 3.7 two different setups are shown. Both initial amplitudes and in plot a) the frequency f_a , in b) the center frequency $(f_a + f_b)/2$ are kept constant. We can see that the second harmonic of wave_b, the sum and the difference frequency component go to zero for small f_b , which is meaningful as the fundamental of wave_b becomes more and more static, which generates less higher harmonics and combination frequencies. In both plots we can see that the difference frequency component needs to be chosen in a certain distance from the boundaries at $\phi = 0$ and $\phi = 1$. The reason is that for a too small ϕ , the fundamental f_b does transfer less energy and for a large ϕ the difference frequency will be small, which means it will rise relatively slowly.

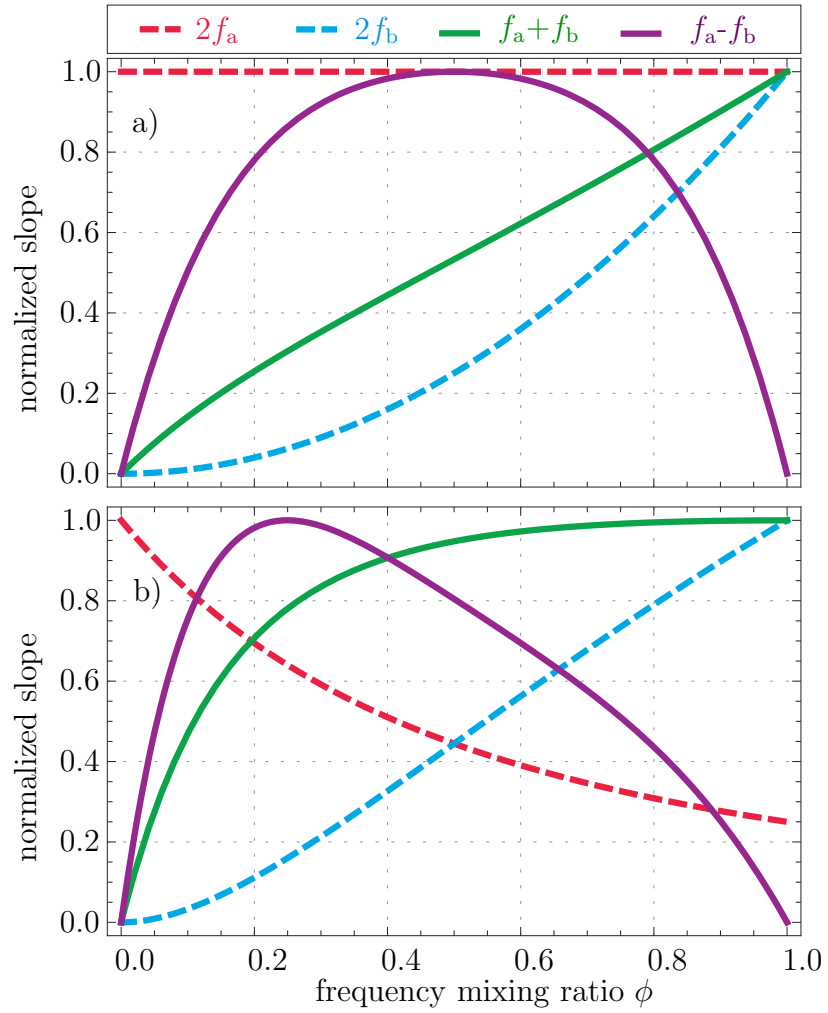


Figure 3.7: Slope over propagation distance for different of the different frequency level 2 components normalized to their maxima and plotted over the frequency mixing ratio. The fundamentals and a) f_a , b) the center frequency $(f_a + f_a)/2$ are kept constant.

All in all, the plots could be used in an experiment to maximize the frequency component of interest.

Besides, the choice of the initial amplitudes is relatively easy as the level 2 waves are either dependent on the product b_1^2 , b_ϕ^2 or $b_1 b_\phi$. Thus, we can easily check how to choose the fundamentals. This relation will be discussed in closer detail in Section 5.2.

3.3 Diffraction Model

Besides the damping effects, the diffraction effects are also important to account in Rayleigh wave experiments, as they are usually conducted in the far field, where those two phenomena play an important role. Therefore it is desirable to obtain a model which takes those effects into account. In the following we will extend the two dimensional model incorporating the SVEA in Section 3.1.1.5 to a third dimension by implementing a finite size source leading to diffraction effects and a similar model as the one wave model stated in [34]. We will still obtain displacements in only two dimensions but with a dependence in the horizontal or y -direction. Using the SVEA assumption will help to simplify the derivation but also the simulation, as a system of partial differential equations will be derived, which can get computationally costly depending on the desired accuracy and the number of frequency components to simulate. Another important underlying assumption is that the diffraction of the Rayleigh waves is small so that we can use a parabolic Taylor series approximation as pointed out in [21, 34]. Let us assume now that the wave vector $n\mathbf{k}_a$ of a Rayleigh wave can be written as

$$n\mathbf{k}_a = n \begin{pmatrix} k_x \\ k_y \\ 0 \end{pmatrix}. \quad (126)$$

Subsequently, we can introduce the small angle Θ_d between the wave propagation direction and the x -axis and write

$$nk_x = nk_a \cos \Theta_d \text{ and } nk_y = nk_a \sin \Theta_d. \quad (127)$$

The wave number now becomes

$$nk_a = n\sqrt{k_a^2(\sin^2 \Theta_d + \cos^2 \Theta_d)} \quad (128)$$

and consequently

$$nk_x = nk_a \sqrt{1 - \sin^2(\Theta_d)}. \quad (129)$$

This can be approximated by a Taylor series approximation around $\Theta_d = 0$ up to quadratic terms as

$$nk_x \approx nk_a \left(1 - \frac{\sin^2(\Theta_d)}{2} \right). \quad (130)$$

Accordingly, we can write the solution forms of Equation (71) now as

$$\begin{aligned} u_x &= \sum_n a_n(t) u_{xn} e^{in(k_x x + k_y y)} \xrightarrow{\text{Taylor}} \\ u_x &= \sum_n a_n(t) u_{xn} e^{ink_a((1-\sin^2(\Theta_d)/2)x + \sin(\Theta_d)y)} = \sum_n \underbrace{b_n e^{ink_a(-\sin^2(\Theta_d)x/2 + \sin(\Theta_d)y)}}_{b_{dn}} u_{xn} e^{in(k_a x - \omega_a t)} \end{aligned} \quad (131)$$

and analogously Equation (72) as

$$u_z = \sum_n a_n(t) u_{zn} e^{ink_a((1-\sin^2(\Theta_d)x/2) + \sin(\Theta_d)y)} = \sum_n \underbrace{b_n e^{ink_a(-\sin^2(\Theta_d)x/2 + \sin(\Theta_d)y)}}_{b_{dn}} u_{zn} e^{in(k_a x - \omega_a t)}, \quad (132)$$

where b_{dn} denotes the displacement amplitudes of the diffracted wave and is a function of x and y . However, for the derivation it is convenient to write the equations on the velocity level where Equations (112) and (113) become

$$v_x = \sum_n \underbrace{v_n e^{ink_a(-\sin^2(\Theta_d)x/2 + \sin(\Theta_d)y)}}_{v_{dn}} u_{xn} e^{in(k_a x - \omega_a t)} \quad (133)$$

$$v_z = \sum_n \underbrace{v_n e^{ink_a(-\sin^2(\Theta_d)x/2 + \sin(\Theta_d)y)}}_{v_{dn}} u_{zn} e^{in(k_a x - \omega_a t)} \quad (134)$$

where v_{dn} denotes the velocity amplitudes of the diffracted wave and is a function of x and y . As a next step, we calculate the partial derivatives

$$\frac{\partial v_{dn}}{\partial x} = -\frac{ik_a}{2} \sin(\Theta_d)^2 v_n e^{ik_a(-\sin(\Theta_d)^2 x/2 + \sin(\Theta_d)y)} + \frac{\partial v_n}{\partial x} e^{ik_a(-\sin(\Theta_d)^2 x/2 + \sin(\Theta_d)y)} \quad (135)$$

and

$$\frac{i}{2nk_a} \frac{\partial^2 v_{dn}}{\partial y^2} = -\frac{ik_a}{2} \sin(\Theta_d)^2 v_n e^{ik_a(-\sin(\Theta_d)^2 x/2 + \sin(\Theta_d)y)}. \quad (136)$$

If we combine Equations (135) and (136), we can write

$$\frac{\partial v_{dn}}{\partial x} + \frac{1}{2ink_a} \frac{\partial^2 v_{dn}}{\partial y^2} = \frac{\partial v_n}{\partial x} e^{ik_a(-\sin(\Theta_d)^2 x/2 + \sin(\Theta_d)y)}, \quad (137)$$

where $\partial v_n/\partial x$ is given by Equation (117) as

$$\frac{\partial v_n}{\partial x} = -\frac{n^2 \mu}{M c_r^3} \sum_{n=l+m} S_{lm} v_l v_m - \alpha n^2 v_n. \quad (138)$$

If we now assume for a moment, that we have real valued initial conditions, then $v_n = v_{-n}$ holds as pointed out in Section 3.1.1.5. Furthermore, as described before, the derivation of the sum in Equation (138) involves a sign switch of n . Let us now switch the sign of n back again and also of l and m in the sum and we get

$$\frac{\partial v_n}{\partial x} = -\frac{n^2 \mu}{M c_r^3} \sum_{n=l+m} S_{lm} v_{-l} v_{-m} - \alpha n^2 v_n. \quad (139)$$

With $v_l = v_{-l}$ and $v_m = v_{-m}$ we can write again

$$\frac{\partial v_n}{\partial x} = -\frac{n^2 \mu}{M c_r^3} \sum_{n=l+m} S_{lm} v_l v_m - \alpha n^2 v_n, \quad (140)$$

which is the same equation as before but now with a changed sign of the n terms within the sum. This means that we do not need to adjust the sign if we pull a term with n into the sum. Note, that the S_{lm} term does not change for sign switches of n or simultaneous sign switches of l and m . Eventually, we can calculate the right

hand term within Equation (137) as

$$\begin{aligned} & \frac{\partial v_n}{\partial x} e^{ink_a(-\sin(\Theta_d)^2 x/2 + \sin(\Theta_d)y)} \\ &= -\frac{n^2 \mu}{Mc_r^3} \sum_{n=l+m} S_{lm} v_l v_m e^{i(l+m)k_a(-\sin(\Theta_d)^2 x/2 + \sin(\Theta_d)y)} - \alpha n^2 v_n e^{ink_a(-\sin(\Theta_d)^2 x/2 + \sin(\Theta_d)y)}, \end{aligned} \quad (141)$$

for $n = l + m$. We can simplify this with the expression of the diffracted velocity amplitude components and plug the result into Equation (137). We obtain

$$\frac{\partial v_{dn}}{\partial x} + \frac{1}{2ink_a} \frac{\partial^2 v_{dn}}{\partial y^2} = -\frac{n^2 \mu}{Mc_r^3} \sum_{n=l+m} S_{lm} v_{dl} v_{dm} - \alpha n^2 v_{dn}, \quad (142)$$

where the initial conditions of the different v_{dn} are arbitrary again as the according initial phase within the exponential terms in v_{d1} and $v_{d\phi}$ is not restricted and can be chosen differently from an angle of zero. This equation is similar to [34]. The main difference is that in this paper only influences from lower harmonics to higher harmonics are modeled except that each harmonic is also influenced by the successive harmonic component. This is not the case in the present model. Finally, let us write this result on the amplitude level by considering the SVEA with the relation

$$v_{dn} = -in\omega_a b_{dn}. \quad (143)$$

The diffraction model can then be written as

$$\frac{\partial b_{dn}}{\partial x} + \frac{1}{2ink_a} \frac{\partial^2 b_{dn}}{\partial y^2} = \frac{in\mu\omega_a}{Mc_r^3} \sum_{n=l+m} lm S_{lm} b_{dl} b_{dm} - \alpha n^2 b_{dn}, \quad (144)$$

where the $\frac{1}{2ink_a} \frac{\partial^2 b_{dn}}{\partial y^2}$ will be denoted as diffraction term. This equation is a system of coupled second order partial differential equations, linear in the second order derivatives. Also note, that the SVEA assumption has only been applied to the second order derivatives in the x -direction which is dominant for wave propagation, but not in the y -direction.

3.4 Simplified Diffraction Model

In order to be able to compare the diffraction model of Section 3.3 to experimental data within the experimental Chapter 5, we need to further simplify the diffraction model. As the aim is to fit the model to experimental data, we need to be able to solve the partial differential equations for different sets of parameters in a fast way. Therefore, we assume that the energy only transfers from lower to higher level frequency components. This leaves us for both fundamentals b_{d1} and $b_{d\phi}$ with

$$\frac{\partial b_{dn}}{\partial x} + \frac{1}{2ink_a} \frac{\partial^2 b_{dn}}{\partial y^2} = -\alpha n^2 b_{dn}. \quad (145)$$

For the level two waves we obtain the usual equation

$$\frac{\partial b_{dn}}{\partial x} + \frac{1}{2ink_a} \frac{\partial^2 b_{dn}}{\partial y^2} = \frac{in\mu\omega_a}{Mc_r^3} \sum_{n=l+m} lmS_{lm} b_{dl} b_{dm} - \alpha n^2 b_{dn}, \quad (146)$$

with source terms on the right side where b_{dl} and b_{dm} denote solely the fundamentals. This system of six equations is similar to the representation in [34]. According to this paper, there exists an analytical solution for the equations of the fundamentals for a Gaussian sources of

$$s_a(y) = b_{ICa} e^{-(y/a_s)^2} \quad (147)$$

$$s_b(y) = b_{ICb} e^{-(y/a_s)^2}. \quad (148)$$

Here, a_s represents a characteristic width of the source and will be taken as the transducer radius in Chapter 5 and the b_{IC} 's are the maximum amplitude of the according fundamental wave. The equation for the fundamentals follows as

$$b_{d1}(x, y) = \frac{b_{ICa} e^{-\alpha_a x}}{\sqrt{1 + ix/x_0}} e^{-(y/a_s)^2 / (1 + ix/x_0)} \quad (149)$$

and

$$b_{d\phi}(x, y) = \frac{b_{ICb} e^{-\alpha_b x}}{\sqrt{1 + ix/\phi x_0}} e^{-(y/a_s)^2 / (1 + ix/\phi x_0)} \quad (150)$$

where $x_0 = k_a a_s^2 / 2$ according to [34] and called the Rayleigh distance of wave_a and α_a and α_b are the damping components of the according fundamental waves.

3.5 Acoustic Nonlinearity Parameter β

3.5.1 Modeling

In Section 2.4.2 the acoustic nonlinearity parameter for P-waves has been derived. However, as Rayleigh waves contain displacements and dependencies in more than one axis direction, we would arrive at more than one nonlinear term similar to [18] where a P- and S-wave have been taken into account together. Thus, we would also arrive at different coefficients yielding different descriptions of nonlinearity. However, as our aim is to quantify the acoustic nonlinearity with one parameter β , we start now in a different way. First of all, it is important to note that in an isotropic solid the nonlinearity parameter β vanishes for transverse waves [29]. Therefore, the idea is now to start with the definition of β for P-waves of Section 2.4.2 which can be written similarly as

$$\beta = \frac{8b_2}{k_a^2 b_1^2 x}. \quad (151)$$

This definition can be found in an analog way in [12] where the only difference is that the displacements have been multiplied by the factor $-i/\eta$ leading to a slightly different definition of b_n . As this factor is assumed to stay constant, both definitions will give the same relative conclusions and therefore we stick to the definition of Equation (151) which is more convenient here.

Besides, this β definition has been derived with a perturbation method. At this, damping was neglected, the fundamental was constant and the second harmonic linear [4, 18]. These characteristics are the same as in the simplified two dimensional model of Section 3.2. Also, for P-waves we were able to derive the true β depending only on material properties directly out of the nonlinear wave equations and state from there the amplitude relation within Equation (151). Now, for Rayleigh waves we could obtain the simplified expressions for the amplitudes depending on material properties but not the expression for β . Thus, the idea is now to start from the other side

and plug the amplitudes of the simplified Rayleigh wave model into the amplitude relations for the β defined for P-waves to obtain an expression for the true β which only depends on material properties. This gives

$$\beta_{\text{true}} = \frac{8b_2}{k_a^2 b_1^2 x} = \frac{8i\mu S_{11}}{M c_r^2 k_a}, \quad (152)$$

where S_{11} denotes S_{lm} for $l = m = 1$. This expression is defined in a similar way in [34] and is independent of the frequency, as the inverse of a wavenumber is contained in M . Note, that this true β is only an analogy to P-waves, but it is usually the value we are looking for in an experiment. It is also important to realize that from the definition of the nonlinearity parameter we obtain the true β by plugging in amplitudes where the assumptions of no damping, constant fundamental and linear second harmonic hold, which is approximately true for small propagation distances. Therefore, if we got absolute experimental data and plug it into Equation (151), the resulting measured β will converge to the true β for small propagation distances. This also means, that if we measure at larger distances where damping and diffraction effects are not negligible anymore, our measured β will be very different from the true β . If we have a good model that takes these effects into account, we can correct for them and approximately back calculate the amplitude or β values for small propagation distances where the true and measured β 's are almost the same [4]. This approach is later conducted in Section 5.2.4.

For now, we only discussed β for one Rayleigh wave. In the case of mixing it is desirable to calculate the exact same β with all level 2 waves, to obtain a high flexibility in choosing the wave component to measure and a good way to compare results. Thus, we need to define β 's for the different level 2 waves and relate them to be able to transfer the values. We can now define a general β formulation as

$$\beta_{lm} = \frac{16 \text{sign}(lm) b_{l+m}}{(l+m) k_{|l|} k_{|m|} b_l b_m x} \quad (153)$$

where l and m are either 1 or ϕ and $k_1 = k_a$ and $k_\phi = k_b$. Also, $\beta_{1,1} = \beta$. Therefore, we have to relate the other β 's to $\beta_{1,1}$. By using the equations of the simplified two dimensional model of Section 3.2, we can state the general relation between the different acoustic nonlinearity parameters of Equation (153) as

$$\beta = \beta_{lm} \frac{S_{11}}{\sum_{n=l+m} S_{lm}} \quad (154)$$

This finally makes it possible to quantify the involved nonlinearity by taking a preferred level 2 wave. Therefore, if we are able to measure absolute displacements and correct for damping and diffraction, we should be able to get approximately the same β by measuring each of the four level two components and the according fundamental wave.

Furthermore, as the S_{lm} term is contained in all β formulations and incorporates material and geometrical nonlinearities, one can infer that the acoustic nonlinearity parameter depends on both nonlinearities [18].

3.5.2 Simulation

In the following we will have a look how the theoretical value of β varies from a case with diffraction and or damping. Simulations were conducted based on Equation (144) for waves with 2.5 and 1.75MHz with maximum initial amplitudes of the fundamentals of $7.5e^{-10}$ m used within Gaussian sources as modeled in Equations (147) and (148) with $a_s = 6.35$ mm which resembles a typical radius of a wedge transducer experimentally used for the considered wavelengths. The elements have been considered up to level 4 only small propagation distances are considered without highly nonlinear effects as shock formations. Furthermore, it is computationally very difficult to take much more components into account as we have a system of coupled partial differential equations that becomes larger for each considered frequency component. The material used is aluminum of Table 3.3 as the diffraction model will later be used to correct for diffraction and damping for experimental data of aluminum. The

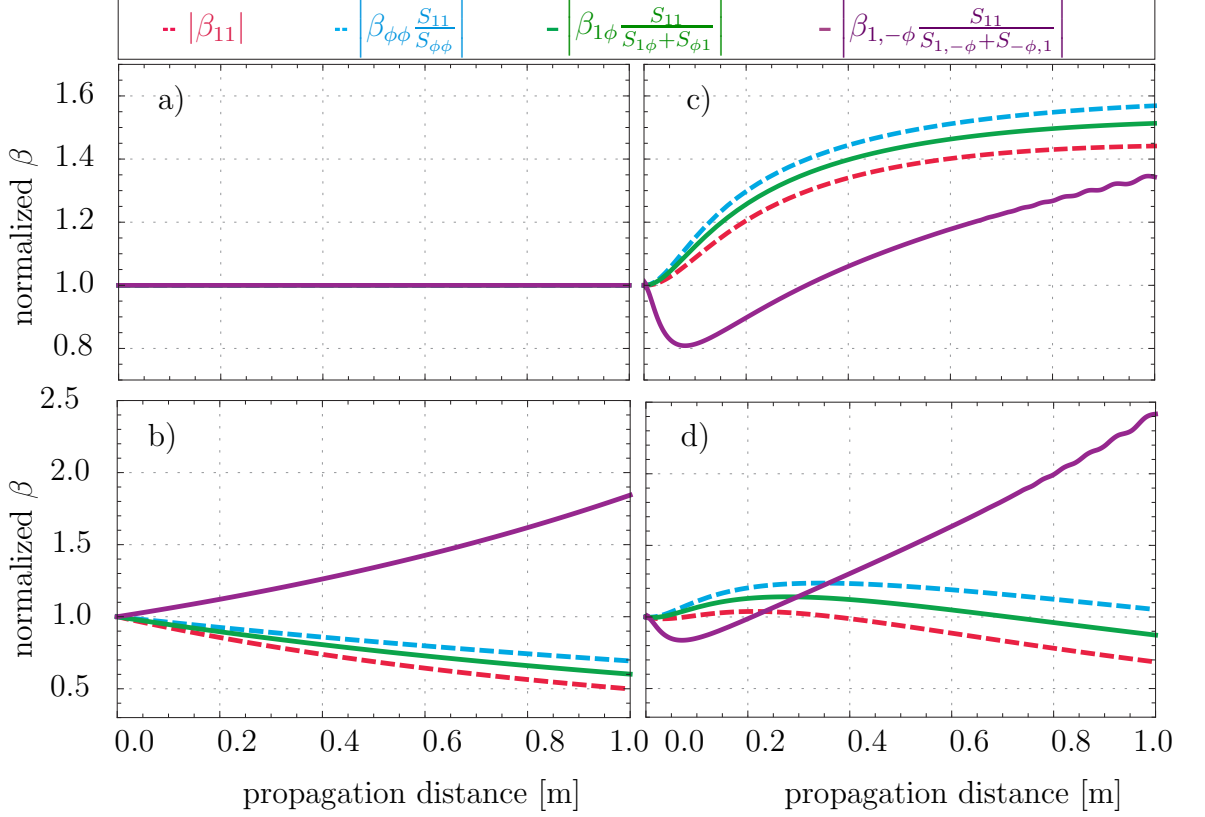


Figure 3.8: Acoustic nonlinearity parameter for aluminum of Table 3.3 calculated on four different ways for a) no diffraction and no attenuation, b) attenuation of 0.8Np/m and no diffraction, c) attenuation of 0.08Np/m and diffraction, d) attenuation of 0.8Np/m and diffraction.

results for four different setups are presented in Figure 3.8. The b_n 's are complex now and differ from the simplified model as damping and diffraction are now taken into account. Therefore, the complex amplitudes in the β formulas will not cancel out. Hence, we need to plot the absolute value of the different β formulations. Now, in plot a) where we have no damping or diffraction we can see that β stays very constant. In plot b) we only have damping. As the damping is higher for higher frequencies, the second harmonics and the sum frequency will fall as they get attenuated faster than the fundamentals. However, as the difference frequency with 0.75MHz is lower than both fundamentals, its β term rises over the propagation distance. In plots c) and d) we finally have both effects, diffraction and damping. As diffraction is higher for lower frequencies, the behavior in the beginning is the other way around now

compared to plot b). In plot d) the used attenuation is 0.8Np/m for 2.5MHz which is based on 0.7Np/m that has been measured for 2.333333MHz.

It is important to note that all curves have been normalized on the value of β_{11} at $x \approx 0$. This means that all expressions are the same in the beginning and Equations (153) and (154) are indeed meaningfully.

All in all, one can conclude that a correction for diffraction and damping is necessary to obtain the true β value at $x = 0$. This is even more important if one wants to compare results of the difference frequency component to another level 2 component, as they vary a lot according to Figure 3.8

CHAPTER IV

FINITE ELEMENT METHOD SIMULATION

In order to validate the analytical mixing model, a finite element model has been set up with the software COMSOL multiphysics version 4.3a and compared to analytical results. The simulations have been conducted on the PACE high performance cluster at the Georgia Institute of Technology. Modules that were used within COMSOL were, besides the base license of COMSOL, the structural mechanics module and the nonlinear structural materials module to incorporate hyperelasticity.

As the finite element method (FEM) is restricted by for example a reasonable domain size and mesh resolution, it is not feasible to compare the FEM model to the analytical model when many high frequency components begin to rise. The reason is that for a doubling of the highest considered frequency the mesh resolution and the detail of the time step size of the solver need to be doubled as well requiring high computational resources. Because of this and as we are experimentally only interested in the level 2 waves as the other components are often extremely small, the FEM model will be used to compare it to the two dimensional model in Section 3.1 for small propagation distances where only the fundamentals and level 2 waves have a reasonable amplitude. Hence, these are the only elements used in the analytical model. Besides, we can scale our time step and mesh size according to the second harmonic of wave_a, which represents higher frequencies not correctly but only involves a small error as they are have negligible amplitudes. For small propagation distances, the influence of damping will also be small. Moreover, as the damping in wave propagation is different for each frequency component it would be difficult to implement such a behavior in COMSOL. As a result, a two dimensional, undamped FEM model has been set up

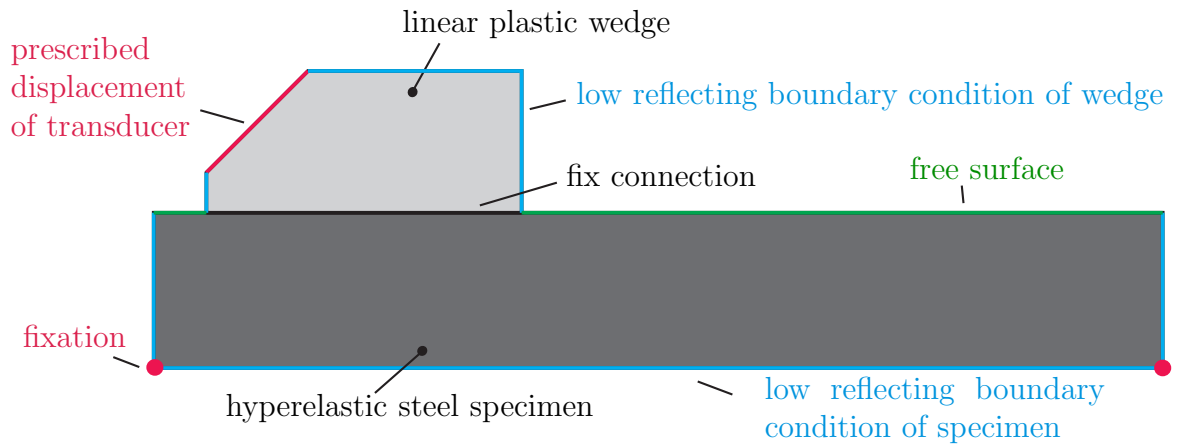


Figure 4.1: Sketch of geometry, material and physics of FEM simulation model.

which resolves waves only up to the larger second harmonic. This should help to make a basic comparison possible and to check if the theory and FEM react the same way on variation of FMRs and AMRs.

4.1 Modeling

In this section the features of the model will be explained. They are important to interpret the simulations later on. A sketch of the model is illustrated in Figure 4.1. This figure will be analyzed throughout the next sections. The model is designed in two dimensions and uses the structural mechanics physics within a time domain analysis. A frequency domain analysis is not applicable as different frequency components in the excitation and measurement are involved and the propagating wave components are nonlinearly coupled.

4.1.1 Geometry

The geometry is kept relatively simple and focuses on two main aspects. Firstly, the generation of Rayleigh waves with the wedge technique. And secondly, wave propagation in a nonlinear material.

Generation using the wedge technique has several advantages. Amongst others, it is

the technique used for experiments and could therefore be a basis for further investigations of the experimental setup instead of only comparing the model to the theory. Also, the wedge technique allows for easy mixing of the waves within the signal of the transducer. This concept would be very difficult to realize with for example the comb technique as one would need to design a comb that is able to excite two waves at the same time or two combs would be necessary which increases the model size. Considering the wedge, it has been designed on the left side with the according Rayleigh wave angle from Section 2.3.6.1. On the right side the focus was to get a large angle in order that waves reflected from the wedge-specimen interface travel a relatively long distance through the wedge before interfering with the generated P-wave.

Furthermore, the wave propagation distance will be counted approximately from the location where the middle point of the P-wave beam that is excited in the wedge hits the specimen. The exact start of the propagation distance is the set by making minor adjustments from the middle point to optimize the fit between FEM and analytical model. This distance is then used for all simulations with the same geometry.

Instead of modeling a complex contact condition between wedge and transducer, they have been modeled as one body with two different materials. This is the ideal and desirable contact condition for Rayleigh wave generation that we seek in experiments by filling up gaps with liquids and firmly attaching the wedge on the specimen as shown in Figure 5.2 in the experimental chapter. Additionally, this reduces the computational effort.

4.1.2 Material

The linear wedge is made of acrylic plastic, which is predefined in the COMSOL material library with a density of 1190kg/m^3 a Young's modulus of $3.2\text{e}9\text{Pa}$ and a Poisson's ratio of 0.35. The hyperelastic specimen has been modeled with the parameters of Table 3.1. This material combination ensures that the P-wave velocity

of the wedge is slower than the Rayleigh wave velocity within the specimen, which is necessary for Rayleigh wave generation. As this chapter serves to qualitatively show the feasibility of the mixing technique an investigation of this material combination was found to be sufficient.

4.1.3 Physics and Boundary Conditions

The most important part of a COMSOL model is typically the so called physics node, where the involved physics or boundary conditions need to be defined. The boundary conditions are painted on color within Figure 4.1. At this, the transducer is simply represented by a prescribed displacement at the left edge of the wedge. This means, that the transducer perfectly connected to the wedge which means that no contacts need to be modeled. This idealization is meaningful, as in the experiment it is necessary to keep the transducer connected to the wedge by for example a fixation as shown in Figure 5.5. For the prescribed displacement two sinusoidal signals with different frequencies are added. Moreover, to ensure that the domains are not floating around, the specimen is fixed in the corners on the bottom.

As the Rayleigh wave is theoretically defined as traveling on a free surface, the upper edges of the specimen have been define accordingly.

A key to meaningful analyses of wave propagation problems defined for infinite components is the handling of reflections. As Rayleigh waves have been derived for an semi-infinite solid, one needs to reproduce this fact as precise as possible. COMSOL offers three different possibilities. Infinite domains, perfectly matched layers and low-reflecting boundary conditions. However, the first two are not applicable in time domain analysis as conducted here. Therefore, low-reflecting boundary conditions have been used. These ensure that only a small part of an incident wave gets reflected back and they work better the closer the incident wave direction is to the normal direction of the considered boundary. Low reflecting boundary conditions

have been used within the wedge and the specimen. However, tests showed that a significant percentage of the Rayleigh wave propagating close to the surface, has been reflected back at the right boundary within Figure 4.1 even when the low reflecting boundary has been optimized for Rayleigh waves. Therefore, the low reflecting boundary condition in the specimen has not been used to handle Rayleigh wave reflection but to further decrease the influence of reflected P- and S-waves. These waves are small compared to the Rayleigh wave, but travel faster and can influence the small nonlinear effects before the Rayleigh wave reaches the boundary. The low reflecting boundary conditions is consequently to create an impedance match for P- and S-waves to reduce reflections. To handle Rayleigh wave reflections, there was no other option than making the domain large enough to avoid reflections in the considered simulation time.

4.1.4 Nonlinearity

As already mentioned, the wedge has been modeled as a linear material as we are not interested in nonlinear effects within this component. To model nonlinear effects within the specimen, the nonlinear structural materials model has been used. Here, hyperelasticity based on the formulation of Murnaghan is predefined, which uses the strain invariants. This expression is also accurate to the third order and equivalent to Equation 55. Additionally, it is based on the Lagrangian strain with geometrical nonlinearities. However, in the theory strain terms of order four and higher have been neglected after the Lagrangian strain has been plugged into the elastic energy density. This is not the case in COMSOL. Additionally, there is no easy possibility for modification available. But according to Section 3.1.3, the fourth order terms should be much smaller than the already small third order terms. Therefore, this difference in approximation will have a neglig As the nonlinear effects we are interested in are very small, we need a certain propagation distance to obtain a measurable

amplitude which can be well separated from other effects within the DFT. But as long propagation distances are computationally expensive and as the aim is to only compare both models but not any special values, it has proven to be useful to increase the nonlinearity by a certain amount. As the geometric nonlinearities are not easily accessible in COMSOL, the idea is now to simply increase the material nonlinearity i.e. all third order elastic constants within COMSOL and the analytical model. It is now important to scale those factors in a meaningful way. If we scale to small, we will still have problems to get good results from the DFT. And if we scale to high, wave components higher than level 2 will obtain a not negligible amplitude and we would need to make the mesh and time steps of the solver finer to resolve these components and their influence on the other components correctly. By using the analytical model it has been found that a factor of 150 is useful for a propagation distance of about 20mm. This factor will be used for the simulations later on.

4.1.5 Mesh

According to the documentation on the COMSOL website it is recommended to choose a mesh size that is around five times smaller than the smallest considered wavelength. As we only look at level 1 and 2 waves, the component of interest will be $2f_a$. As f_a will be fixed in this chapter to 2.5MHz, we obtain the mesh size of the specimen as

$$meshsize_s = \frac{\lambda_s}{5} = \frac{c_r}{10f_a} = 116.88\mu m, \quad (155)$$

where the Rayleigh wave velocity of the steel of Table 3.1 is given as $c_r = 2922.15\frac{m}{s}$. Therefore, the maximum mesh size within the specimen has been rounded to $120\mu m$. For the wedge one needs to take the P-wave velocity of acrylic plastic which is $c_{pw} = 2077.45$ and the highest frequency, which is only f_a , as the wedge is linear. This leads

to the wedge mesh size

$$meshsize_w = \frac{\lambda_w}{5} = \frac{c_{pw}}{5f_a} = 166.2\mu m. \quad (156)$$

A slightly smaller maximum mesh size of $160\mu m$ has been taken here. Furthermore, the specimen has been divided into two parts, where for the lower part a mesh size of maximum $170\mu m$ has been taken, as the high frequencies decrease faster with depth than the lower frequencies within a Rayleigh wave and as we are not interested in resolving the wave nicely on the bottom of the specimen. The standard model used for most simulations solves for around 200000 degrees of freedom.

4.1.6 Time stepping

Besides resolving the largest second harmonic in space, we also need to resolve it accurately in time. According to COMSOL a CFL (CourantFriedrichsLewy) number of 0.2 is close to optimal, which yields

$$timestep = \frac{0.2}{10f_a} = 8ns. \quad (157)$$

To be on the save side and obtain a reasonable DFT resolution a maximum time step of 6.5ns has been chosen.

4.1.7 Solver

COMSOL offers several direct and iterative solvers. The direct solver called Spooles worked very memory efficient but slowly. It is often a useful choice on a machine with small memory. However, on the PACE cluster where multi core calculations where used, the Pardiso direct solver has been taken, as it usually scales up best. Tests with indirect solvers gave very similar results. Note, that the solvers utilized here used the fully coupled attribute feature which uses a damped version of Newtons method.

4.2 Simulation

4.2.1 Computing

The simulations presented in the following have been conducted on the PACE cluster at the Georgia Institute of Technology. Batch jobs had to be submitted as the interactive mode of COMSOL has been relatively unstable on the cluster. Because of the speed up difficulties mentioned in Section 4.1.7 several simulations with different parameter sets have been calculated on a single node. The two dimensional simulations were conducted with 2-4 cores and 10-16 gigabyte memory, as the amount of memory was the main problem. The simulation time varied between 10 and 40 hours depending on the details and sizes used in the different setups. The use of more resources did not result in a useful speedup. Thus, the resources have rather been used to start several simulations at the same time.

4.2.2 Signal Processing

Within the simulation only data at discrete points is saved, as a fine resolution in time is needed for tracking nonlinear effects and conducting a discrete Fourier transform (DFT). Saving data on all mesh points would result in huge models which need a lot of memory to access and analyze and a lot of space on the hard disk. Therefore, 32 probe points are fixed on the free surface of the geometry at distances of 0.5mm between each other. These probe points measure the vertical displacement in material coordinates in the z direction, which is defined in Figure 2.5. This makes it possible to compare the results with the z component of the theory. The same procedure also works for displacements in the x direction.

When a simulation runs, the 32 probe points will now record the displacement in the vertical direction over time, which yields time domain signal similar to Figure 4.2. Here, the steady-state region for the Hanning window can be chosen already after the first few oscillations as the signal is relatively clean. As a next step, the time signal

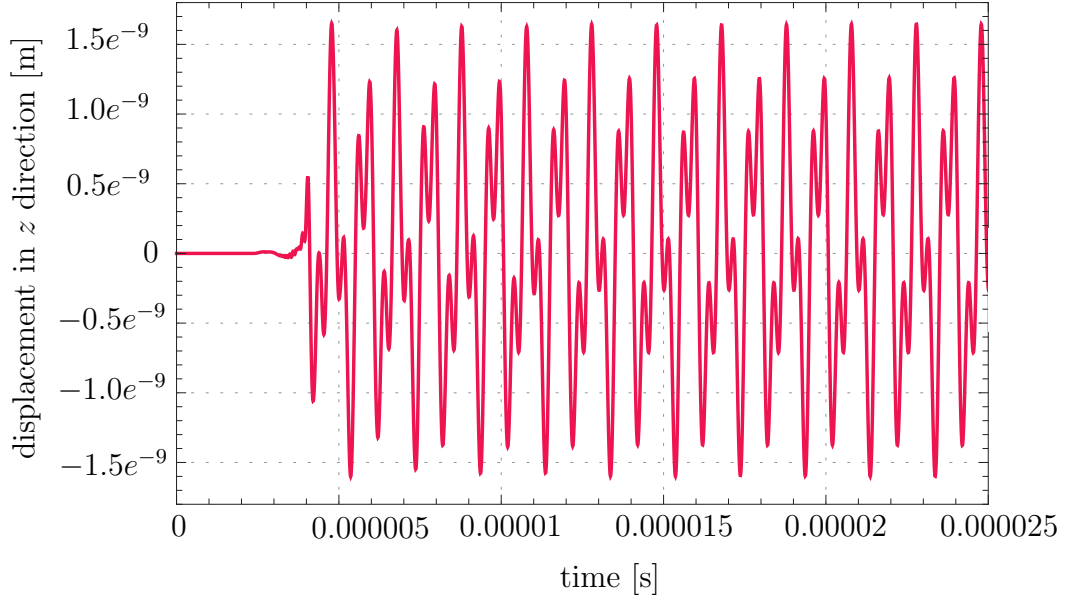


Figure 4.2: Time domain signal in z -direction for mixing of 2.5 and 1MHz waves with an AMR of 1.5 at 5.5mm propagation distance in steel with increased nonlinearity by a factor of 150.

is transformed into the frequency domain with a DFT resulting in a plot like Figure 4.3. . At this, the original DFT amplitudes have been back calculated to the time domain signal with the approximate formula

$$time\ domain\ amplitude = \frac{4\ frequency\ domain\ amplitude}{number\ of\ data\ points\ used\ for\ Hanning\ window}. \quad (158)$$

Selecting approximately full periods for the Hanning window was found to be very important to obtain good DFT data. This helps to get a more periodic signal to reduce side lobes in the DFT plot compared to a rectangular window.

After the DFT is performed, the maxima at the level 1 and 2 frequencies can be calculated. This process is repeated for 32 different propagation distances. The fundamentals of the analytical model are then fitted to the FEM results with a single constant factor. The whole signal processing procedure is summarized in Figure 4.4. Note that in Figure 5.8 there are relatively few cycles taken to improve visibility. In a simulation more steady-state cycles as for example in 4.2 have to be simulated to obtain a better DFT.

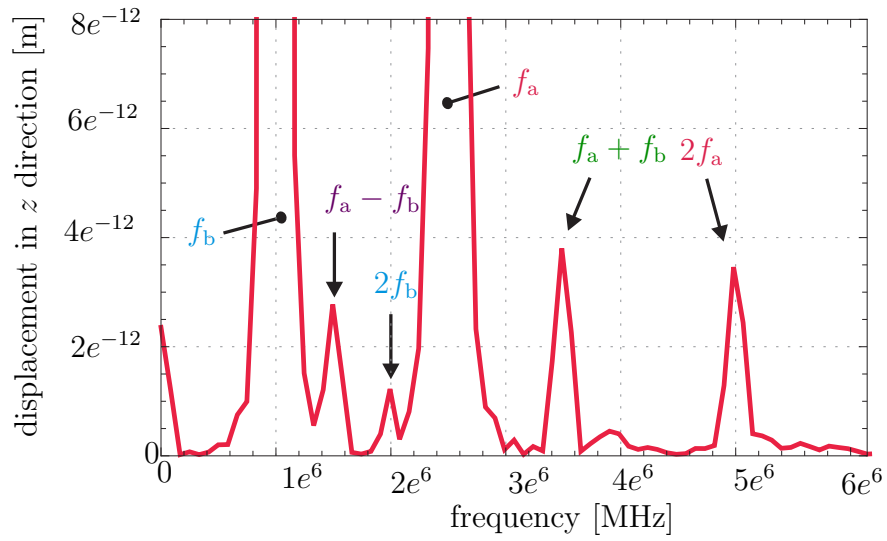


Figure 4.3: DFT plot of time domain signal of Figure 4.2 with a Hanning window applied and approximately back calculated to time domain amplitudes with Equation (158).

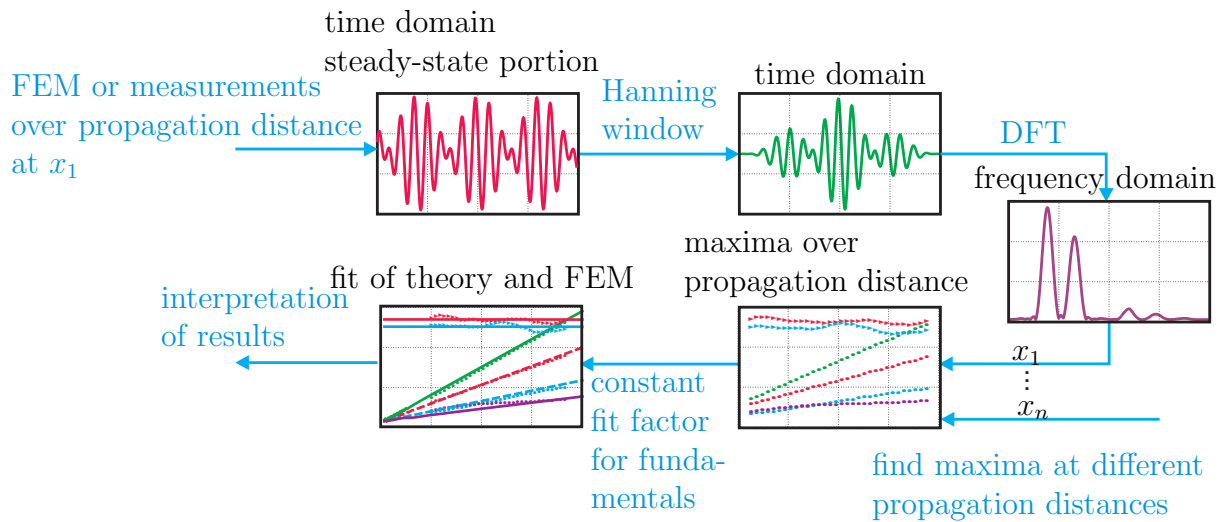


Figure 4.4: Workflow in processing of the time domain signal obtained within FEM.

4.2.3 Results for Different Frequencies and Amplitudes

As the FEM model has a different excitation method compared to the theory where a perfect Rayleigh wave is given as initial condition and as we have information losses through signal processing in the DFT, through finite domains and finite resolutions in space and time, meaning limited mesh and time step resolutions, we can expect that we will obtain several differences between both models for which all these aspects are responsible.

Now, we compare the two dimensional model of Section 3.1 to the FEM model for a sine wave with amplitude of $15e^{-10}$ for each wave, which are added up in the transducer to excite a mixed P-wave. A frequency for wave_a of $f_a = 2.5\text{MHz}$ has been applied and a frequency of 1 and 2MHz for wave_b as shown in Figure 4.5. The scale on the left side holds for the fundamentals, the scale on the right side for the level 2 waves. It can be observed, that the models match relatively well for the different FMRs and AMRs and the considered propagation distances. Here, the amplitude of the f_b component within the Rayleigh wave tended to decrease for a lower f_b despite the amplitudes in the excitation of the transducer stay constant. This effect is most likely related to the fact that the energy for a higher frequency will be more confined near the surface as pointed out in 3.1.2. This will cause a higher amplitude for higher frequencies as the displacement has been measured on the free surface. Considering plot b) of Figure 4.5, we can see that the difference frequency component is relatively inaccurate compared to plot a). The reason is that in plot b) it has a value of only 0.5MHz compared to 1.5MHz in plot a). This means that the wavelength will be three times larger in plot b) leading to a much smaller decrease in energy. Therefore, much more reflections of the difference frequency component will occur within the specimen leading to a distortion of this component. A more detailed discussion on these effects will follow in the Specimen Size Section 4.2.4. In Figure 4.6 surface plots of the Rayleigh waves are presented for the setups used in Figure 4.5. The

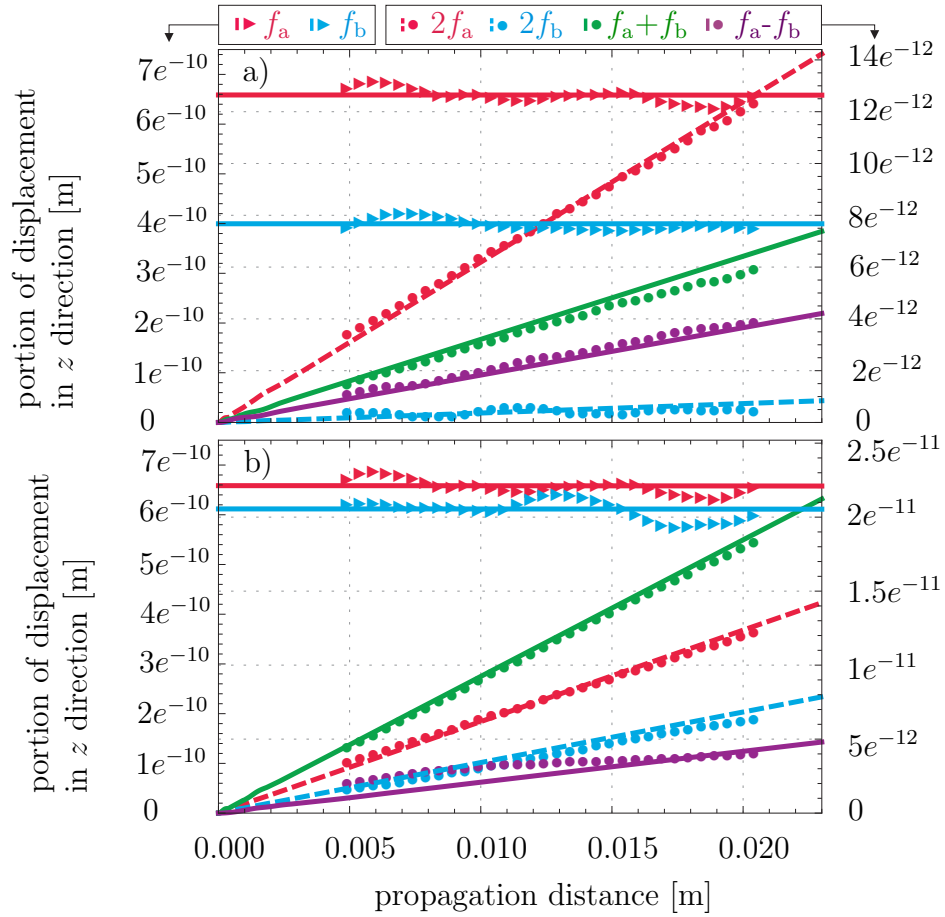


Figure 4.5: Comparison of vertical displacement portions of the different frequency components of the two dimensional model (curves) with the FEM model (markers) for $f_a = 2.5\text{MHz}$ and a) $f_b = 1\text{MHz}$ and b) $f_b = 2\text{MHz}$. The maximum P-wave excitation is $15e^{-10}\text{m}$ for both fundamentals. Material nonlinearity within steel is increased by a factor of 150.

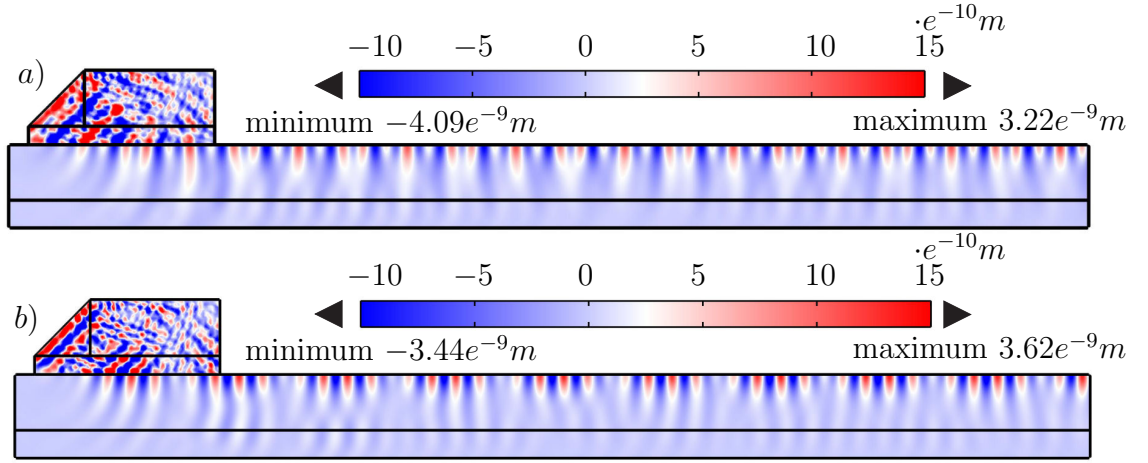


Figure 4.6: Surface plot of vertical displacement for the FEM model for $f_a = 2.5\text{MHz}$ and a) $f_b = 1\text{MHz}$, b) $f_b = 2\text{MHz}$. The used setups are the same as used in Figure 4.5.

evanescent behavior of the Rayleigh wave can be observed and the different form of the wave displacement depending on the FMR. The color range has been adjusted in order that the displacements in the specimen is easier recognizable. Therefore, the color gradient does not cover the whole displacement range. In the following sections parameter variations will be conducted based on the setup of Figure 4.5 plot b) to point out important effects on the simulation results that were all considered to optimize the results.

4.2.4 Variation of Specimen Size

As already mentioned in Section 4.2.3 we obtain reflections for larger wavelengths within the specimen, when its depth is not large enough. The specimen depth used for the plots in Figure 4.5 was 4.5mm. The wavelength of the difference frequency component for a setup with $f_a=2.5\text{MHz}$ and $f_b=2\text{MHz}$ gives a wavelength of

$$\lambda_w = \frac{2922\text{m/s}}{0.5\text{MHz}}\text{m} = 5.844\text{mm}. \quad (159)$$

Hence, the geometry does not even allow one wavelength of the difference frequency component. This large wavelength is the reason why this component was least accurate in Figure 4.5 b). However, the use of low reflecting boundary conditions improves

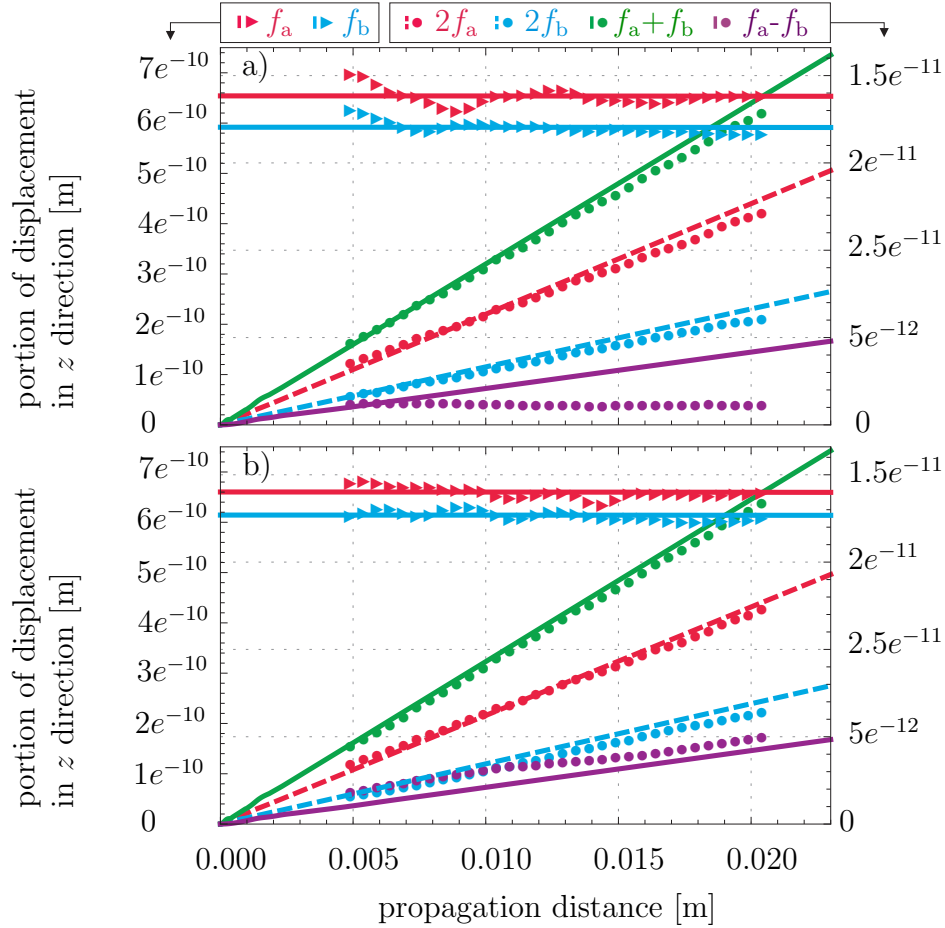


Figure 4.7: Comparison of vertical displacement portions of the different frequency components of the two dimensional model (curves) with the FEM model (markers) for $f_a = 2.5\text{MHz}$ and $f_b = 2\text{MHz}$. The maximum P-wave excitation is $15e^{-10}\text{m}$ for both fundamentals. Material nonlinearity within steel is increased by a factor of 150. The specimen depth is a) 0.5 and b) 2 times the depth used in Figure 4.5 plot b).

the situation a lot. The effect of variation of the specimen depths, two simulations with same the parameters as in the setup of 4.5 b) but different depths can be seen in Figure 4.7. Clearly, the difference frequency component is affected a lot by variation of the specimen depth. This depth needs to be chosen depending on the involved frequencies to obtain accurate results. A larger depth also reduces the oscillations of the fundamentals to a certain extent as effects of reflections become smaller.

When the specimen depth is chosen too small, we obtain very large effects on the fundamentals. This can be seen more clearly when simulation with low FMRs like

0.1 or 0.2.

4.2.5 Variation of Wedge Size

In this section the wedge size is now be varied based on the setup of Figure 4.5 b). The according results for half and double the original wedge size is presented in Figure 4.7 Here, different propagation distances are used as the probes where placed right after the wedge for measurement of vertical displacement. According to the plots, the oscillations of the fundamentals are less severe for a larger wedge, at least relatively to the amplitudes of the fundamentals. This effect is most likely due to reduced reflections within the wedge. An increased wedge size causes the waves to travel longer and reduces the reflection problems to a certain degree.

4.2.6 Variation of Nonlinearity

As a next step the influence of the factor multiplied to the third order elastic constants after Murnaghan is investigated, which will be called nonlinearity factor in the following. Based on the setup of Figure 4.5 b) with a nonlinearity factor of 150, simulations with a nonlinearity factor of 10 and 1350 are shown in Figure 4.9. In plot a) the fundamentals are resolved as usual. However, the level 2 waves are still so small that we can hardly calculate useful values within the DFT. In plot b), we can see the other extrema. The level 2 components became so high that the fundamentals show a clearly visible decrease as they transfer their energy to the level 2 waves. Along with that, level 3 waves begin to have a significant influence on the overall result. This can be seen in the decrease of the level 2 after a certain propagation distance. However, as the mesh and time steps were not designed for measuring level 3 components, the amplitudes become relatively inaccurate. Therefore, a comparison to the analytical model with level 3 components did not give good results.

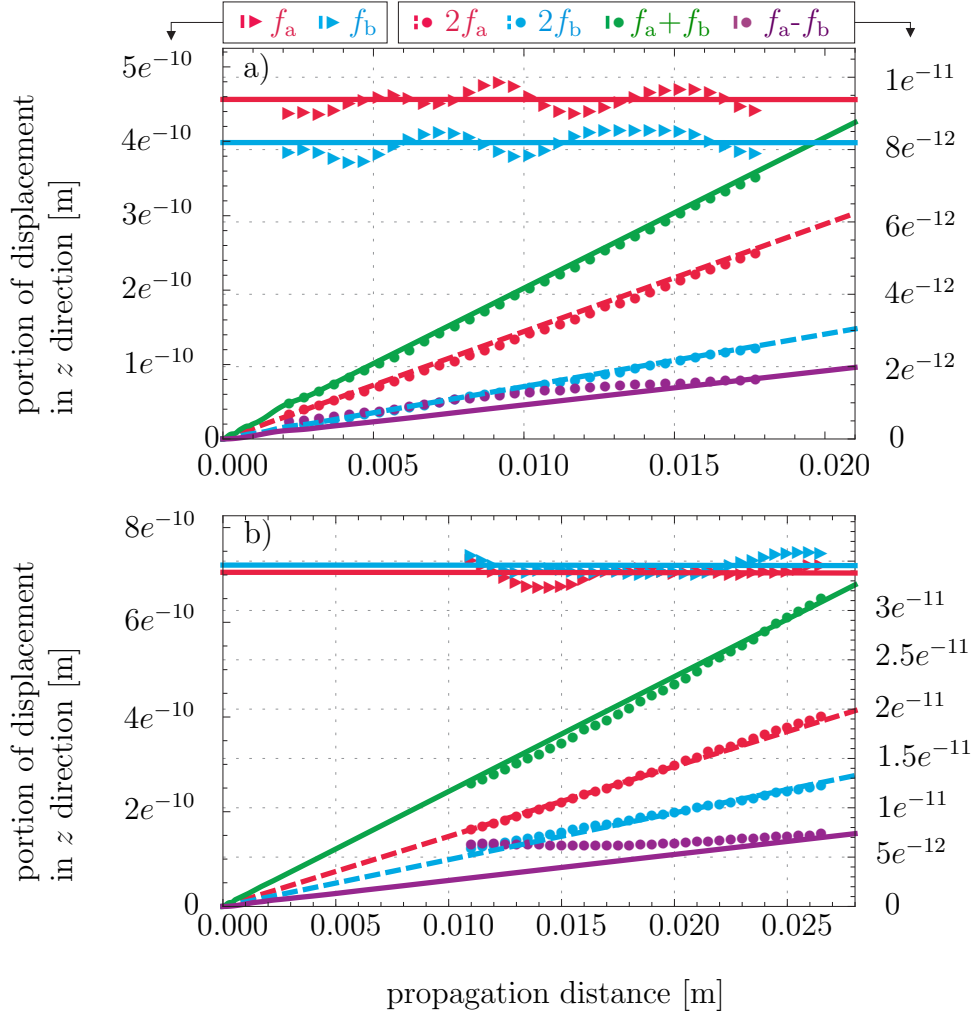


Figure 4.8: Comparison of vertical displacement portions of the different frequency components of the two dimensional model (curves) with the FEM model (markers) for $f_a = 2.5\text{MHz}$, $f_b = 2\text{MHz}$ and a maximum P-wave excitation of $15e^{-10}\text{m}$ for both fundamentals. Material nonlinearity within steel is increased by a factor of 150 and the wedge size is multiplied by a factor of a) 0.5 and b) 2 compared to the setup used in Figure 4.5 b).

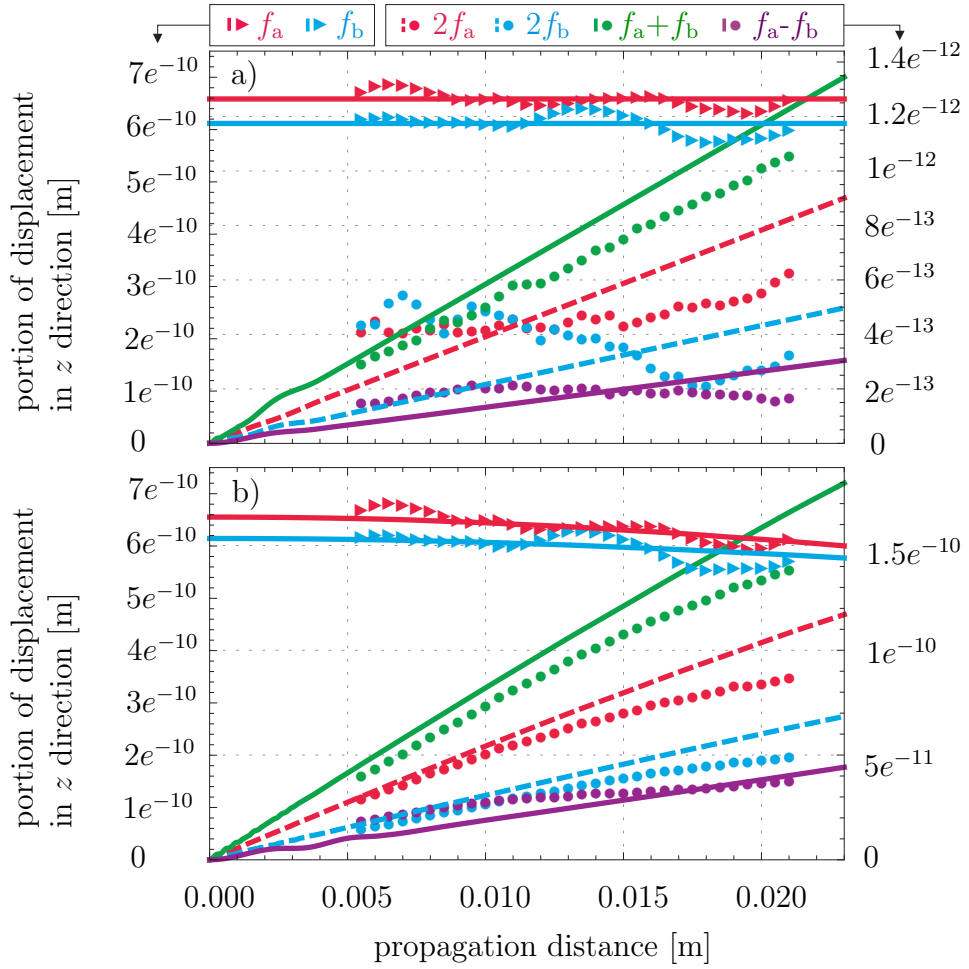


Figure 4.9: Comparison of vertical displacement portions of the different frequency components of the two dimensional model (curves) with the FEM model (markers) for $f_a = 2.5\text{MHz}$, $f_b = 2\text{MHz}$ and P-wave excitation of $15e^{-10}\text{m}$ for both fundamentals. Material nonlinearity within steel is increased by a factor of a)10, b)1350. Otherwise the setups are identical as used in Figure 4.5b)

4.2.7 Variation of Mesh Size

The effect of an inappropriate mesh size is pretty obvious. As the mesh size needs to be designed according to the highest considered frequency, this component will also be the first one to suffer from a not detailed enough spatial discretization. Tests have shown that the fundamentals are relatively unaffected when the mesh size has been doubled within the specimen. This is in contrast to the high level 2 frequency components which rise relatively normal in the beginning but after a certain propagation distance they start to decrease rapidly.

Besides, a more detailed mesh for the setup of Figure 4.5 did not result in any visible improvements. This confirms that the mesh has been dimensioned accurate enough.

4.2.8 Variation of Time Step

Variations of the time step within the solver gave very similar results to the variation of the mesh size. A too large time step caused the high frequencies to become inaccurate first. Investigations also showed that the time step used for the setup of Figure 4.5 was accurate enough as smaller time steps did not result in improvements.

4.3 FEM Conclusion

This FEM section showed qualitatively and quantitatively that the analytical model of Chapter 3 and the FEM simulation model match well for the considered setup. A variety of influences on the FEM model have been shown. They were all taken into account to design the model in a way that it works accurately but also fast enough to show the feasibility of the analytical model. Much more detailed models have not been investigated as no big improvements have been observed for variation of different parameters. However, it is expected that the results are becoming slightly better but the computationally effort would most likely become relatively large to further approximate the analytical model of a semi-infinite solid.

CHAPTER V

EXPERIMENTAL VALIDATION

In the following chapter the mixing technique of two collinear Rayleigh waves will be performed experimentally. The objective is first to generally show that we can measure the generated level 2 waves and use them to characterize the acoustic non-linearity parameter β with the applied technique. After showing the feasibility of the technique, several measurements are performed for different frequencies and amplitudes of the two mixing waves in order to confirm basic relations modeled within the derived dynamic equations of Chapter 3. As a last next step, a comparison between experimental results and the diffraction model of Section 3.3 is conducted to test if they are qualitatively in line.

5.1 Experimental Setup

5.1.1 Experimental Procedure

The basic concept of the conducted experiment can be seen in Figure 5.1. Here, two function generators produce sine waves at two different frequencies. As a next step, we mix the two waves in the electrical signal and feed the obtained wave into a gated high power amplifier. The amplified signal is sent from there to a transducer mounted on a wedge similar to Section 2.3.6.1. Then, a mixed P-wave will be excited which causes a mixed Rayleigh wave to propagate through the surface of the nonlinear material. This generates in all kinds of higher harmonics and combination frequencies of which usually the level 1 and level 2 waves can be measured. For detection, an air-coupled transducer is used which sends the measured data to a receiver which amplifies the results to obtain a large enough amplitudes. The measurements are displayed and processed with an oscilloscope and serve later as input to software like

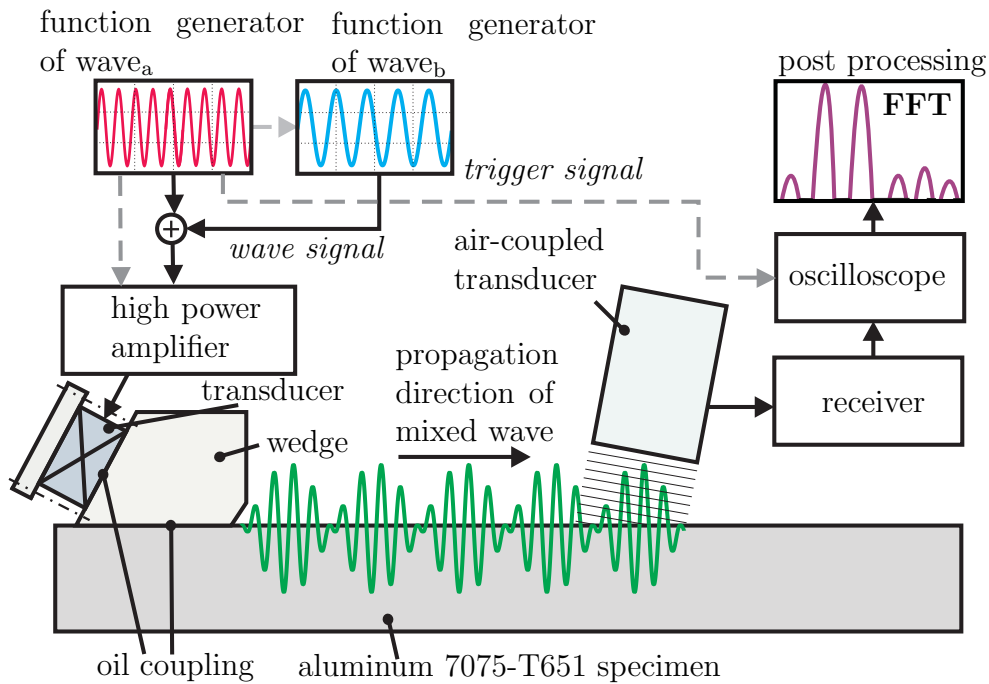


Figure 5.1: Concept of experimental Rayleigh wave mixing.

Matlab for post processing and signal processing respectively, similarly to Figure 4.4. The heart of the setup, which is the transducer installation on the specimen is illustrated in Figures 5.2 and 5.3, where the propagation direction is from right to left now. Here, it is important to fix the plastic wedge firmly to the specimen to obtain clean contact conditions that are necessary for making good measurements. Also, the wedge transducer and the air-coupled transducer have to be aligned to measure as close as possible on the center of the propagating Rayleigh wave beam to obtain a large signal. The black device within 5.3 serves to adjust the propagation distance of the air-coupled transducer, to measure the development of the level 1 and 2 components over distance. This device can be used to adjust the distance by fractions of a millimeter which is very useful for accurate measurements as a millimeter was the used step size in all conducted experiments in this research.

5.1.2 Experimental Devices

Several technical devices and parts as shown in Figure 5.1 were necessary to conduct the experiments. Some important facts will be explained in the following that give

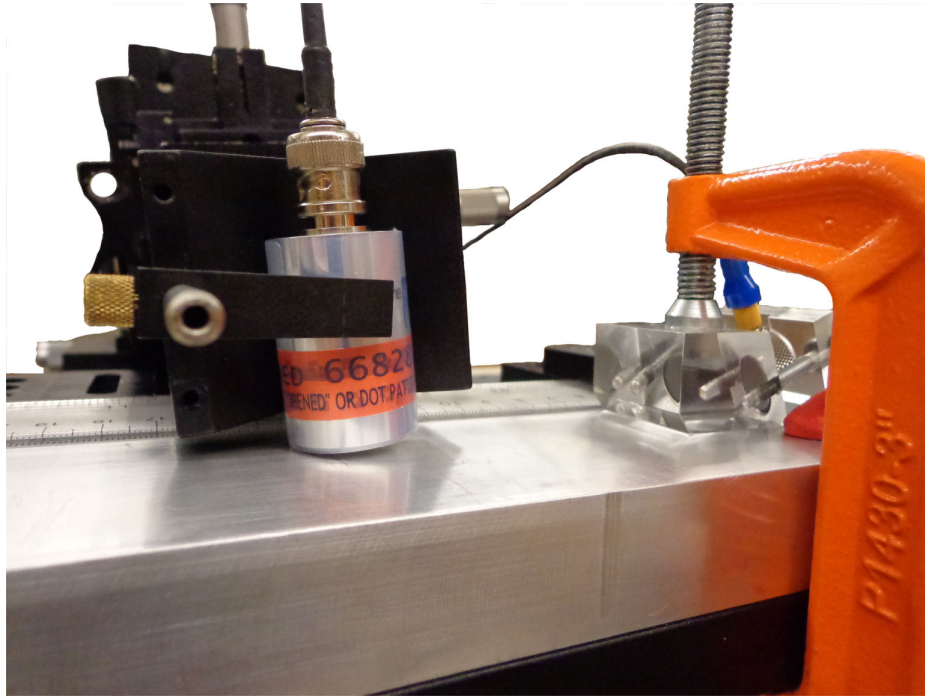


Figure 5.2: Transducer setup of experiments with view from the side.

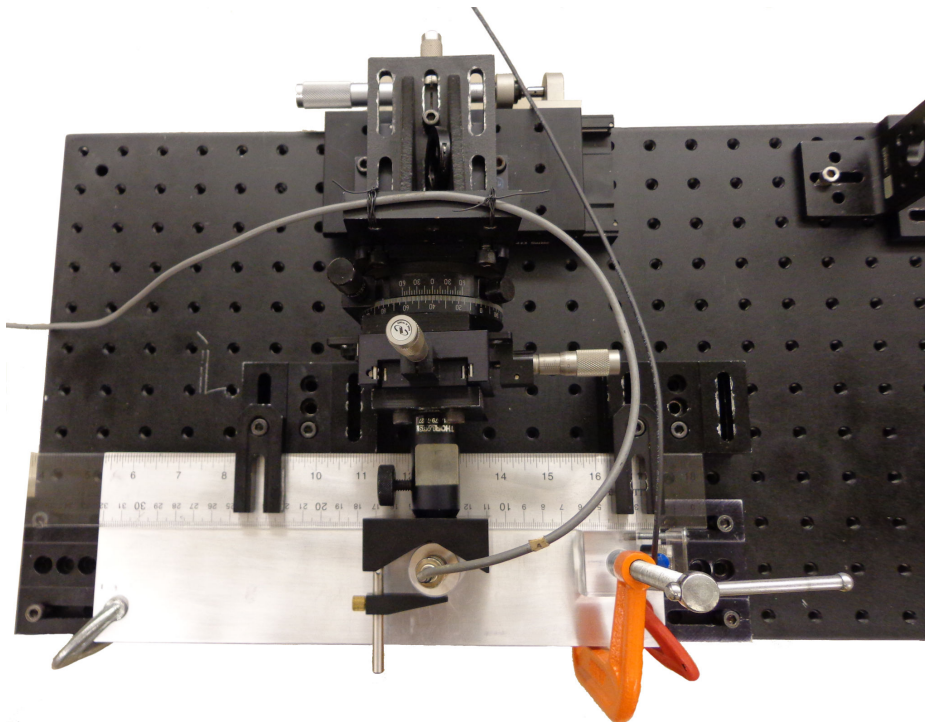


Figure 5.3: Transducer setup of experiments with view from the top.

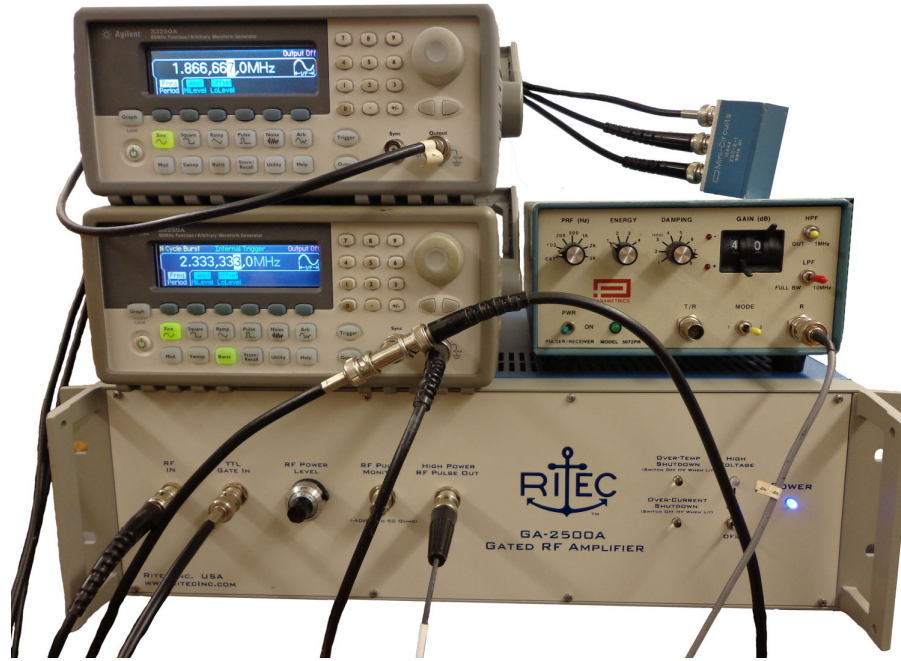


Figure 5.4: Technical devices used for experiments.

more detail about the involved adjustments and effects. The order of the devices explained will resemble the way the wave signal goes through the setup.

5.1.2.1 Function Generators

Two 80 MHz 33250A function/arbitrary waveform generator from Agilent are used to generate two different sine waves at different frequencies and variable amplitudes. They are the devices on the top left of Figure 5.4. Here, both signals are mixed in the small blue box. However, an ordinary link worked as well to mix the signals. It is important to point out, that in the conducted experiments we mix already the signal which feeds into one transducer instead of exciting two separate Rayleigh waves where the mixing is done in the material. If the chosen frequencies are close together it should be much easier to excite a clean Rayleigh wave by mixing before the transducer instead of afterwards. Furthermore, as drawn in Figure 5.1 one of the function generators has been used as the trigger source.

The number of cycles used for one sine wave was typically between 20 and 35, depending on what frequencies have been mixed and how many cycles it took to get enough steady-state data to which the post processing can be applied. A small number of cycles does not give enough steady-state data and too many cycles will lead to undesired reflections at the air-coupled transducer, which will be discussed in Section 5.1.2.5.

Moreover, the function generators will also be used in Section 5.2.2 to adjust the amplitudes of the single sine waves to investigate the effect of amplitude ratios on the experiment.

5.1.2.2 High Power Amplifier

The high power amplifier that has been used is a Ritec GA-2500A gated RF amplifier and is the large device on the bottom of Figure 5.4. The amplifier is crucial in nonlinear measurements, as we need high voltages to excite large enough Rayleigh waves that generate significant higher harmonics. If the amplification is too small the level 2 waves cannot be separated from noise within the measurements. The amplifier has also a pretty linear behavior which is important if we want to quantify nonlinear effects in the material.

The input to the amplifier is limited to around 1V from each wave component, which is the reason for the amplitudes used in section 5.2. The input voltage will then be amplified to actuate the transducer.

5.1.2.3 Excitation Device

The wedge method has been chosen as excitation method which is a so-called contact method. A typical plastic wedge with a narrow-band V106 piezoelectric transducer of Panametrics centered at 2.25 MHz has been used. The transducer mounted to the wedge can be seen in Figure 5.5. Here, the angle where the transducer is attached to the plastic wedge is designed as explained in Section 2.3.6.1. According to [11] it is

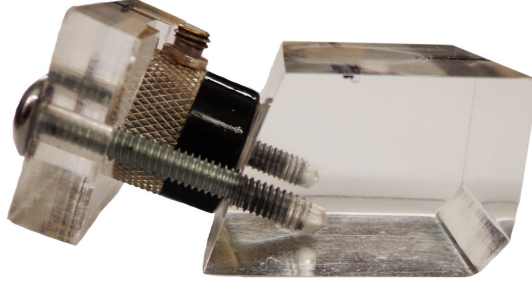


Figure 5.5: Plastic wedge with exciting transducer centered at 2.25 MHz.

important to keep the propagation distance of the P-wave through the wedge small, as diffraction effects will change the incident angle on the wedge-specimen boundary. Thus, also P- and S-waves are generated leaving a smaller portion of the input energy for the Rayleigh wave, which makes measurements more difficult. Also, the angle on the right side of the wedge serves to increase the propagation distance for reflected waves within the wedge to keep their influence small.

Finally, it is important to have a good coupling between wedge and specimen and wedge and transducer. This is done by the fixations but also by oil couplings.

5.1.2.4 *Specimen*

The specimen used is made of 7075-T651 aluminum and has the dimensions of 0.0254m thickness, 0.1016m width and 0.3048m length. Its elastic properties have been stated in [35] and are shown in Table 3.3. This specific kind of material has been chosen as it has low attenuation, which makes it possible to conduct experiments over a longer domain before the level 2 signals begin to fall. Thus, more data points can be measured within the region where the acoustic nonlinearity parameter β is relatively constant. When the waves are attenuated too much one needs to compensate for the attenuation. As the experiments in Section 5.2 have been done in the far field, we will already see a decline of the level 2 waves for higher propagation distances even for the low attenuating aluminum that has been used. Consequently, it might be already useful to compensate for attenuation and also diffraction. This

will be discussed in closer detail in Section 5.2.4.

Besides, we can investigate if the plate thickness is sufficient in order to check that we do not have much reflections at the ground of the specimen or that no Lamb waves will be formed [11]. Since the Rayleigh wave is evanescent we can get rid of these effects by choosing a large enough specimen thickness. As our experiments will be done with fundamental frequencies around 2MHz and a difference frequency component of at least 0.2MHz we obtain with

$$\lambda_w = \frac{c_r}{f} \quad (160)$$

and $c_r \approx 2923.31$ values of $\lambda_w(2MHz) = 1.4517mm$ and $\lambda_w(0.2MHz) = 14.517mm$. Thus, the plate thickness is about $17\lambda_w(2MHz)$ and $1.7\lambda_w(0.2MHz)$. Clearly, the thickness is sufficient for the fundamentals. In the case of the difference frequency the plate thickness is relatively small, but as the difference frequency does not carry much energy, the influence should still be small on the overall experiment. But the difference frequency itself could be affected. In Section 5.2 difficulties with the measurements of the difference frequency component will be pointed out and this might be one factor that contributes to the overall problem.

5.1.2.5 Detection Device

For detection the NCT4-D13 high frequency air-coupled transducer from Ultrasonics has been used with a peak and center frequency at 3.3MHz and a bandwidth of 1.1MHz at -6dB . The response of this non-contact transducer is shown in Figure 5.6, where the x-axis scale is 1.25MHz per division and the y-axis scale 10dB per division. It can be seen within this diagram that the performance of the transducer is highly dependent on the frequency, meaning that different frequency components within a signal will be scaled differently. Note that most experiments have been conducted close to a fundamental center frequency of 2.1MHz instead of the 2.25MHz transducer center frequency for excitation as the air-coupled is centered at 3.3MHz and gave better

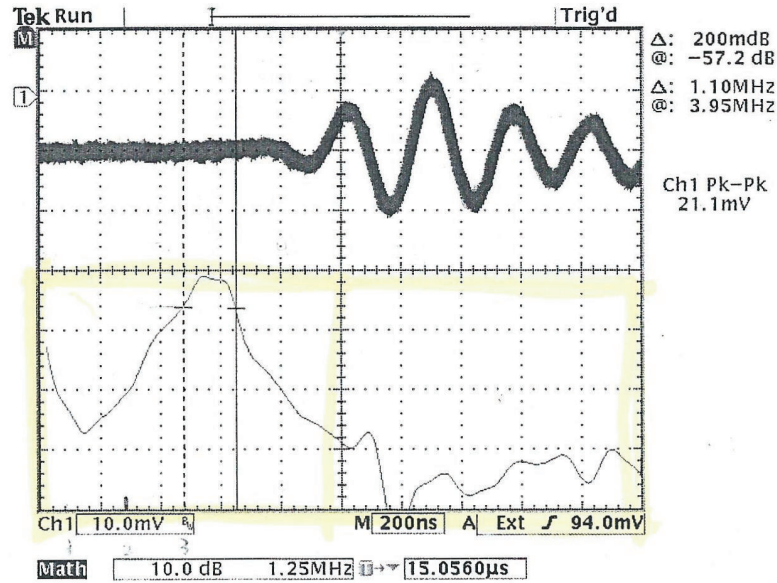


Figure 5.6: Frequency response of air-coupled transducer from the Ultrason group.

results for level 2 waves closer to 3.3MHz. Furthermore, the air-coupled transducer works in principle just like the wedge transducer. The Rayleigh wave that travels through the surface will leak a P-wave into the surrounding air. Thus, the air acts similar to the plastic wedge and one can measure this P-wave.

Also, it is important to send a wave packet through the specimen which is not too long. The P-wave will be reflected at the surface of the transducer and again reflected at the surface of the specimen and then travel back to the transducer. Thus, we need to choose the length of the wave packet according to the lift-off distance between specimen and transducer in order that we do not measure reflected waves. Therefore, a large lift-off distance would be desirable to measure more wave cycles. However, the lift-off distance cannot be too large as the damping in air is relatively high and we would not get a good signal for larger distances. So there is a trade-off between both effects.

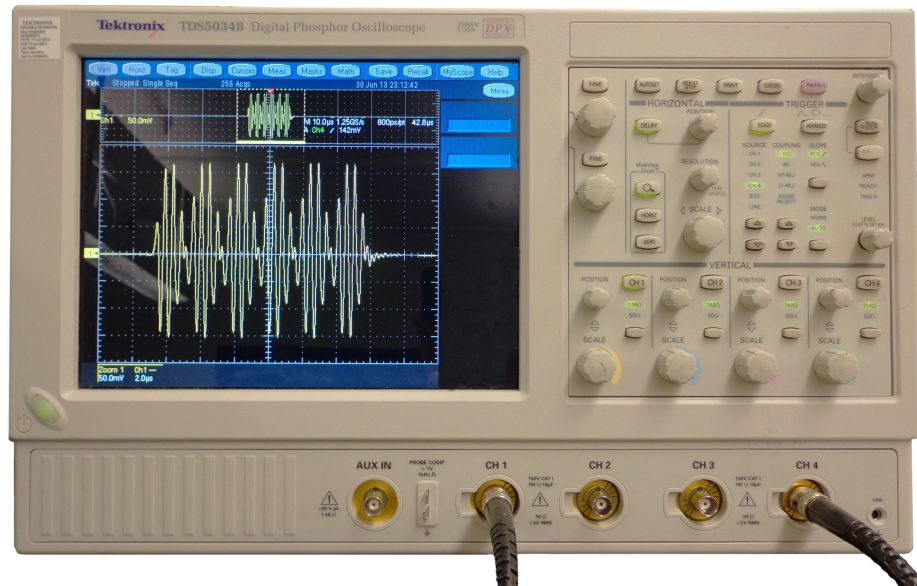


Figure 5.7: Oscilloscope showing measured signal of two mixed Rayleigh waves at 2.666667 and 1.866667 MHz.

5.1.2.6 Receiver

The 5072PR Panametrics Receiver that has been used is the device on the right on the amplifier in Figure 5.4. The most important setting here is the gain, which is set to 40dB. A gain is often important as the measured signal is relatively low. However, if we use the receiver with a small gain the noise will be increased within the signal, as the receiver adds a certain amount of noise itself. If we further increase the gain to a reasonable number, the influence of the receiver noise will be low compared to the amplification of the signal.

5.1.2.7 Oscilloscope

A TDS5034B Digital Phosphor Oscilloscope of Tektronix has been used within the experiments. A photograph is shown in Figure 5.7. Within this figure we see the measured signal of two mixed Rayleigh waves. To obtain a clearer signal an average of 256 samples has been taken as basis for signal processing. The signal processing for the experiments has been similar to Section 4.2.2. The DFT of the time domain

signal has been realized with the fft command in Matlab.

5.2 Experimental Results

Within the experiments there are basically three steps. The first is to show that we can use the mixing technique in general to obtain the acoustic nonlinearity parameter β and how the m. The second step analyses the influence of variation of the initial amplitudes of the fundamental waves with fixed frequencies. And in the third step the mixing frequencies are varied while the initial amplitudes of the fundamentals are held fix.

5.2.1 Feasibility of Rayleigh Wave Mixing

First of all basic tests have been performed to see if we can measure the four level 2 components and if they grow over the propagation distance when damping is small. This could help to obtain more information from a single experiment as compared to a one wave case. For the sum frequency and the second harmonics, it was relatively unproblematic to get good results. However, the difference frequency was difficult to measure. Tests have been made for a center frequency of the fundamentals of $f_c = 2.1\text{MHz}$ and a $\phi = 0.8$, which means that the frequencies at 2.333333MHz and 1.867777MHz are used. Therefore, it was impossible to measure the difference frequency of 0.466666MHz with the air-coupled transducer which is centered at 3.3MHz , as the amplitude is too weak as shown in Figure 5.10. Thus, a wedge transducer has been used also for the receiving part with transducers centered at 0.5MHz and 1MHz . The difference frequency could in fact be measured relatively easily but the behavior over the propagation distance was not meaningful. A reason for this behavior is that the transducer cannot measure the high frequencies accurately, which distorts the time domain signal too much. This has also been tested for mixing frequencies at 10 and 13MHz but a meaningful detection with a wedge transducer centered at 5MHz and the air-coupled were not possible. As a result, a broadband detection

technique like laser measurements, broadband microphones or accelerometers could resolve this problem. As it has recently been shown that the difference frequency of Rayleigh wave mixing can actually be used to measure β in concrete with broadband techniques [10].

On the excitation side one could vary the FMR to obtain a larger difference frequency that is closer to the other frequency components. However, either two exciting transducers are necessary when exciting far away from having a beating phenomena which means smaller FMRs. Then one would need to perform the wave mixing in the specimen which is rather difficult. Or also a broadband transducer needs to be taken for excitation purposes. Also, a very small FMR with an easy transducer motion might be possible to realize with only one transducer, but then it would be more difficult to measure several level 2 waves at the same time as they are more spread out and the sum and difference frequency are also closer to the fundamentals which could cause overlaps in the DFT. Thus, larger FMRs were easier to handle with the available equipment to perform basic investigations on the Rayleigh wave mixing method which is the reason why only large FMRs will be considered in the following.

Consequently, as the difference frequency component is too involved for the scope of this thesis and has already been investigated before and can be used to measure β [10], the further analysis will focus solely on the other three level 2 waves which gave very good results with the air-coupled transducer. With the described narrow band transducers of Section 5.1.2 it is usually recommendable to excite with a FMR close to one to have a beating, as this motion is easy to realize since the involved frequencies are close to each other which results in an easier motion for the exciting transducer to follow and the frequencies, except the difference frequency, can be chosen close to the center frequencies of the exciting and detecting transducers.

The measured data has been processed similarly to Chapter 4 and is summarized in Figure 5.8. The different steps within this procedure will be discussed in the fol-

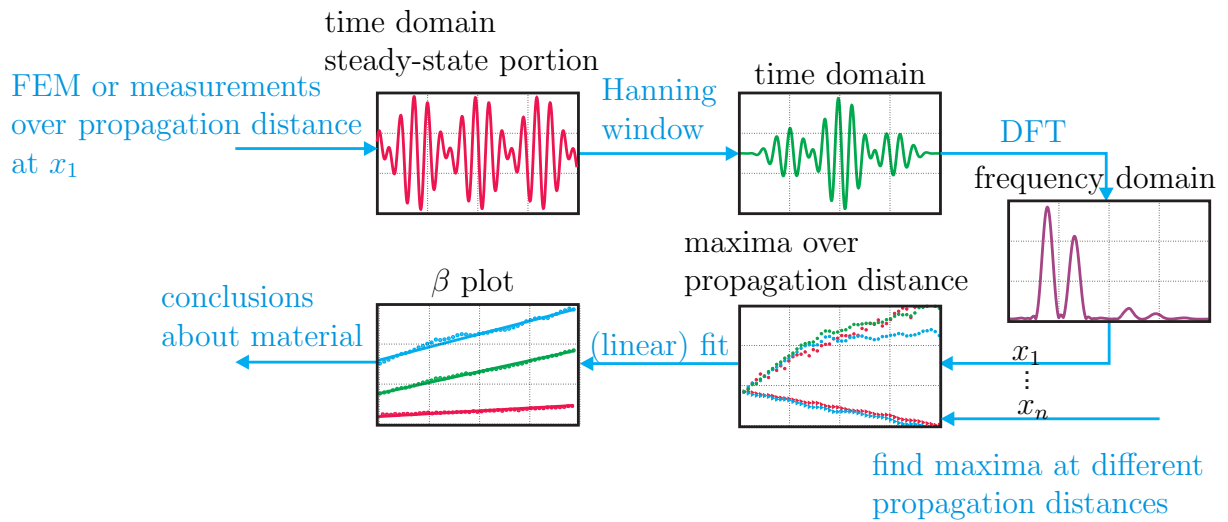


Figure 5.8: Workflow in processing of the time domain signal obtained within experiments.

lowing. Results of the measured time domain signal can be seen in Figures 5.7 and 5.9. Despite the rather difficult excitation, the measured signal looks relatively clean. When we apply the illustrated Hanning window on a steady-state portion of the time domain signal, we obtain the DFT shown in Figure 5.10.

The different frequency components are clean, well separated and have a high enough amplitude to be not influenced too much by noise. It is important to note that the amplitudes in 5.10 do not say much about the real world signal, as the air-coupled transducer has a certain response over frequency as shown in Figure 5.6 as well as the exciting transducer. Thus, we cannot compare the amplitudes of the different frequency components against each other but only the same frequency components for different measurements as done in the next sections. Thus, the even the fundamental amplitudes differ although we applied the same voltage for both waves. To be able to compare different frequencies, we would need to conduct absolute measurements with for example a laser which was out of the scope of this thesis. As a result, the amplitudes and later calculated β values are only relative measure.

Note, that the original DFT amplitudes have been back calculated to the time domain

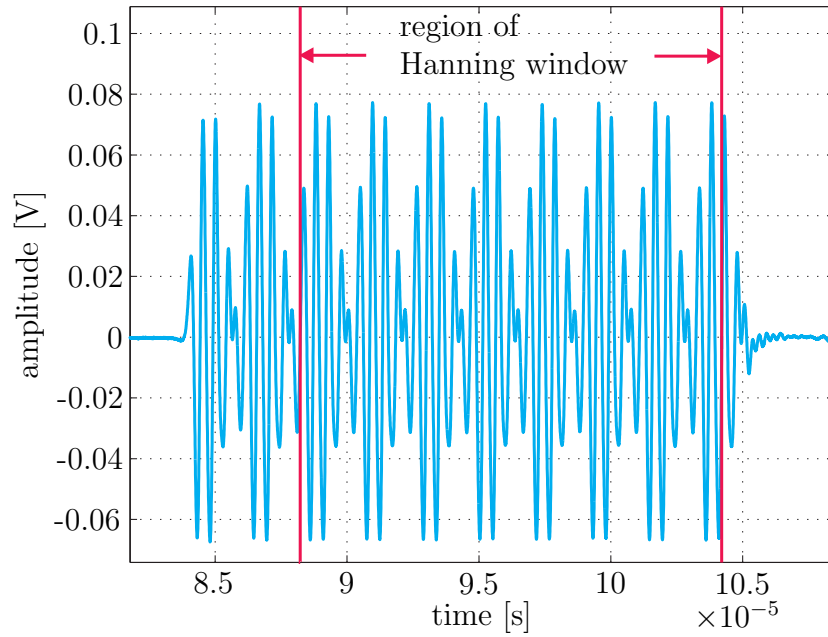


Figure 5.9: Measured time domain signal at 78mm propagation distance for mixing a 2.333333MHz with a 1.867777MHz wave both at 700mVpp output from the function generator.

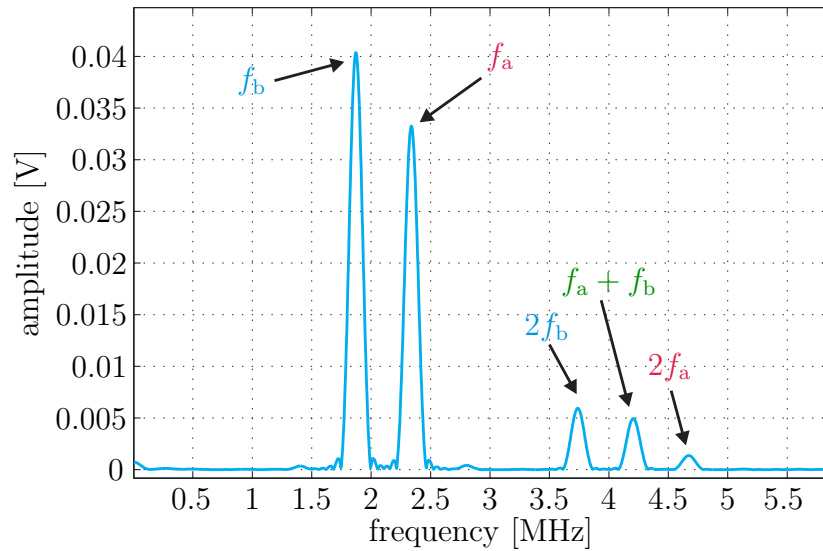


Figure 5.10: DFT of the time domain signal of Figure 5.9 with an applied Hanning window.

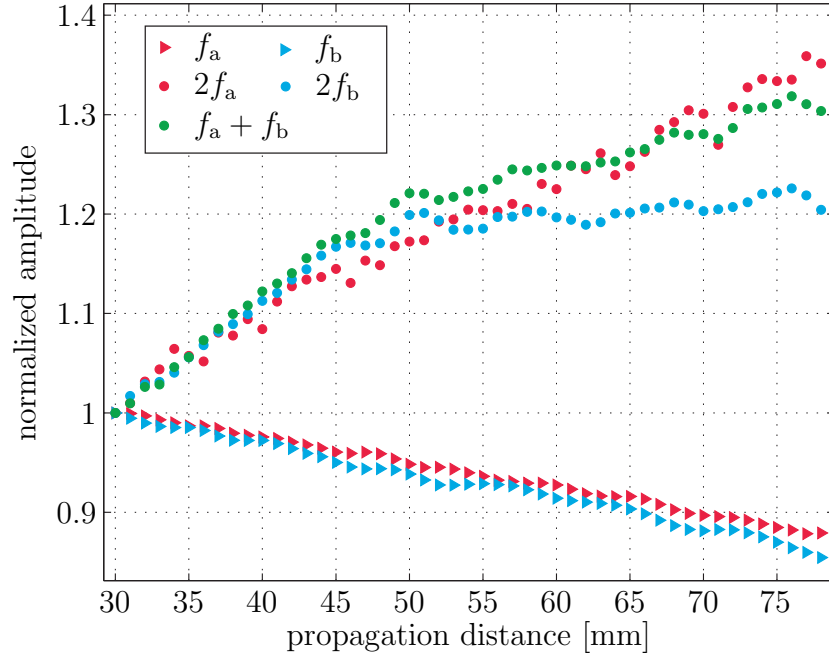


Figure 5.11: Amplitudes of different frequency components over the propagation distance with the parameters of Figure 5.9.

signal with the approximate formula of Equation 158. After incorporating this formula, we just need to read off the maxima to get the approximate amplitude of each component within the time domain signal. If we take now measurements at positions from 30 to 78mm in 1mm steps, apply the discussed steps and calculate the according maxima, we obtain the plot in Figure 5.11, which has been similarly measured for the other experiments of the set which incorporated different fundamental frequencies and amplitudes. Here, each component has been normalized to its value at 30mm. In this plot we can see the typical characteristic of fundamentals and level 2 waves, which are generated through nonlinearity. The fundamental waves fall of with a relatively small percentage but the level 2 waves rise with a higher percentage. The reason is that the fundamentals have much higher absolute values and therefore their relative change is usually smaller in the beginning. It can also be observed that the fundamentals rise for small propagation distances in an almost linear manner but begin to drop of later. As the measurements are conducted in the far-field of the Rayleigh waves diffraction and damping effects become dominant over the generation of level 2 waves at larger

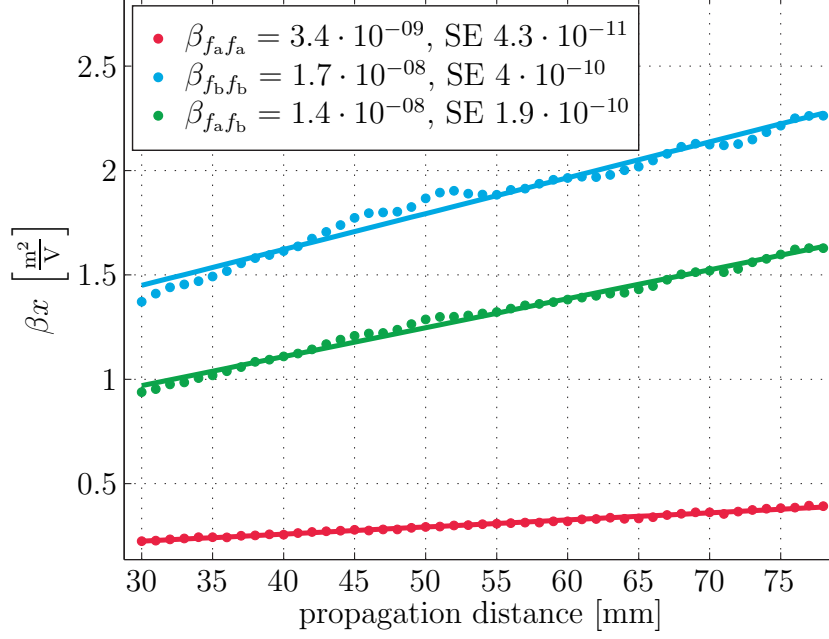


Figure 5.12: β times x for different level 2 components.

propagation distances. In all conducted measurements it has been observed that the $2f_b$, which has the smallest frequency of the level 2 waves measured, drops of first. A possible explanation is that because of the lower frequency it is experimentally much harder to generate higher harmonics when damping and diffraction effects become larger. Also the $2f_a$ component gave in general the uncleanest measurements. The reason is that it is the highest measured frequency and thus relatively far away from the center frequency of the air-coupled transducer making the signal small, which is harder too measure and to separate from noise. Also, if the input amplitudes of the fundamentals are low, we will obtain worse data for the $2f_a$ component, as small fundamental amplitudes reduce the amplitudes of the level 2 waves as well. If we now use the calculated amplitudes and apply the β formulas derived in section 3.5 and multiply them with the propagation distance, we obtain the plot shown in Figure 5.12.

It should be pointed out that we measure a P-wave with the air-coupled transducer and therefore we do not directly have the Rayleigh wave amplitudes available as

defined in needed within the β formulas. However, as we got a certain response for the combination of both transducers anyway that has not been quantified, we will just use the overall measured amplitudes for the amplitudes within the acoustic nonlinearity parameter to get a value that is at least proportional to β with an unknown proportionality factor. Besides, in Figure 5.12 a linear fit has been used to calculate β as the slope assuming a constant acoustic nonlinearity parameter. This is a common approach to obtain an approximate value for β . Note again, that the β values between the three illustrated curves cannot be compared because of different transducer response behavior. One should only compare the value of the same frequency for amongst others different amplitudes or specimen. The term SE in the legend stands for standard error calculated with the LinearModel.fit of Matlab and as this value is relatively small we can infer that the linear fit is reasonable. This finally means that we can use the mixing technique to measure the acoustic nonlinearity parameter of the material for the second harmonics and the sum frequency.

5.2.2 Variation of Amplitudes for Fixed Frequencies

After showing that the mixing technique gives feasible data a first set of experiments has been conducted. Here, only the amplitudes of the fundamental waves will be scaled but the frequencies will be fixed at 2.333333MHz and 1.866667MHz. As the displacement of the fundamental waves is approximately proportional to the output voltage of the function generators, the output voltages of both function generators have been varied among the values 350, 525 and 700mVpp which resulted in nine different measurement sets. Note that 525 is the mean of 350 and 700 and will later be useful to conduct experiments with a fixed center voltage. Fixed center output voltage means that the average of the voltages of both function generators stays fixed. Furthermore, all measurements have been conducted from 30mm to 78mm propagation distance with increments of 1mm. As the measurements turned out to be very

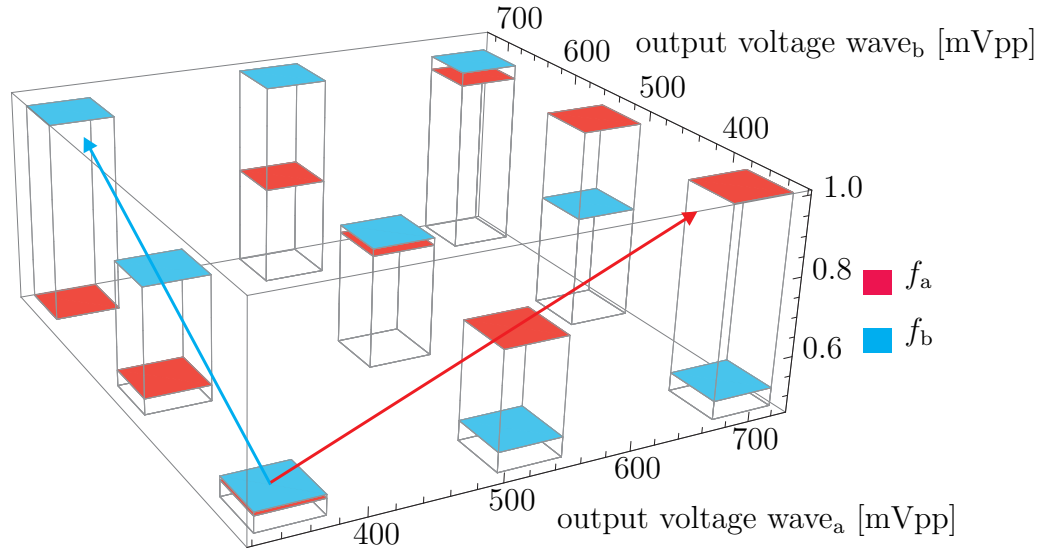


Figure 5.13: Average fundamental amplitudes over propagation distance normalized to their maxima for different output voltages of the function generators. Trends denoted by arrows.

repeatable, only one measurement per set has been obtained as the data was already very satisfying to do basic investigations concerning the mixing technique. If one would want to get reliable data to investigate material properties it is recommended to do more measurements.

In Figures 5.13 and 5.14 the normalized averages of the measured values over the propagation distances of the fundamentals plus the sum frequency and second harmonics are presented. The average has been taken as considering more data points helped to reduce the influence from outliers on the overall behavior. Also, a normalization has been conducted as the absolute values of the measured amplitudes are not physically meaningful because of the explained transducer characteristics or responses. Thus, normalization has been chosen for easier visualization. In Figure 5.13 the axis directions of the trends of the measured amplitudes are shown by arrows. As one would expect from the simplified mixing model from Section 3.2.1 the f_a rises linearly with an increased voltage output of the function generator of wave_a. Thus, with a doubling of the voltage from 350 to 700 mVpp, the normalized amplitude

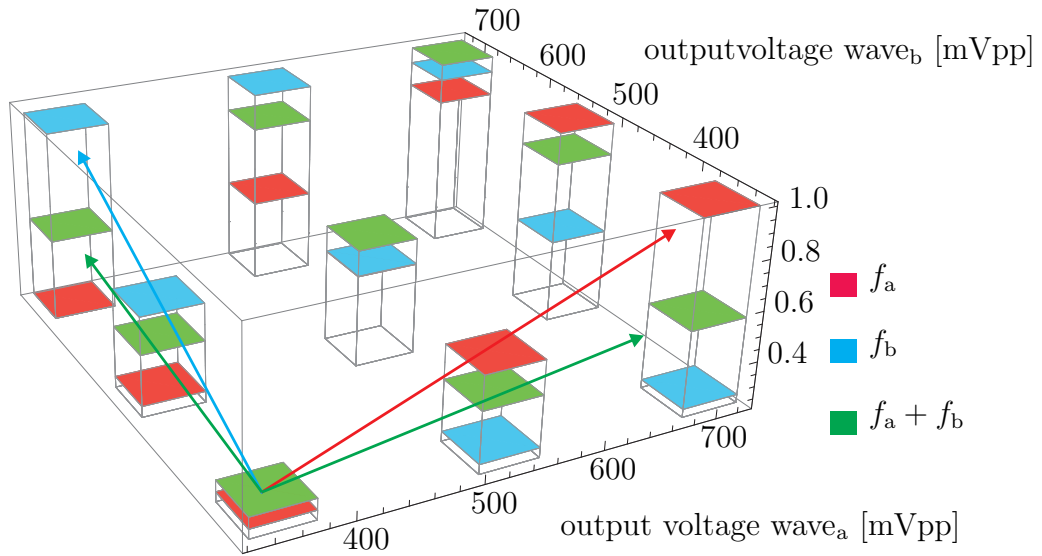


Figure 5.14: Average level 2 wave amplitudes over propagation distance normalized to their maxima for different output voltages of the function generators. Trends denoted by arrows.

doubles approximately as well from around 0.5 to 1.0 while the amplitude of the f_b component stays relatively constant. This holds analogously for an increased voltage output of the function generator of wave_b.

In Figure 5.14 we see similar trends for the $2f_a$ and $2f_b$ components only that they scale with the square of the fundamental amplitudes as predicted by the Equations within Section 3.2.1. Thus, when we double the voltage of a function generator, the according second harmonic will rise with a factor of approximately four. Compared to this, the sum frequency rises only linear but in both axis directions as it depends on both fundamental amplitudes. These results are well in line with theory. It should also be pointed out that for a fixed center output voltage the sum frequency is highest if the voltages of both function generators are close to each other according to 3.2. Specifically, this effect means that the amplitude of the sum frequency at 525mVpp for both outputs is higher than at 700 mVpp for one and 350mVpp for the other output making the green bar in the middle in Figure 5.14 higher than the ones in the left and right corners. In the experiments the 525mVpp setup was of factor of

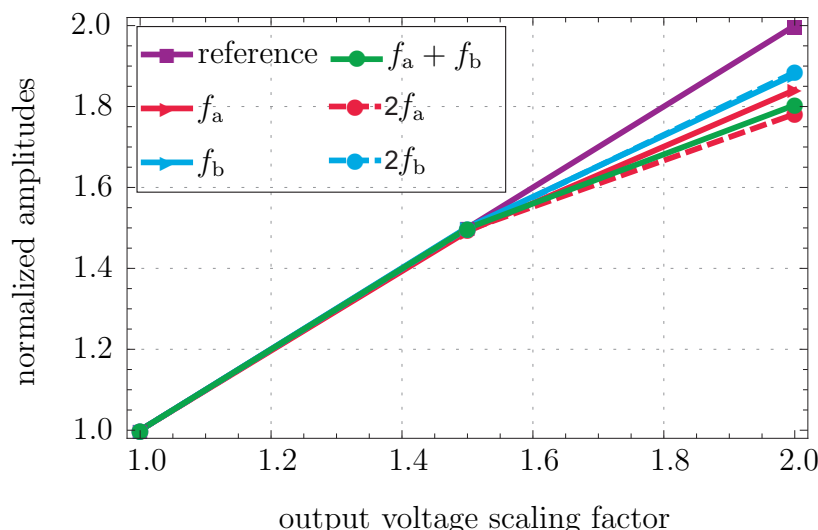


Figure 5.15: Dependence of measured amplitudes on simultaneous scaling of the output voltage of both function generators. All components are normalized to the first data point. The fundamentals are plotted linearly whereas the square root is taken of all level two waves. The reference curve has a slope of one.

1.2206 larger than when the output of wave_a was 700mVpp and 350mVpp for wave_b. For the setup with exchanged amplitudes of wave_a and wave_b, the factor was 1.2626. However, it is important to realize that the fundamental waves scaled very linearly and the level two waves very quadratically from 350 to 525mVpp. This can be observed in Figure 5.15 where both output voltages have been increased at the same time. However, between 525mVpp and 700mVpp there is no linear development anymore. The reason is that the exciting transducer has reached its limit and is not able to deliver more amplitude even if the voltage is higher. Thus, if we correct for this amplitude decrease and multiply a correction factor to increase the fundamental amplitudes to fit the reference curve we can recalculate the obtained results for the sum frequency increase. So instead of of 1.2206 we obtain $1.2206/1.08=1.1302$ and instead of 1.26257 we obtain $1.2626/1.065=1.1855$ which are now much closer to the theoretical factor for the simplified model of $525^2/(700 * 350) = 1.125$. To confirm this increase of the sum frequency another measurement solely in the linear region of Figure 5.15 could be done in the future, so that no correction needs to be applied.

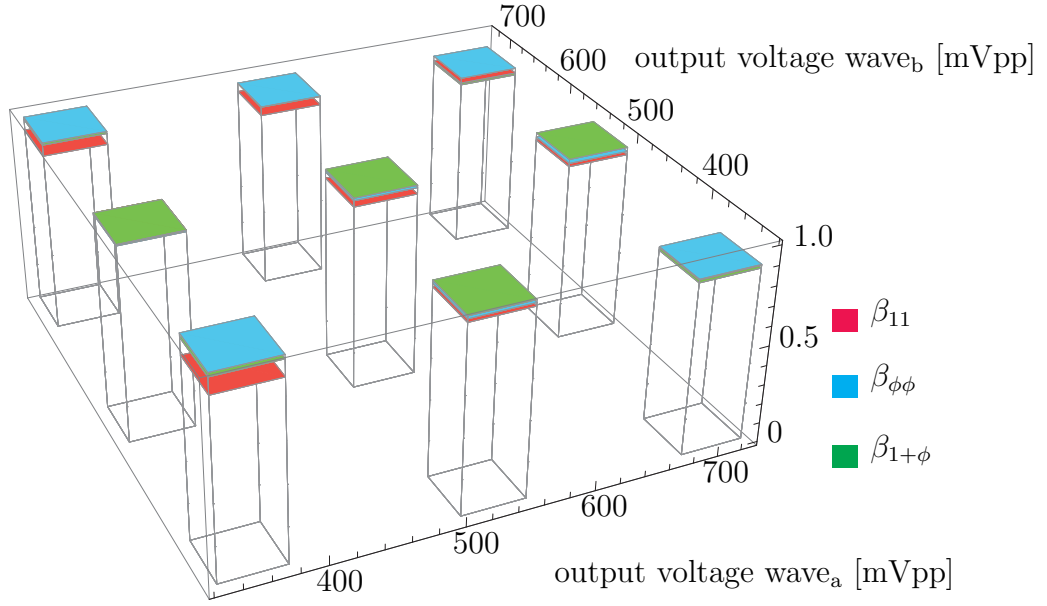


Figure 5.16: Value of linear fit for different β 's normalized to their maxima for different output voltages of the function generators.

Subsequently, when we compare the normalized β 's for three considered level 2 waves for different voltage outputs we obtain the plot within Figure 5.12. As expected all β 's are approximately constant. The reason is that in the β formulas we find the proportionality for appropriate pairs of fundamentals and level 2 waves as

$$\beta \propto \frac{\text{level 2 wave}}{\text{product of two fundamentals}}. \quad (161)$$

And as the product of the fundamentals scales the same way as the level 2 waves, the β stays approximately constant what is physically evident as the acoustic nonlinearity parameter β is independent of the applied voltage.

Finally, we can state that voltage output variation is a good means to check the amplitude dependence of the different frequency components, as the transducers responses stay constant for fixed frequencies and the wedge transducer and the amplifier behave relatively linear. Also, it is not important that the actual relative amplitudes measured differ from the voltage output of the function generators as the amplitudes behave approximately multiplicative. Therefore, all discussed results hold even for

the DFT shown in Figure 5.10 where the fundamental amplitudes have a large difference although the same voltage output has been used for both wave components. As this factor between both fundamentals does not change much, it has no influence on the interpretations presented in this section.

5.2.3 Variation of Frequencies for Fixed Amplitudes

In a second set of experiments, the output voltages of both function generators have been fixed at 700mVpp and the frequencies have now been varied between 1.75 and 2.49MHz. Comparisons with the theory have shown that the transducer characteristic is dominant over small variations in the FMR. It has been tried to compensate for the air-coupled transducer frequency response as illustrated in the data sheet in Figure 5.6. However, there are many other parameters that change when the frequencies are varied, like the exciting transducer characteristic. As there were too many unknowns, it was impossible to compare this set of experiments to theoretical investigations and results obtained for example in Section 3.2. Nevertheless, for a fixed center frequency at 2.1MHz, the sum frequency stays constant at 4.2MHz and should therefore not be affected by the frequency response of the detecting transducer. When we now plot the amplitude of the sum frequency over different FMRs we obtain the plot illustrated in Figure 5.17. According to the theory it makes sense that the amplitude of sum frequency rises for higher FMR. But nevertheless, the increase is too large to be caused only by the different frequencies. As the exciting transducer now has relatively large influence on the results compared to the other components, the increase of the sum frequency amplitude is most likely related to the easier excitation for the higher FMRs as we are using a narrow band transducer which works well when the frequencies to excite are close to the center frequency and as the motion of the transducer displacement is less complex for similar frequencies. It is also possible that the transformation of the excited P-wave into a Rayleigh wave is sensitive to

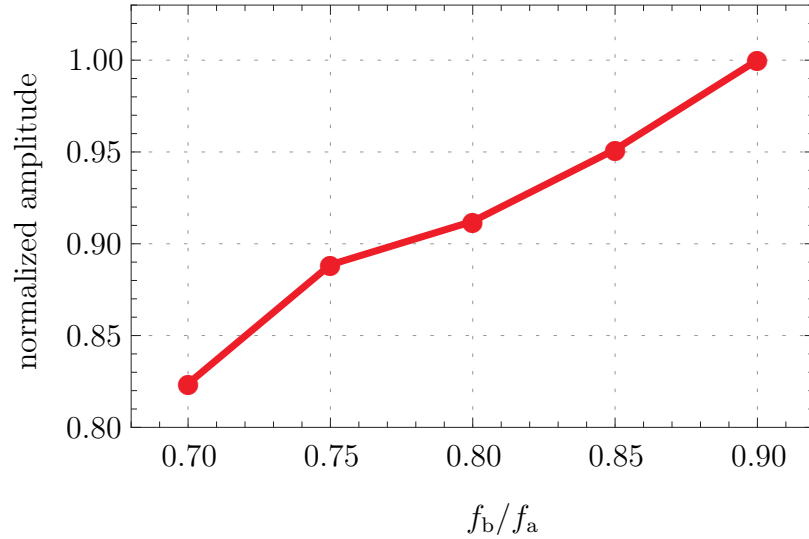


Figure 5.17: Amplitude of sum frequency normalized to last data point for fixed center frequency at 2.1MHz for different f_b/f_a .

the frequency similar to the results in Chapter 4 or that for example diffraction and damping effects have already a not negligible influence. However, these question are open to be investigated in the future.

5.2.4 Comparison of Experiments with Analytical Model

In the following it will be shown how the simplified diffraction model of Section 3.4 can be used to compensate for diffraction and damping. The idea is to fit the equations for the fundamentals and the partial differential equations of the level 2 waves to the experimental data. The result of the applied fitting on the data shown in Figure 5.11 is presented in the plot of Figure 5.18. By using the least squares method, the theoretical model could be fitted to the experiments. The fitting parameters have been the damping parameter of each wave component and a scaling factor which accounts for the transducer characteristics. Also, experiments show that the utilized transducers produce level 2 waves by themselves. This has been qualitatively taken into account by fitting a Gaussian initial condition of the level 2 waves with $a_s = 6.35\text{mm}$. It should be pointed out that these values should be the same for different specimen as it is a transducer characteristic. This means that it is

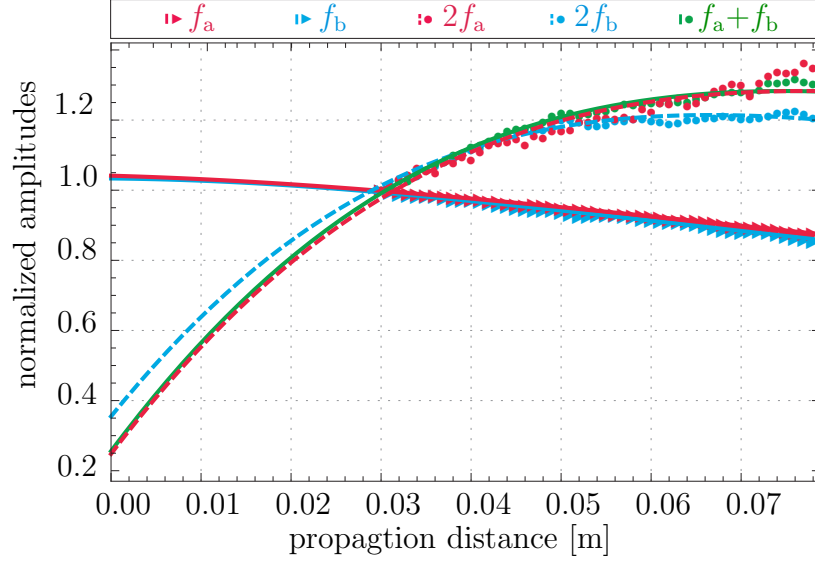


Figure 5.18: Simplified diffraction model of Section 3.4 fitted to normalized experimental data shown in Figure 5.11.

desirable to measure the transducer nonlinearity independently first and then apply a fixed value to the different experiments. This has not been tested within this thesis and therefore the transducer nonlinearity stays unknown. But it would be necessary to characterize it in the future to test the feasibility of this initial nonlinearity. Also, the obtained attenuation values of the fundamentals seem reasonable with 0.71Np/m for f_a and 0.24Np/m for f_b . However, the attenuation factors of the level 2 waves were 19Np/m for $2f_b$ and 21Np/m for $2f_b$ and $f_a + f_b$. These values seem to be relatively high and could be connected to the fact that the initial nonlinearity that gives the best fits might be much lower than the actual nonlinearity from the transducer. As this means that the curves start at a smaller initial value, the damping needs to be larger to follow the decrease of the level 2 waves for higher propagation distances. As we got now results for the fundamentals and level 2 waves at $x = 0$, we can take the slope of

$$\frac{16\text{sign}(lm)b_{l+m}}{(l+m)k_{|l|}k_{|m|}b_l b_m} \quad (162)$$

at $x = 0$ for a l and m of 1 or $\pm\phi$ according to the considered components. The b 's denote the fitted amplitudes. This yields a β that is corrected for diffraction and damping and should theoretically only be different from the true β by a factor caused by the measurement instruments. So in the case of absolute measurements one should be able to calculate the true β at $x = 0$. Besides, the different normalization of each component is only done for a more compact representation but should not be done when comparing different materials. Finally, we can conclude that there are relatively simple ways of correction for diffraction, attenuation and transducer nonlinearity to get the β value at $x = 0$ where we cannot measure. However, the presented approach needs to be validated by applying it to different materials.

CHAPTER VI

CONCLUSION AND FUTURE WORK

6.1 Conclusion

The results of this thesis show that it is possible to use Rayleigh wave mixing to measure the acoustic nonlinearity parameter β to quantify material damage on up to four ways. Several links could be shown between the analytical, finite element method and experimental investigations that support the feasibility of the used approaches and the mixing approach itself.

First, analytical investigations have been undertaken and simulation models developed that focus on the different domains like small propagation distances or different effects like diffraction. With a simplified model general relations have been derived that show how one can choose the mixing frequencies and initial amplitudes to maximize the considered level 2 wave. It has been shown that in the case of low attenuation and high propagation distances, the horizontal velocity component forms a shock and the vertical velocity a pulse independent of the frequency mixing ratio. Moreover, general relationships between frequencies and amplitudes for mixed collinear Rayleigh waves have been developed to enable selection of best frequency and amplitude ratios for amplitude maxima. Furthermore, it has been shown how one can relate the amplitudes of the different mixing frequencies to obtain the same acoustic nonlinearity parameter β in order to be able to measure the same quantity in up to four different ways.

The analytical model has been validated with a finite element simulation for small propagation distances. Here, the power of the analytical solution becomes apparent: the simulation time is much smaller and the possibility to take into account a range

of more than hundred harmonics without a problem.

Finally, experiments could confirm that the acoustic nonlinearity parameter β is measurable for Rayleigh wave mixing. Furthermore, the analytically modeled amplitude relations could be confirmed. Experiments also show that mixing requires careful planning of frequencies excited and generated in the system as amongst others transducer responses will be different for different frequency components or frequency mixing ratios. These differences between experiment and theory limit the possibility of comparison to a certain extent.

6.2 Future Work

The mixing technique offers new possibilities to improve measurements of acoustic nonlinearity. To fully validate the technique, detailed studies on different materials should be conducted and compared to theoretical predictions. A well-founded study would be important to show the robustness in real world applications.

An open question that has not been cleared regarding the FEM simulation is, amongst others, if the analytical diffraction model can be validated. Therefore it would be advantageous to write an own code to get a better speed up than the speed up within COMSOL for this specific problem. The two dimensional FEM simulation could also be used for larger propagation distances where level 3 components get significant in order to confirm the analytically modeled interactions with more involved components in closer detail. Moreover, the transfer of energy from an excited P-wave in a wedge to a Rayleigh surface wave could be investigated in closer detail. As FEM simulations showed a significant amplitude change for a variation in frequency, it might be of great value to understand this energy transfer process to excite larger Rayleigh waves. This is important as they generate second harmonics that depend on the square of the fundamental amplitudes.

In regard of the experiments it would be very interesting to use a broadband excitation and measuring technique to test if the difference frequency component can be measured in a way that the results can be used for material characterization. Also, a full characterization of the involved transducers could help to extend the theoretical model to calculate more accurately what frequencies and amplitudes of the fundamental waves should be chosen to maximize the considered level 2 wave. Finally, to validate the diffraction and damping correction of Section 5.2.4 transducer nonlinearities could be characterized.

References

- [1] ACHENBACH, J., *Wave Propagation in Elastic Solids (North-Holland Series in Applied Mathematics and Mechanics)*. North Holland, 1973.
- [2] BARNARD, D. J., “Variation of nonlinearity parameter at low fundamental amplitudes,” *Applied Physics Letters*, vol. 74, no. 17, p. 2447, 1999.
- [3] BONIFACIO, R., CALOI, R., and MAROLI, C., “The slowly varying envelope approximation revisited,” *Optics Communications*, vol. 101, pp. 185–187, Aug 1993.
- [4] CANTRELL, J. H., *Ultrasonic Nondestructive Evaluation: Engineering and Biological Material Characterization Chapter 6*. CRC Press, 2003.
- [5] CANTRELL, J. H. and YOST, W. T., “Effect of precipitate coherency strains on acoustic harmonic generation,” *Journal of Applied Physics*, vol. 81, no. 7, p. 2957, 1997.
- [6] CHEEKE, J. D. N., *Fundamentals and Applications of Ultrasonic Waves (CRC Series in Pure and Applied Physics)*. CRC Press, 2002.
- [7] CROXFORD, A. J., WILCOX, P. D., DRINKWATER, B. W., and NAGY, P. B., “The use of non-collinear mixing for nonlinear ultrasonic detection of plasticity and fatigue,” *The Journal of the Acoustical Society of America*, vol. 126, no. 5, p. EL117, 2009.
- [8] DAVID, E., “A uniform asymptotic solution for nonlinear surface acoustic waves,” *International Journal of Engineering Science*, vol. 23, no. 7, pp. 699 – 708, 1985.
- [9] GRAFF, K. F., *Wave Motion in Elastic Solids (Dover Books on Engineering)*. Dover Publications, 1991.
- [10] GROSS, J., “Evaluation of near surface material degradation in concrete using nonlinear rayleigh surface waves,” Master’s thesis, Georgia Institute of Technology, 2012.
- [11] HERRMANN, J., “Generation and detection of higher harmonics in rayleigh waves using laser ultrasound,” Master’s thesis, Georgia Institute of Technology, 2005.
- [12] HERRMANN, J., KIM, J.-Y., JACOBS, L. J., QU, J., LITTLES, J. W., and SAVAGE, M. F., “Assessment of material damage in a nickel-base superalloy using nonlinear Rayleigh surface waves,” *Journal of Applied Physics*, vol. 99, no. 12, p. 124913, 2006.
- [13] JONES, G. L., “Interaction of elastic waves in an isotropic solid,” *The Journal of the Acoustical Society of America*, vol. 35, no. 1, pp. 5–10, 1963.

- [14] KALAYANASUNDARAM, N., “Nonlinear mode coupling of surface acoustic waves on an isotropic solid,” *International Journal of Engineering Science*, vol. 19, pp. 435–441, Jan 1981.
- [15] KALYANASUNDARAM, N., “Nonlinear surface acoustic waves on an isotropic solid,” *International Journal of Engineering Science*, vol. 19, pp. 279–286, Jan 1981.
- [16] KALYANASUNDARAM, N., “Coupled amplitude theory of nonlinear surface acoustic waves,” *The Journal of the Acoustical Society of America*, vol. 72, no. 2, pp. 488–493, 1982.
- [17] KALYANASUNDARAM, N., “Nonlinear mixing of surface acoustic waves propagating in opposite directions,” *The Journal of the Acoustical Society of America*, vol. 73, no. 6, pp. 1956–1965, 1983.
- [18] KIM, J.-Y., *Ultrasonic and Electromagnetic NDE for Structure and Material Characterization: Engineering and Biomedical Applications, Chapter 8*. CRC Press, 2012.
- [19] KINSLER, L. E., FREY, A. R., COPPENS, A. B., and SANDERS, J. V., *Fundamentals of Acoustics. 4th ed. International ed.* John Wiley & Sons, 2000.
- [20] KOLSKY, H., *Stress Waves in Solids (Dover Phoenix Editions)*. Dover Publications, 1963.
- [21] KOPYLOV, Y. V., POPOV, A. V., and VINOGRADOV, A. V., “Application of the parabolic wave equation to x-ray diffraction optics,” *Optics Communications*, vol. 118, pp. 619–636, Aug 1995.
- [22] LANDAU, L. D. and LIFSHITZ, E. M., *Theory of Elasticity (Course of Theoretical Physics)*. Pergamon Press, 1970.
- [23] LANDAU, L. and LIFSHITZ, E., *Mechanics (Course of Theoretical Physics)*, vol. 1. Pergamon Press, 1976.
- [24] LARDNER, R., “Waveform distortion and shock development in nonlinear rayleigh waves,” *International Journal of Engineering Science*, vol. 23, pp. 113–118, Jan 1985.
- [25] LIU, M., TANG, G., JACOBS, L. J., QU, J., THOMPSON, D. O., and CHIMENTI, D. E., *Measuring acoustic nonlinearity by collinear mixing waves*, pp. 322–329. American Institute of Physics, 2011.
- [26] LIU, M., TANG, G., JACOBS, L. J., and QU, J., “Measuring acoustic nonlinearity parameter using collinear wave mixing,” *Journal of Applied Physics*, vol. 112, no. 2, p. 024908, 2012.

- [27] MATLACK, K. H., WALL, J. J., KIM, J.-Y., QU, J., JACOBS, L. J., and VIEHRIG, H.-W., “Evaluation of radiation damage using nonlinear ultrasound,” *Journal of Applied Physics*, vol. 111, no. 5, p. 054911, 2012.
- [28] MÜLLER, M. F., “Analytical investigation of internally resonant second harmonic lamb waves in nonlinear elastic isotropic plates,” Master’s thesis, Georgia Institute of Technology, 2009.
- [29] NORRIS, A. N., “Symmetry conditions for third order elastic moduli and implications in nonlinear wave theory,” *Journal of Elasticity*, vol. 25, pp. 247–257, May 1991.
- [30] REUTOV, V. P., “Use of the averaged variational principle for describing multiwave interactions of elastic surface waves,” *Radiophysics and Quantum Electronics*, vol. 16, pp. 1307–1316, Nov 1973.
- [31] ROLLINS, F. R., “Interaction of ultrasonic waves in solid media,” *Applied Physics Letters*, vol. 2, no. 8, p. 147, 1963.
- [32] ROSE, J. L., *Ultrasonic Waves in Solid Media*. Cambridge University Press, 1999.
- [33] SHULL, D. J., “Harmonic generation in plane and cylindrical nonlinear Rayleigh waves,” *The Journal of the Acoustical Society of America*, vol. 94, no. 1, p. 418, 1993.
- [34] SHULL, D. J., “Diffraction effects in nonlinear Rayleigh wave beams,” *The Journal of the Acoustical Society of America*, vol. 97, no. 4, p. 2126, 1995.
- [35] STOBBE, D. M., “Acoustoelasticity in 7075-t651 aluminum and dependence of third order elastic constants on fatigue damage,” Master’s thesis, Georgia Institute of Technology, 2005.
- [36] VIKTOROV, I. A., *Rayleigh and Lamb Waves : Physical Theory and Applications*. Plenum Press, 1967.
- [37] WALKER, S. V., “Characterization of fatigue damage in A36 steel specimens using nonlinear Rayleigh surface waves,” Master’s thesis, Georgia Institute of Technology, 2011.
- [38] WALKER, S. V., KIM, J.-Y., QU, J., and JACOBS, L. J., “Fatigue damage evaluation in a36 steel using nonlinear Rayleigh surface waves,” *NDT & E International*, vol. 48, pp. 10–15, Jun 2012.
- [39] WOLFRAM RESEARCH, “Wolfram Research 3D Rayleigh wave model.” <http://www.wolfram.com/cdf/uses-examples/infographics-full-example.html>, accessed August 2013.

- [40] ZABOLOTSKAYA, E. A., “Nonlinear propagation of rayleigh waves,” *Optical and Acoustical Review*, vol. 1, pp. 133–140, 1990.
- [41] ZABOLOTSKAYA, E. A., “Nonlinear propagation of plane and circular Rayleigh waves in isotropic solids,” *The Journal of the Acoustical Society of America*, vol. 91, no. 5, pp. 2569–2575, 1992.
- [42] ZEITVOGEL, D., “Characterization of damage due to stress corrosion cracking in carbon steel using nonlinear surface acoustic waves,” Master’s thesis, Georgia Institute of Technology, 2012.